

INFLUENCE OF MICROPATTERNED POLYMERIC SUBSTRATES ON
CANCER CELL BEHAVIOR

A THESIS SUBMITTED TO
THE GRADUATE SCHOOL OF NATURAL AND APPLIED SCIENCES
OF
MIDDLE EAST TECHNICAL UNIVERSITY

BY
MENEKŞE ERMIŞ ŞEN

IN PARTIAL FULFILLMENT OF THE REQUIREMENTS
FOR
THE DEGREE OF DOCTOR OF PHILOSOPHY
IN
BIOMEDICAL ENGINEERING

JUNE 2016

Approval of the thesis:

**INFLUENCE OF MICROPATTERNED POLYMERIC SUBSTRATES ON
CANCER CELL BEHAVIOR**

submitted by **MENEKŞE ERMİŞ ŞEN** in partial fulfillment of the requirements for the degree of **Doctor of Philosophy in Biomedical Engineering Department, Middle East Technical University** by,

Prof. Dr. Gülbin Dural Ünver
Dean, Graduate School of **Natural and Applied Sciences**

Prof. Dr. Hakan Işık Tarman
Head of Department, **Biomedical Engineering, METU**

Prof. Dr. Vasıf Hasırcı
Supervisor, **Biomedical Engineering and Biological Sciences Departments, METU**

Assoc. Prof. Dr. Utkan Demirci
Co-supervisor, **Radiology Department, SoM, Stanford University, CA, USA**

Examining Committee Members:

Prof. Dr. Atilla Aydınlı
Physics Department, Bilkent University

Prof. Dr. Vasıf Hasırcı
Biological Sciences, Biomedical Engineering, METU

Doç. Dr. Sreeparna Banerjee
Biological Sciences, Biomedical Engineering, METU

Doç. Dr. Rengül Çetin Atalay
Bioinformatics Department, METU

Doç. Dr. Güvem Gümüş Akay
Brain Research Center (BAUM), Ankara University

Date: 07.06.16

I hereby declare that all information in this document has been obtained and presented in accordance with academic rules and ethical conduct. I also declare that, as required by these rules and conduct, I have fully cited and referenced all material and results that are not original to this work.

Name, Last Name: Menekşe Ermiş Şen

Signature:

ABSTRACT

INFLUENCE OF MICROPATTERNED POLYMERIC SUBSTRATES ON CANCER CELL BEHAVIOR

Ermiş Şen, Menekşe

Ph.D., Department of Biomedical Engineering

Supervisor: Prof. Dr. Vasıf Hasırcı

Co-Supervisor: Assoc. Prof. Utkan Demirci

June 2016, 160 pages

The aim of this study was to develop micropatterned surfaces on biodegradable polymers such as PLGA and PLLA and non-degradable polymer PMMA to study cellular responses including proliferation, cellular morphology, nucleus morphology and deformation, focal adhesions and related pathways, cell division and cycle, and epithelial to mesenchymal transition in cancer cells. An array of nine surfaces decorated with micron sized micropillars were produced using photolithography. Saos-2 osteosarcoma and hOB human osteoblast-like cells were cultured on the micropillar array made from PLGA, PLLA or their blends for focal adhesion and micropillar bending studies. Deformations of nuclei on the micropatterned surfaces were studied with Saos-2, hOB, L-929 mouse fibroblast, SH-SY5Y neuroblastoma, and MCF-7 breast carcinoma cells. Cell division and cycle studies were conducted with Saos-2 cells on PLGA and MDA-MB231 and MCF-7 cells on PMMA. All surfaces induced nucleus deformations but smaller interpillar distances were found to

be most effective. Of all the cells tested for nucleus deformations, cancer cells (Saos-2, MCF-7, SH-SY5Y) deformed most prominently. Both Saos-2 and hOB cells were found to apply similar forces to bend pillars and highest bending forces were applied on PLGA and PLLA substrates rather than their blends. Micropatterned PMMA substrates were found to effect cell cycle and induce an arrest at G0/G1 phase. RT-qPCR and RNA sequencing analysis demonstrated that Micropatterned PMMA surfaces induced EMT in epithelial breast cancer cells. Micropatterned substrates were proven to affect many cellular processes and intracellular signaling pathways. Cancer cells were found to be more prone to these changes.

Keywords: Micropatterns, pillar, poly(lactic acid-*co*-glycolic acid), cancer, nucleus, cytoskeleton, deformation, cell-surface interactions, gene expression

ÖZ

MİKRODESENİLİ POLİMERİK SÜBSTRATLARIN KANSER HÜCRESİ DAVRANIŞI ÜZERİNE ETKİSİ

Ermiş Şen, Menekşe

Doktora Tezi, Biyomedikal Mühendisliği Bölümü

Tez Yöneticisi: Prof. Dr. Vasıf Hasırcı

Ortak Tez Yöneticisi: Doç. Dr. Utkan Demirci

Haziran 2016, 160 sayfa

Bu çalışmanın amacı PLGA ve PLLA gibi biyobozunur ve PMMA gibi bozunmaz polimerler kullanarak mikrodeseanlı yüzeyler üretmektir. Bu yüzeyler kullanılarak hücrelerin çoğalma, hücre morfolojisi, çekirdek morfolojisi ve deformasyonu, fokal adhezyonlar ve ilişkili yolaklar, hücre bölünmesi döngüsü ve kanser hücrelerinde epitel-mezenşimal dönüşüm yanıtları incelenmiştir. Bu amaçla fotolitografi yöntemi kullanılarak mikrodeseanlarla donatılmış dokuz yüzey üretilmiştir. Saos-2 osteosarkom ve hOB insan osteoblast benzeri hücreleri PLGA, PLLA ve bu iki polimerin karışımından üretilen mikrodeseanlı yüzeyler üzerinde büyütülmüş ve fokal adhezyon ve mikro sütunları bükme özellikleri araştırılmıştır. Mikrodeseanlı yüzeyler üzerinde çekirdek deformasyonlarının incelenmesinde Saos-2, hOB, L-929 fare fibroblast, SH-SY5Y nöroblastom ve MCF-7 meme kanseri hücreleri ile gerçekleştirilmiştir. Hücre bölünmesi ve döngüsü çalışmalarında PLGA üzerinde Saos-2 hücreleri ve PMMA üzerinde MDA-MB231 ve MCF-7 hücreleri büyütülmüştür. Bütün mikrodeseanlı yüzeylerin çekirdeği deforme ettiği, mikro

sütunların aralığı en dar olan yüzeylerde deformasyonun en üst düzeyde olduğu saptanmıştır. Test edilen tüm hücre tipleri içerisinde en belirgin çekirdek deformasyonu kanser hücrelerinde (Saos-2, MCF-7, SH-SY5Y) gözlenmiştir. Saos-2 ve hOB mikro sütunları bükme için benzer düzeyde kuvvet uygulamaktadırlar. Mikrosütunlar arasında en fazla kuvvet PLGA ve PLLA yüzeylerde saptanmıştır. Mikrodesenli PMMA yüzeylerin hücre döngüsü üzerine etkisi olduğu ve G0/G1 fazında duraklamaya yol açtığı bulunmuştur. Epitel kökenli meme kanseri hücrelerinde RT-qPCR ve RNA sekanslama analizleri ile mikrodesenli PMMA yüzeylerin epitel-mezenşimal dönüşümünü uyardıkları görülmüştür. Sonuç olarak mikrodesenli yüzeyler bir çok hücreyel süreç ve hücre içi sinyal yolağını etkilemektedir. Kanser hücrelerinin bu değişikliklere daha duyarlı olduğu saptanmıştır.

Anahtar kelimeler: Mikrodesenler, sütun, poli(laktik asit-*ko*-glikolik asit), kanser, hücre çekirdeği, hücre iskeleti, şekil bozulmaları, hücre-yüzey etkileşimleri, gen ifadesi

Dedicated to all my beloved ones...

ACKNOWLEDGEMENTS

"...we have spent five decades studying the cerebral cortex in excruciating detail, but we still don't have the foggiest idea of how it works or what it does. We are all like asexual Martians visiting earth who spent fifty years examining the detailed cellular mechanisms and biochemistry of the testicles without knowing anything at all about sex.."

Horace Barlow, Cambridge Physiologist

Scientific research is excruciatingly detailed, tabulated and systematical; it is at the same time convoluted, perplexing and labyrinthine. Unless one is strongly guided, it is very easy to get lost. I would like to thank my thesis supervisor Prof. Dr. Vasif Hasırcı; who guided me for all these years and kept me in perspective, my research relevant and every excruciating detail in context; without whom I would be lost. His patience towards me (a young, excited graduate yet to be seasoned in academia) was everlasting. His will not only drives biomaterials field and BIOMATEN forward, it also sets an excellent and unique example to me as his Ph.D. student.

I would like to thank to my co-supervisor Prof. Dr. Utkan Demirci, whom not only opened the doors of his lab but also allowed me to have a unique experience in Stanford, while providing unlimited opportunities for research.

I would also like to thank to Prof. Dr. Nesrin Hasırcı, for supporting me throughout my Ph.D. and unrestrictedly sharing her insight. She is also a significant role model for all the women in academia.

I would like to thank to...

...my husband, my best friend, my partner in life, he who never left my side throughout this journey and many others and for better, for worse, in sickness and in health, without you I couldn't have come this far.

...my father for setting the path and my mother for keeping me on the path, and my brother for showing me that there are many other paths and all my family, for being my family.

...all my friends. Some friendships are forever. Deniz Sezlev Bilecen and Canan Kurşungöz; you endured all my scientific gibberish, never ending complaints and were there for me all the way. Aysu Küçükurhan, my sister and longest long distance friendship, gratitude is the best word for always being there for me. Gözde Eke, I appreciate all the weekdays, weekends, impulsive shopping trips, late night visits; your friendship (even though I am not very good at showing it). Saime Ünlüsoy, you are my teacher, friend and companion, even if our paths do not cross as often as we desire, I know that you're there... Elvin İřcan İnsel thank you for a friendship not for everyone but for all the times, Ayře Gökçe Bor for being you no matter what and Ayře Karancı for the child still in us. Aylin Kömez for your never-ending energy. Onur Hastürk thank you for sharing, helping and being my companion on this micropatterned journey. Ezgi Antmen for being the voice of logic. Arda Büyüksungur for teaching me the basics of a research lab at the very beginning of my carrier. Pu Chen and Gözde Durmuř for all their help and kind friendship during my visit to Stanford

...I would specially thank to Emre Insel, the ultimate civil engineer, who introduced me to the world of beams and bending and helped me with all the engineering steps that I direly needed.

...Derya Akkaynak for all the endless nights we spent on Skype and g-talk, strength and stamina to understand all the biological processes under the hood of the required analysis, and especially to the friendship that overcame distances and 3 continents, 4 countries and never meeting face to face to this day.

Semih Çalamak for being the best lab-partner throughout my studies abroad and a dear friend thereafter...

...my friends that I lost on the road. Durmuř Ekin Tařatan not a single day passes by without wishing you were here...

I would like to thank to all my labmates and graduates Senem Büyüksungur, Gökhan Bahçeciođlu, Cemile Bektař, Tuđba Dursun, Ayře Selcen Alagöz, Aysel Kızıltay, Tuđba Endođan Tanır, Pınar Yılgör Huri. Our technician Zeynel Akın for his patience and help throughout these years.

This study was supported by DPT2011K120350 Ministry of Development grant, and TUBITAK 2211C PhD scholarship.

TABLE OF CONTENTS

ABSTRACT.....	v
ÖZ.....	vii
ACKNOWLEDGEMENTS.....	x
TABLE OF CONTENTS.....	xii
LIST OF TABLES.....	xvi
LIST OF FIGURES.....	xvii
LIST OF ABBREVIATIONS.....	xxiii
CHAPTER 1	
INTRODUCTION.....	1
1.1. Biology of cell, nucleus, division and mechanotransduction.....	1
1.1.1. Cell, cytoskeleton and nucleus.....	1
1.1.1.1. The Cell and cytoskeleton.....	1
1.1.1.2. The Nucleus.....	5
1.1.2. Cell adhesion and mechanotransduction.....	7
1.2. Biomaterials and micro and nano patterns: Production and use in biomaterials and cell-substrate introduction.....	15
1.2.1. Biomaterials for studying surface patterns.....	15
1.2.2. Surface patterning technologies at micro and nano level.....	17
1.2.3. Need for patterned substrates to study cell and nucleus.....	17
1.3. Cancer cell mechanics and micropatterned substrates.....	18
CHAPTER 2	
MATERIALS AND METHODS.....	21
2.1. Materials.....	21
2.2. Methods.....	22
2.2.1. Preparation of micropatterned silicon wafers.....	22
2.2.2. Preparation of micropatterned films.....	24
2.2.3. Characterization of films.....	25
2.2.3.1. Surface profilometry.....	25

2.2.3.2. Contact angle measurements	25
2.2.3.3. Scanning Electron Microscopy (SEM)	26
2.2.3.4. Tensile testing	26
2.2.4. <i>In vitro</i> studies	27
2.2.4.1. Cell culture.....	27
2.2.4.1.1. Isolation and culture of human osteoblast like (hOB) cells.....	27
2.2.4.1.2. Saos-2, MCF-7, MDA-MB 231, SH-SY5Y, L929 cell culture	28
2.2.4.1.3. Cell seeding onto the micropatterned films	29
2.2.4.2. Determination of cell viability, adhesion and proliferation by Alamar Blue assay.....	29
2.2.4.3. Cell cycle analysis with flow cytometry	30
2.2.5. Microscopy	30
2.2.5.1. Specimen preparation for fluorescence microscopy	30
2.2.5.2. Nuclear stains to study nuclear deformation.....	31
2.2.5.3. Immunocytochemistry	31
2.2.5.4. Confocal Laser Scanning Microscope (CLSM) and widefield fluorescence microscope imaging.....	31
2.2.6. Analysis of nucleus deformation	31
2.2.6.1. Image-based quantification of cell deformation	31
2.2.6.2. Image pre-processing.....	32
2.2.6.3. Feature extraction	32
2.2.6.4. Surface selection	33
2.2.6.5. Nuclear deformation on the P4G4 surface.....	34
2.2.7 Bending of Pillars	36
2.2.8. Molecular biology studies.....	37
2.2.8.1. qPCR studies.....	37
2.2.8.1.1. Isolation of total RNA	37
2.2.8.1.2. Primer Design	37
2.2.7.1.3. cDNA synthesis	38
2.2.7.1.4. qPCR and analysis	38
2.2.7.1.5. The Human Focal Adhesions RT ² Profiler PCR Array	39
2.2.8.2. RNA Sequencing	40

CHAPTER 3

RESULTS AND DISCUSSION	41
3.1. Characterization	41
3.1.1. Thermal characterization using DSC	41
3.1.2. Tensile testing	43
3.1.3. Surface design and characterization.....	46
3.1.4. Surface Profilometry	48
3.1.5. Water contact angles and wettability	50
3.2. Isolation of Human Osteoblast Like Cells (hOBs)	54
3.3. Nucleus Deformation on Micropatterned Substrates	56
3.4. Cell Viability on Micropatterned Substrates.....	58
3.5. Quantification of nuclear deformation on micropatterned substrates.....	61
3.6. Effect of Micropatterns on Cell Adhesion	66
3.6.1. Cell behavior on micropatterned substrates	66
3.6.2. Patterned surfaces and focal adhesions.....	66
3.6.3. Cell Type and Surface Interaction	71
3.6.4. Calculations of Pillar Bending Force.....	71
3.6.4.1 Saos-2 cells pillar bending forces on PLGA micropatterned surfaces	77
3.6.4.2 Bending of PLGA P8G8 pillars by Saos-2 vs hOB cells.....	82
3.6.4.3 Saos-2 cells pillar bending forces on P8G4 PLGA vs PLLA vs PLGA:PLLA 80:20	85
3.6.5. PCR Array of Focal Adhesion Related Genes of hOB and Saos2 on Micropatterned Substrates	88
3.7. Cell division and cell cycle progression on micropatterned substrates	94
3.7.1. Saos-2 Cells	94
3.7.2. MDA-MB-231 cells.....	98
3.7.3. Regulation of Cell Cycle in MDA-MB231 and MCF-7 Cells on Micropatterned Substrates	102
3.8. Effect of Micropatterned Substrates on Epithelial-to-Mesenchymal Transition (EMT) of Breast Carcinoma Cells	105
3.8.1. Expression of EMT Markers.....	105
3.8.2. Immunohistochemistry of EMT Markers	109

3.9. RNA Sequencing of MDA-MB231 Cells on Micropatterned Substrates.....	111
CHAPTER 4	
CONCLUSION.....	119
REFERENCES	123
APPENDIX A.....	139
APPENDIX B.....	141
APPENDIX C.....	145
APPENDIX D.....	153
APPENDIX E.....	157
CURRICULUM VITAE.....	159

LIST OF TABLES

TABLES

Table 1: Intermediate filaments types and tissue of origin (Gartner et al., 2012)	4
Table 2: Phenotypes associated with null mutations in focal contact proteins (Mitra et al., 2005).	10
Table 3: Primer sequences	38
Table 4: Selection of micropatterned substrate and cell type for RT2 focal adhesion PCR array.....	39
Table 5: Abbreviations of the surfaces according to the pillar dimensions and spacings in the array.....	47
Table 6: Gene ontology (GO) enrichment in 48 h SM TCPS vs 48 h SFM+12 h SM TCPS groups.	115
Table 7: Gene ontology (GO) enrichment in 48 h SM TCPS vs 48 h Micropatterned groups.....	116
Table 8: Gene ontology (GO) enrichment in 48 h SM TCPS vs 48 h SM Unpatterned groups.....	116
Table 9: Gene ontology (GO) enrichment in 48 h SM Unpatterned vs 48 h SM Micropatterned groups.	117

LIST OF FIGURES

FIGURES

Figure 1: Cell and organelles (Gartner et al., 2012).	3
Figure 2: Cytoskeletal proteins, their subunits and representative images (Pollard et al., 2003).	4
Figure 3: Nuclear membrane, lamina and their cytoskeletal connections.	7
Figure 4: Focal adhesion proteins and their assembly (adapted from Wozniak et al., 2004).	9
Figure 5: Focal adhesion kinase promotes cytoskeletal fluidity (Mitra et al., 2005).	11
Figure 6: Multiple roles of NM II in cell migration. (Vicente-Manzanares et al., 2009).	11
Figure 7: Tensegrity network of nucleus and its actin connection (Hutchinson et al., 2002).	12
Figure 8: Signal transmission rates of mechanical and chemical signals (Wang et al., 2009).	13
Figure 9: Force transduction from outside in (Wang et al., 2009)	14
Figure 10: Structures of PLGA, PLA and PLGA (Gunatillake et al., 2003).....	16
Figure 11: Production of SU-8 micropillar array chip.....	23
Figure 12: Representative sketch of 9 micropatterned array chips.....	24

Figure 13: Preparation of PDMS molds and poly(lactic acid-co-glycolic acid) (PLGA) (85:15) micropatterned films from SU-8 micropatterned array chips.	25
Figure 14: Primary isolation of hOB cells.	28
Figure 15: DSC thermograms of PLLA and PLGA polymers. Scan was conducted between 0-240°C (T_m endothermic peak was shown with dotted lines).	42
Figure 16: DSC thermograms of PLLA and PLGA polymers. Scan was conducted between 20-80°C (T_g endothermic peaks were shown with dotted lines).	43
Figure 17: Representative stress-strain curves for PLGA and PLLA polymers.	44
Figure 18: Mechanical property change with the composition of the polymer.	45
Figure 19: Surface profilometry results for various patterned surfaces.	49
Figure 20: Water contact angles of unpatterned PLLA, PLGA and PLGA:PLLA blend films, measured by sessile drop method.	51
Figure 21: Water contact angles of micropatterned PLGA films measured by sessile drop method.	52
Figure 22: Human osteoblast like cells (HOB) were isolated from surgical bone explants by incubating for a month in culture medium.	54
Figure 23: Fluorescent microscopy images of HOB cells.	55
Figure 24: Design of the micropillar array chip and response of the Saos-2 cells to test the effect of pillar dimensions and spacing on deformations of the nucleus.	57
Figure 25: Day 1 Alamar Blue® results of 9 micropillar array surfaces and control, seeded with 5000 Saos-2 cells	58
Figure 26: Alamar Blue® results of 9 micropillar array surfaces and control seeded with 5000 Saos-2 cells showing proliferation on different substrate topographies. ..	60

Figure 27: Deformation frequency and Principal Component 1 (PC1) of Saos2 cells on 10 surfaces tested. descriptors.	62
Figure 28: Circle variance (CV) and rectangularity (R) graphs of hypothetical nucleus deformations, Saos-2 and hOB cells.....	63
Figure 29: Quantification of deformation of two non-cancerous (hOB, L-929) and three cancer cell (Saos-2, MCF-7, SH-SY5Y) types on P4G4 surface.	65
Figure 30: Saos-2 osteosarcoma cells cultured for 48 h on PLLA and PLGA surfaces.	68
Figure 31: Overlaid images of focal adhesions stained with anti-vinculin antibody and actin cytoskeleton of Saos-2 cells cultured on PLGA.....	69
Figure 32: CLSM micrographs of Saos-2 osteosarcoma cells cultured on PLGA surfaces for 48 h, fixed and imaged.	70
Figure 33: SEM micrographs of hOB and Saos-2 cultured on P8G16, and P8G8 PLGA micropatterned surfaces.....	72
Figure 34: Calculation of pillar bending forces was modeled according to beam bending equations.	73
Figure 35: Bending of pillars were calculated from the deflection in x and y axis (Δ_x , Δ_y) of the SEM images of the pillars.	74
Figure 36: Bending force on PLGA Pillar 1 (Panel 1).	74
Figure 37: Schematic representation of a bending pillar.	75
Figure 38: Bending force of the Pillar 1 of PLGA Panel 1 calculated according to Case a (to the free end of the beam), and Case d (to whole length of the shaft of the beam, increasing towards the free end) with and without taking shear deflection into consideration.	76

Figure 39: SEM micrographs of Saos-2 cells cultured on P8G4 PLGA substrate for 48 h. Deflection of pillars in x and y axis were calculated from 5 panels. 78

Figure 40: SEM micrographs of Saos-2 cells cultured on P8G8 PLGA substrate for 48 h. Deflection of pillars in x and y axis were calculated from 5 panels. 79

Figure 41: SEM micrographs of Saos-2 cells cultured on P8G16 PLGA substrate for 48 h. Deflection of pillars in x and y axis were calculated from 8 panels. 80

Figure 42: Pillar displacements and forces calculated using SEM micrographs of Saos-2 cells cultured on micropatterned P8G4, P8G8, P8G16 substrates. 81

Figure 43: SEM micrographs of hOB cells cultured on P8G8 PLGA substrate for 48 h. Deflection of pillars in x and y axis were calculated from 5 panels. 83

Figure 44: Pillar displacements and forces calculated from SEM micrographs of Saos-2 and hOB cells cultured on P8G8 micropatterned substrates. 84

Figure 45: Average number of pillars each cell interacted and average force per cell calculated from these measurements. 84

Figure 46: SEM micrographs of Saos-2 cells cultured on P8G4 PLLA substrate for 48 h. 86

Figure 47: SEM micrographs of Saos-2 cells cultured on P8G4 PLGA:PLLA 80:20 substrate for 48 h. 87

Figure 48: Pillar displacements and forces calculated from SEM micrographs of Saos-2 cells cultured on P8G4 PLGA:PLLA 100:0, 0:100 and 80:20 micropatterned substrates. 88

Figure 49: Fold changes of the focal adhesion genes for Saos-2 and hOB cells cultured on PLLA and PLGA substrates with P8G4 patterns. 90

Figure 50: Fold changes of the focal adhesion genes for Saos-2 cells cultured on PLLA substrates with P8G4 and P8G8 patterns. 91

Figure 51: Fold changes of the 3 groups genes (integrins, FAK signaling pathway, cytoskeletal regulator genes) of focal adhesion PCR array for Saos-2 and hOB cells cultured on P8G4 PLLA and PLGA.	93
Figure 52: Schematic representation and microscopy of cell division phases.	95
Figure 53: Top view and cross sections (at the edges as xz and yz axes) of Saos-2 cells cultured on P8G4 substrate.	97
Figure 54: Cell cycle analysis of MDA-MB-231 cells using flow cytometry.	99
Figure 55: Immunocytochemistry of MDA-MB-231 cells with Ki67, tubulin- α and DAPI.	101
Figure 56: Ki-67 mRNA levels of MCF-7 and MDA-MB231 cells cultured on micropatterned substrates for up to 72 h.	103
Figure 57: Cyclin A mRNA levels of MCF-7 and MDA-MB231 cells cultured on micropatterned substrates for up to 72 h. mRNA.	103
Figure 58: Cyclin B mRNA levels of MCF-7 and MDA-MB231 cells cultured on micropatterned substrates for up to 72 h.	104
Figure 59: p21 mRNA levels of MCF-7 and MDA-MB231 cells cultured on micropatterned substrates for up to 72 h.	104
Figure 60: Basal vimentin and E-cadherin expression of MDA-MB231 cells compared to MCF-7 cells.	106
Figure 61: Vimentin mRNA levels of MCF-7 and MDA-MB231 cells cultured on micropatterned substrates for up to 72 h.	107
Figure 62: E-cadherin mRNA levels of MCF-7 and MDA-MB231 cells cultured on micropatterned substrates for up to 72 h.	108

Figure 63: CLSM images of MDA-MB231 cells cultured on control and P4G4 surfaces up to 7 days. **110**

Figure 64: Vimentin/E-cadherin ratios of the MDA-MB231 cells cultured on control and P4G4 surfaces up to 7 days. **111**

Figure 65: RNA sequencing results for EMT related genes of TCPS (48h SM, 48h SFM+12h SM) and micropatterned and unpatterned PMMA (48h SM) samples... **113**

LIST OF ABBREVIATIONS

μm	micrometer
2D	Two Dimensional
3D	Three Dimensional
BSA	Bovine Serum Albumin
CA	Contact Angle
CLSM	Confocal Laser Scanning Microscopy
CO ₂	Carbon Dioxide
d	days
Da	Dalton
DAPI	4', 6-diamidino-2-phenylindole
DMEM	Dulbecco's Modified Eagle Medium
DMSO	Dimethyl Sulfoxide
E	Young's Modulus
ECM	Extracellular Matrix
EDTA	Ethylenediaminetetraacetic Acid
EMT	Epithelial-to-mesenchymal Transition
FAK	Focal Adhesion Kinase
FBS	Fetal Bovine Serum
g	gram
h	hour
hOB	Human Osteoblast-like Cells
GPa	Gigapascal
HUVEC	Human Umbilical Vein Endothelial Cells
kDa	Kilodalton
kPa	Kilopascal
LINC	Linker of Nucleus and Cytoskeleton

M	Molarity
mg	milligram
min	minute
mL	milliliter
mm	millimeter
mM	millimolar
MPa	Megapascal
MW	Molecular Weight
NaOH	Sodium Hydroxide
nm	nanometer
OsO ₄	Osmium Tetroxide
PAAm	Polyacrylamide
PBS	Phosphate Buffer Saline
PC	Principal Component
PCL	Poly(caprolactone)
PDMS	Poly(dimethylsiloxane)
PE	Polyethylene
Pen/Strep	Penicillin/Streptomycin
PET	Poly(ethylene terephthalate)
PGA	Poly(glycolic acid)
PHAs	Polyhydroxyalkanoates
PHBV	Poly(3-hydroxybutyrate-co-3-hydroxyvalerate)
PHB	Poly(3-hydroxy butyrate)
PIPES	Piperazine-N, N'-Bis(Ethanesulfonic Acid)
PLA	Poly(lactic acid)
PLGA	Poly(lactic acid-co-glycolic acid)
PLLA	Poly(l-lactic acid)
PMMA	Poly(methyl methacrylate)
PS	Polystyrene
PVC	Poly(vinyl chloride)
SEM	Scanning Electron Microscopy
TCPs	Tissue Culture Polystyrene

TGF- β 1	Transforming Growth Factor Beta-1
UC	Unpatterned Control
UTS	Ultimate Tensile Strength
UV	Ultraviolet
w	weight
w/v	weight/volume ratio

CHAPTER 1

INTRODUCTION

1.1. Biology of cell, nucleus, division and mechanotransduction

1.1.1. Cell, cytoskeleton and nucleus

1.1.1.1. The Cell and cytoskeleton

Cell is the smallest functional unit of living organisms. Cells consist of cytoplasm and nucleus. Cytoplasm is separated from the surrounding environment by plasma membrane. Plasma membrane is made up of phospholipid bilayer and membrane proteins are embedded into this bilayer. Plasma membrane has many functions including cell-cell recognition, transport, receptor site for signaling molecules, and initiator and controller of secondary messenger systems. There are organelles in eukaryotic cell cytoplasm. These organelles are mitochondria, ribosomes, endoplasmic reticulum, golgi apparatus, endosomes, lysosomes, and peroxisomes (Gartner et al., 2012) (Figure 1). Most of the organelles in a cell has a membrane. About half the total area of membrane in a eukaryotic cell encloses the labyrinthine spaces of the endoplasmic reticulum (ER). The rough ER has many ribosomes bound to its cytosolic surface.

There is also a supporting network for the cell. Cell cytoskeleton is in the cytoplasm and is a filamentous network functioning as a structural framework and takes roles in transport, migration, division and polarization of the cell.

There are three types of cytoskeletal elements in a cell: microtubules, intermediate filaments and actin filaments (Figure 2) (Gartner et al., 2012). All cytoskeletal elements are made up of monomer units and polymerization of these subunits are under strict control (Pollard et al., 2003). Actin filaments and microtubules polymerization and depolymerization generating directed forces that result in changes in cell shape (Fletcher et al., 2010). Microtubules are made up of α and β tubulin units arranged in 13 protofilaments. Microtubules originate from the microtubule-organizing center (MTOC) and take role in chromosome alignment and separation of sister chromatids during cell division. There are different types of intermediate filaments in cells (Table 1). Actin filaments have the smallest fiber diameter among all and they come together to form bundles. These bundles support filopodial protrusions, which are involved in chemotaxis and cell–cell interaction and communication (Fletcher et al., 2010). Intermediate filaments are found in a tissue specific manner (Table 1) and can be used as markers for the tumors originating from the tissueS they are abundantly found.

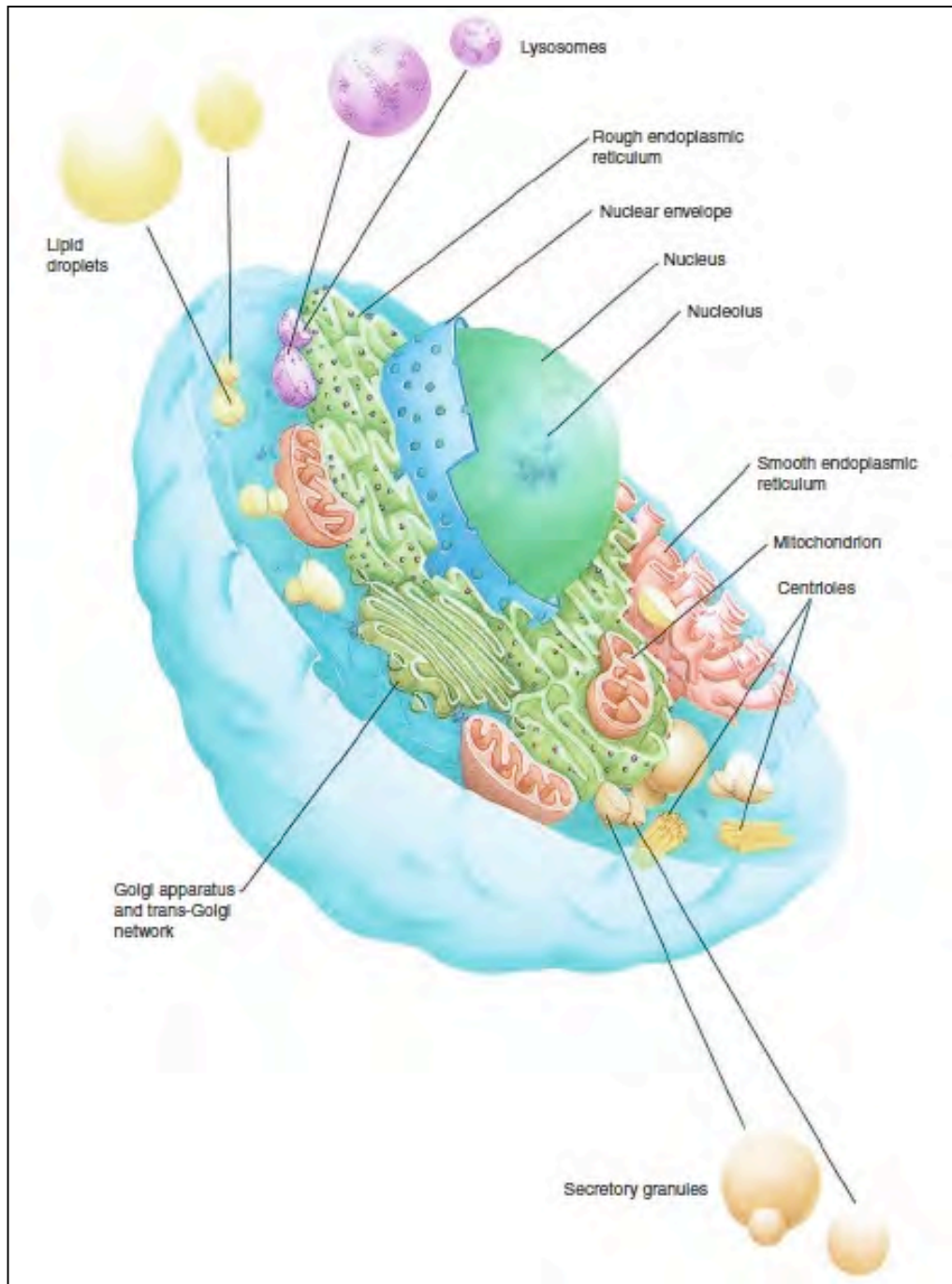


Figure 1: Cell and organelles (Gartner et al., 2012).




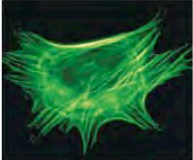
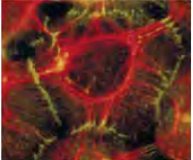
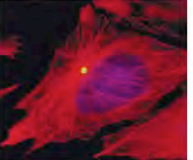
Polymer	Actin filament	Microtubule	Intermediate filament
Protein subunit	Actin monomer	Tubulin heterodimer	Various proteins with an α -helical coil
Electron micrographs of polymers			
Fluorescence micrographs of cells with polymers			

Figure 2: Cytoskeletal proteins, their subunits and representative images (Pollard et al., 2003).

Table 1: Intermediate filaments types and tissue of origin (Gartner et al., 2012)

Type	Location	Function
Keratin	Epithelial cells Cells of hair and nails	Support; tension bearing; withstands stretching; associated with desmosomes, hemidesmosomes, and tonofilaments; immunological marker for epithelial tumors
Vimentin	Mesenchymal cells, chondroblasts, fibroblasts, endothelial cells	Structural support, forms cage-like structure around nucleus; immunological marker for mesenchymal tumors
Desmin and vimentin	Muscle: skeletal, smooth, cardiac	Links myofibrils to myofilaments; desmin is an immunological marker for tumors arising in muscle
GFAP* and vimentin	Astrocytes, oligodendrocytes, Schwann cells, and neurons	Support; GFAP is an immunological marker for glial tumors.
Neurofilaments	Neurons	Support of axons and dendrites, immunological marker for neurological tumors.
Lamin A, B, and C	Lines nuclear envelope of all cells	Organizes and assembles nuclear envelope, maintains organization of nuclear chromatin
<i>*GFAP, glial fibrillary acidic protein</i>		

1.1.1.2. The Nucleus

The nucleus is connected to the cytoskeleton through some structural proteins embedded in the nuclear membrane. To understand the deformations in nuclear shape, the anatomy of the nucleus has to be considered. The nucleus is surrounded by a nuclear envelope (NE) consisting of two nuclear membranes, an underlying nuclear lamina and nuclear pore complexes (Figure 3). Outer nuclear membrane (ONM) is continuous with the endoplasmic reticulum. Inner nuclear membrane (INM) contains proteins specific to the nucleus. It acts as a barrier between the nucleus and cytoplasm. Nuclear lamina consists of lamin proteins which are type-V intermediate filament proteins (Gruenbaum et al., 2005). Lamins are categorized as A and B-type. B-type lamins are involved in cell viability and are expressed in cells during development. Studies show that all mammalian cells have one or both type B lamins, but lamins A/C are expressed specifically in differentiated cells and their expression is generally increased during terminal and growth arrest (Broers et al., 1997). All A-type lamins are transcribed from a single LMNA gene but with alternative mRNA splicing (Adapted from Gruenbaum et.al., 2005).

Transcriptionally silent heterochromatin in the nucleus is localized near the nuclear periphery. Lamins play a role in the attachment of chromatin to NE as was shown in Hutchinson-Gilford progeria where mutation of LMNA causes loss of heterochromatin from the nucleus (Goldman et al., 2004). Lamins bind to many known INM proteins, including emerin, MAN1, LBR, lamina-associated polypeptides-1 and -2 β and nesprin-1 α in vitro. Lamins also bind to histone H2A or H2B dimers, RNA-polymerase-II-dependent transcription complexes and DNA replication complexes (Prokocimer et al., 2009). It is suggested that reduced or absent lamin A/C expression is a common feature of a variety of cancers, including small cell lung cancer (SCLC), skin basal cell and squamous cell carcinoma, testicular germ cell tumor, prostatic carcinoma, leukemia, and Lymphomas. The reduction in lamin A/C expression is correlated with cancer subtypes, aggressiveness, proliferative capacity and differentiation state (Wu et al, 2009).

A well-established mechanism for gene silencing in human tumors is transcriptional inactivation by CpG island promoter hypermethylation is a well-established mechanism for gene silencing in human tumors. In Agrelo et.al study the epigenetic silencing effect of lamin A/C through CpG island promoter hypermethylation which resulted in the loss of lamin A/C gene expression was shown in leukemia and lymphomas and related to poor outcome (Agrelo et al., 2005). This suggests that lamin proteins are closely related to carcinogenesis through many different mechanisms. The linker of Nucleoskeleton and Cytoskeleton (LINC) complex connects nuclear lamina and nuclear membrane to the cytoskeleton. LINC complex is composed of a molecular bridge of SUN and KASH proteins that spans both nuclear membranes while SUN proteins interact with lamins in INM; they interact with KASH proteins in the perinuclear space (Starr et al., 2010).

There are several KASH proteins. KASH proteins Nesprin-1/Nesprin-2 connect nucleus to the cytoskeleton (Tapley et al., 2007). In the case of LINC complex components including nesprins and SUN proteins depletion, nuclear shape defects and an associated softening of the nucleus and the cytoplasm was observed (Lee et al., 2007). The nuclear lamina and LINC complex molecules have crucial roles in collective 2D migration and maybe cancer metastasis. When mechanical properties of normal and cancer cells were compared in biophysical settings it was consistently shown that cancer cells were found to be softer and that this cellular compliance was related to increased metastatic potential (Wirtz et al., 2011).

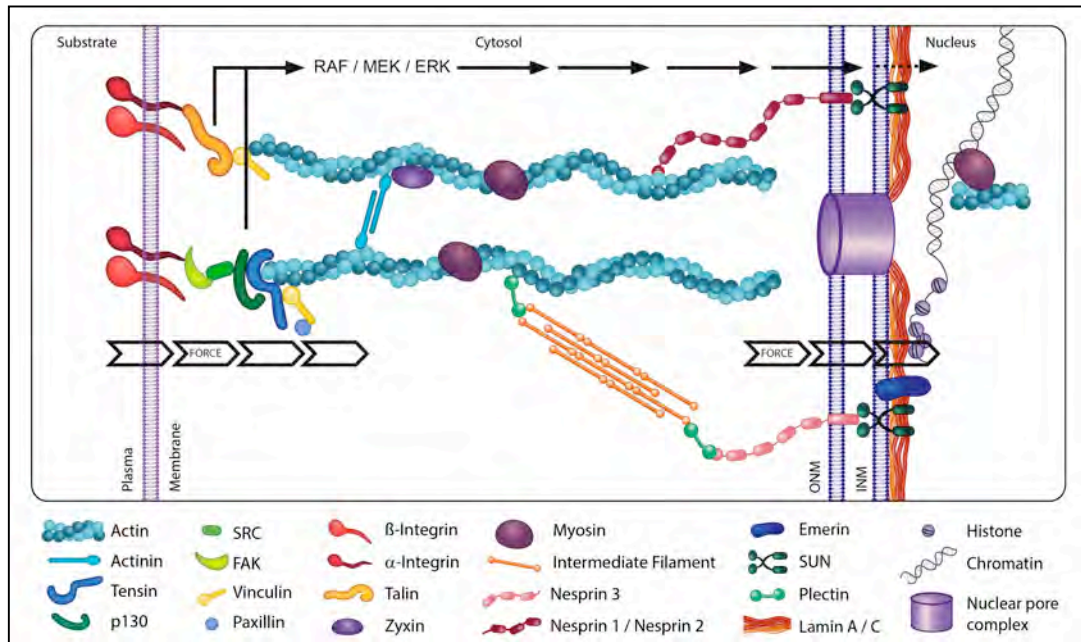


Figure 3: Nuclear membrane, lamina and their cytoskeletal connections.

1.1.2. Cell adhesion and mechanotransduction

Many different cell types that make up tissues and organs of an organism are adherent. Therefore, cell adhesion is a very important issue for these cell types. It is the binding process of a cell to the extracellular matrix, a surface or another cell using some specific surface proteins. This binding process results in two particular mechanisms which lead to intracellular signal generation: (i) creates a force on the cytoskeletal elements which is transmitted through the cytosol to the nuclear lamina, and (ii) initiates intracellular molecular signals and messengers. Cell adhesion process is dependent on integrin binding (Schwartz et al., 1995). Integrins are multimeric transmembrane proteins and involved in many processes including cell adhesion and migration (Figures 3, and 4). Integrins convey information both ways in and out. Inside out, cell adhesion strength can be controlled by changing the affinity and flexibility of integrins (Carman et al., 2003). Outside in signaling on the other hand depend on the cytoplasmic linking of integrins. Several proteins including paxillin, talin, α -actinin and filamin link integrins to actin cytoskeleton (Wozniak et

al., 2004). Structures where aggregates of integrins connect cell exterior to the cytosol are called focal adhesions (FA) (Figure 3, 4). FA create physical signals through binding to actin and chemical signals through phosphorylation of several proteins. At a focal adhesion site two major kinases play a role: focal adhesion kinase (FAK) and src. FAK autophosphorylates at Y397 residue after integrin binding to substrate and src docking to FAK through SH2 domain follows (Schlaepfer et al., 1999). This event activates src which leads to the activation of Raf-MEK-ERK signaling cascade (Roskoski et al., 2012). This process of transmitting of mechanical stimuli at the cell membrane into intracellular signals is called mechanotransduction. Through mechanotransduction cells can “feel” the force. Problems in mechanotransduction are linked with many diseases. For example, in Duchenne Muscular Dystrophy (DMD), force transmission between the extracellular matrix (ECM) and the cytoskeleton is disrupted due to the mutations in dystrophin gene resulting in progressive degeneration of muscle tissue (Heydemann et al., 2007). Mechanotransduction also plays an important role in cancer. In the study of Paszek et al. it was shown that Rho and ERK play a role in physical signals coming from ECM through integrin binding. A chronic increase in cytoskeletal tension due to elevated ERK activity through assembly of FA could enhance and change tissue organization and result in malignant transformation of a tissue or simply, cancer (Paszek et al., 2005).

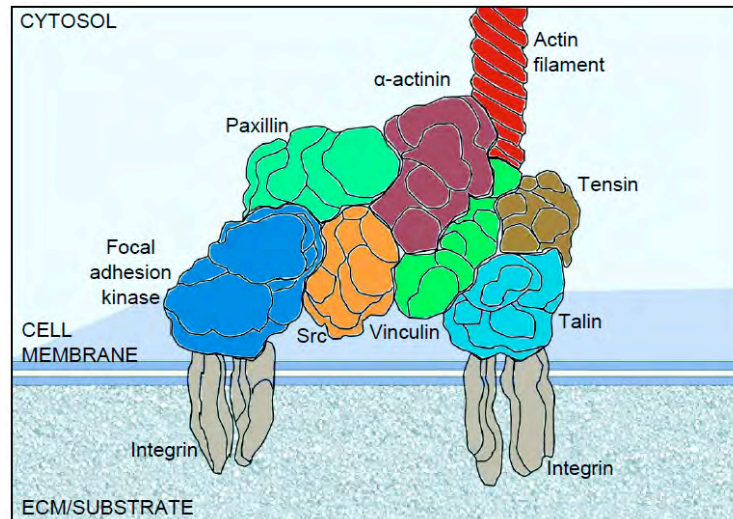


Figure 4: Focal adhesion proteins and their assembly (adapted from Wozniak et al., 2004).

Zaidel-Bar et al. constructed in silicon adhesome to study interconnectedness of focal adhesion associated proteins and they subdivided 156 component molecules into functional groups of adaptor proteins, cytoskeletal proteins, actin binding proteins, serine/threonine kinases, transmembrane receptors, adhesions proteins and other components (Zaidel-Bar et al., 2007). They concluded that compared with other mammalian intracellular interaction networks adhesome has higher number of links per node ratio.

It is expected from such a network proteins with more than 20 interactions (integrin, paxillin, Grb2, FAK, Src), forming prominent hubs are more prominent for the functions of the adhesome. Loss of these proteins were shown to be lethal in embryonic mouse (Table 2) (Zaidel-Bar et al., 2007) except one- Src. Src knockout mice were shown to be viable embryos with osteopetrosis (Soriano et al., 1991). However role of Src on cell morphology, cell adhesion and motility clearly indicated a role for Src in the regulation of cytoskeletal-linked events (Parsons et al., 2004) non-lethal loss of Src may be explained by compensation provided by other Src family members such as Lyn and Fyn.

Table 2: Phenotypes associated with null mutations in focal contact proteins (Mitra et al., 2005).

Cell phenotypes	Embryonic (lethality) day	Focal contact formation	Focal contact turnover	Integrin-stimulated migration	FAK tyrosine phosphorylation
FAK ^{-/-} (p53 ^{-/-})	8.5	Increased immature	Inhibited	Inhibited	NA
SYF ^{-/-}	9.5	No change	Inhibited	Reduced	pTyr397 reduced
p130Cas ^{-/-}	11.5-12.5	No change	Inhibited	Reduced	No difference
Paxillin ^{-/-}	9.5	Increased size	Decreased	Inhibited	pTyr397 reduced
Vinculin ^{-/-}	10.0	Decreased size	ND	Stimulated	Increased activity
PTPα ^{-/-}	None	Delayed	ND	Reduced	pTyr397 reduced
SHP2 ^{-/-}	8.5-10.5	Increased immature	Elevated	Inhibited	Increased activity in suspension
Calpain-4 ^{-/-}	10.0	Larger	Reduced	Decreased	No change

FAK regulates stress fibers and cortical actin stabilization and destabilization. In undisturbed state actin cytoskeleton is in a semi-solid state. This is due to α -actinin crosslinking of stress fibers which are connected to and exert tension at focal contacts (Figure 3, 5). FAK phosphorylation on Tyr-12 results in a more soluble α -actinin and releases actin stress fibers (Mitra et al., 2005).

Non-muscle myosin II (NMII) is integral in regulation of cell adhesion and polarity in cell migration. Since cell adhesion and polarity is very important for remodeling of the actin cytoskeleton it is also has utmost importance in interaction of the cell with its environment (Vicente-Manzanares et al., 2009). It reacts via cellular signaling pathways to mechanical stimuli and stand as a convergence point for external and cell-generated forces (Galbraith et al., 2002). When NMII is inhibited, cells stop responding to external forces (Chen 2008). Subcellular structures like nucleus, microtubule organizing center (MTOC) and Golgi apparatus have certain localizations in the cell and during polarization and migration their position has importance together with actin organization. It was observed that MtoC and golgi apparatus position themselves in front of the nucleus towards the direction of the protrusion (Etienne-Manneville et al., 2001). When NMII activity was inhibited by blebbistatin nuclear position regulatory functions of NMII became clear (Gomes et al., 2005).

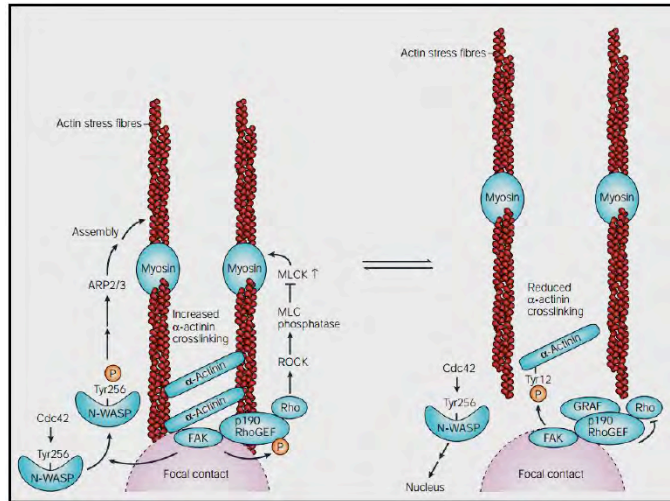


Figure 5: Focal adhesion kinase promotes cytoskeletal fluidity (Mitra et al., 2005).

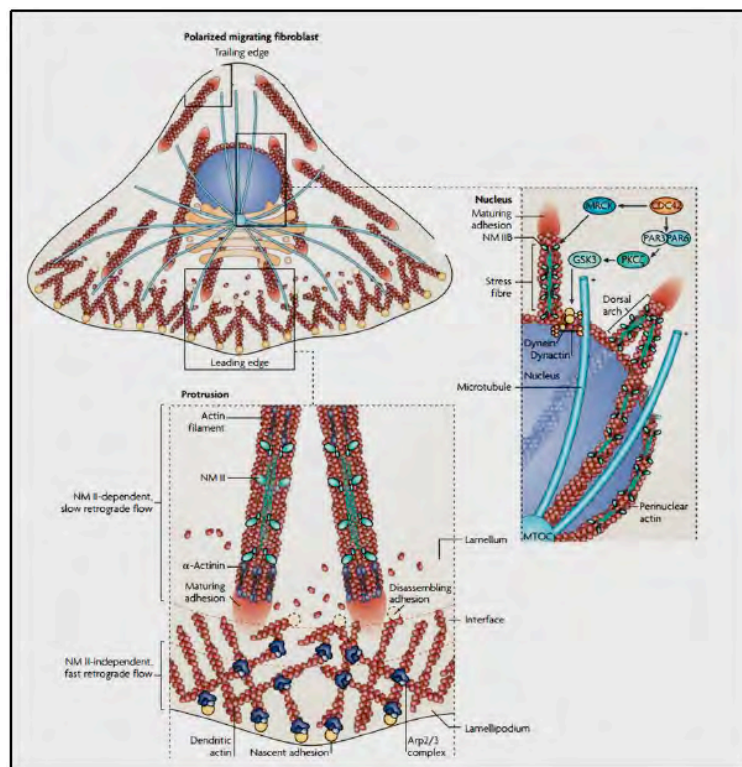


Figure 6: Multiple roles of NM II in cell migration. (Vicente-Manzanares et al., 2009).

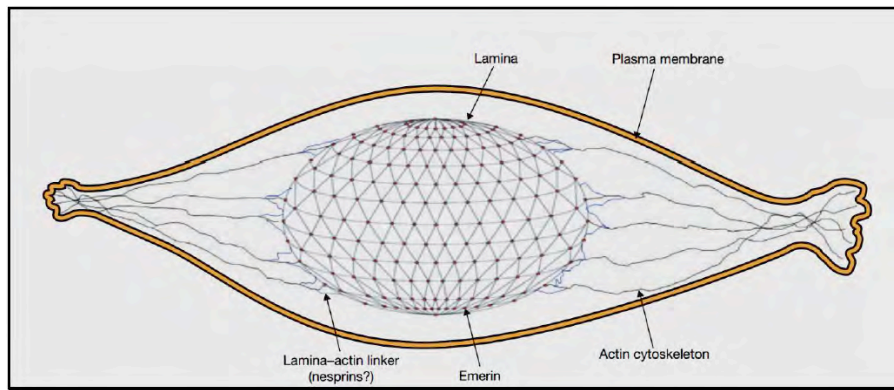


Figure 7: Tensegrity network of nucleus and its actin connection (Hutchinson et al., 2002).

Considering the connectedness of nuclear lamina proteins it is proposed that tensile properties of the lamina would radiate through the cytoskeleton to the plasma membrane (Figure 7), generating a mechanotransduction signalling capability in the cell that links the extracellular matrix to the inside of the nucleus (Hutchinson et al., 2002, 2004).

In a study of Broers et al. nuclei of fibroblasts from *Lmna*^{-/-} mice were found notably less able to resist compression compared with nuclei of fibroblasts from *Lmna*^{+/+} mice. They were able to show that the nuclei of *Lmna*^{-/-} mice exhibit isotropic deformation when compressed, whereas *Lmna*^{+/+} mice exhibit anisotropic deformation. These imply that nuclei of cells lacking A-type lamins were unable to respond to the polarity of the cell and it is a direct result of disorganization of cytoskeletal elements around the nuclear envelope (Broers et al., 2004).

The nuclear lamina could be described as a ‘tensegrity element’, which is able to resist forces of deformation and at the same time protects chromatin from physical damage. This kind of tensegrity elements has several functions. Altering the spacing and arrangement of the struts could change the shape of the shell (cell nucleus) markedly (Figure 7) (Hutchinson et al., 2002).

Organization of the genome and composition of the nuclear matrix change in response to many environmental factors (Nickerson et al., 1996). Many DNA regulatory proteins were shown to have a structural role in the nucleus. Stein et al. showed that RuNX, which is crucial for osteoblast differentiation and chromatin structure modification linked different regions of the chromosome and facilitated combinatorial control of gene transcription (Stein et al., 2007).

Collins et al. demonstrated that when 1.8 Pa stress was applied over a focal adhesion, Src was activated in microseconds to an extent similar to stimulation by 0.4 ng/mL EGF over minutes. This highlights the fact that stress induced signal transduction is 40 times faster than growth factor induced signal transduction (Figure 8) (Wang et al., 2009).

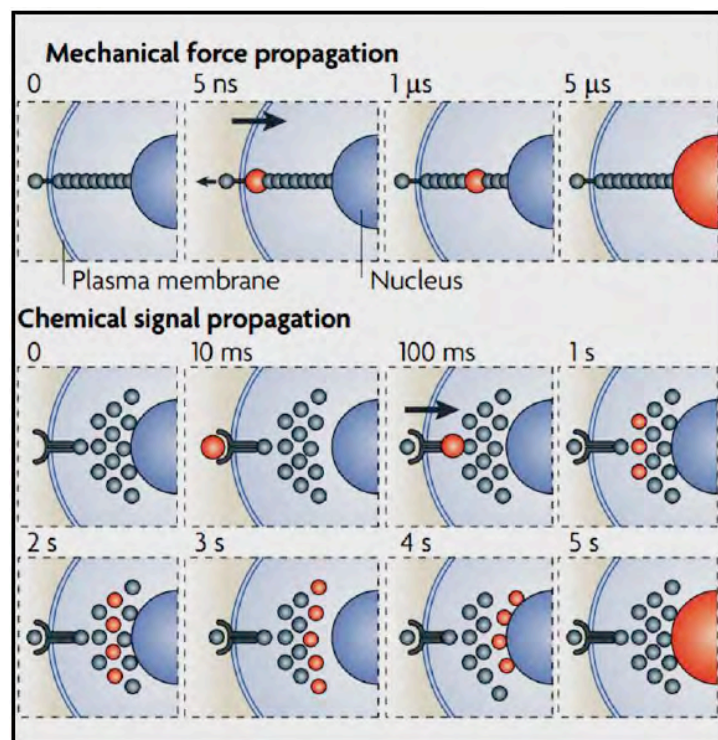


Figure 8: Signal transmission rates of mechanical and chemical signals (Wang et al., 2009).

This resulted in a paradigm shift on mechanical-chemical signal transduction in the cell, resulting from simultaneous activations of molecules at remote sites in the cytoplasm and local sites characterized by localized mechanical stress producing transduction at order of magnitude differences than known chemical signaling models. Thus, forces that are transmitted over the LINC complex and channeled over nuclear scaffolds might be focused directly on crucial DNA regulatory enzymes and binding factors directly alter gene expression and protein isoform expression through sequestration or modification of the transcription or splicing factors (Figure 9) (Wang et al., 2009).

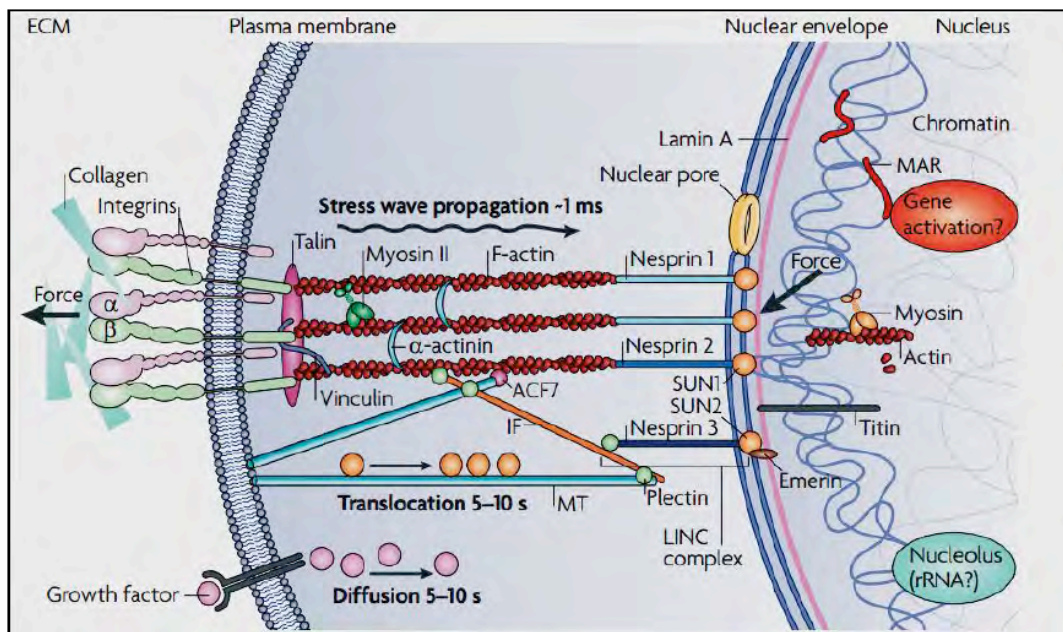


Figure 9: Force transduction from outside in (Wang et al., 2009)

1.2. Biomaterials and micro and nano patterns: Production and use in biomaterials and cell-substrate introduction

1.2.1. Biomaterials for studying surface patterns

Polymers are the largest class of biomaterials and are being applied in many biomedical applications. They have multiple purposes. This property is attributed to the ease of polymer design which can result in a wide variety of structures with desired physical, chemical, surface and biomimetic properties. In the last fifty years polymer science introduced new and wide range of reactions to discover and synthesize novel polymeric biomaterials. Additionally, recent developments in the field of tissue engineering and drug delivery accelerated the search for more efficient, biocompatible and biodegradable polymers (Eke et al., 2015).

Biocompatibility is related to the behavior of a given biomaterial in desired application site in the body. It describes an interaction of biomaterial and organism such that no toxic effects or immune response is elicited. Many classes of polymers show good biocompatibility so that in many applications polymers are becoming the first choice, and even in some cases less biocompatible classes of materials are coated with polymers to minimize host reactions.

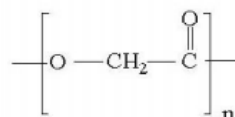
Biodegradability of a material is defined as the capability of being decomposed by biological agents. It is a desired property in cases where the implanted biomaterials need not to be removed or for the biomaterial to show intended function slow breakdown is necessary.

One of the largest classes of polymers possessing both biocompatibility and biodegradability properties is aliphatic polyesters. In 1930's Carothers' work showed synthesis of aliphatic polyesters by polycondensation of diols with carboxylic acid. However due to low melting points and difficulty in obtaining high molecular weight polymers, wide usage of aliphatic polyesters as polymeric materials was not favored (Okada 2002). Today ring opening polymerization is preferred when higher

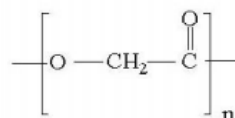
molecular weights are desired (Vroman et al., 2009). Many types of biodegradable polyester can be synthesized from ring opening polymerization of six or seven membered lactones.

Most common aliphatic polyesters are poly (glycolic acid) (PGA), poly (lactic acid) (PLA), poly(lactic acid-co-glycolic acid) (PLGA), poly(ϵ -caprolactone) (PCL), poly (butylene succinate) (PBS) and an aliphatic polyether ester poly(p-dioxanone) (Figure 10) (Gunatillake et al., 2003). PGA is synthesized by ring opening polymerization of a cyclic lactone, glycolide. It is highly crystalline with a melting point (T_m) of 220-225 °C and a glass transition temperature (T_g) of 35-40 °C (Daniels et al., 1990). It has excellent mechanical properties. PLA is usually synthesized by polycondensation of D- or L-lactic acid or from ring opening polymerization of lactide. It is a hydrophobic polymer owing to $-\text{CH}_3$ side groups with a T_g of 60-70 °C (Daniels et al., 1990). If crystallinity is desired L- form should be preferred (PLLA) while poly(DL-lactic acid) (PDLLA) is amorphous (Athanasidou et al., 1996). In order to modify mechanical properties and degradation profile copolymers of PLA and PGA, PLGA variants can be synthesized. Depending on the lactic acid: glycolic acid ratio amorphous (25:75) to semi-crystalline (80:20) copolymers can be obtained.

Poly(glycolic acid)



Poly(lactic acid)



Poly(lactic acid-co-glycolic acid)

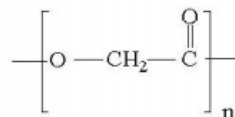


Figure 10: Structures of PLGA, PLA and PLGA (Gunatillake et al., 2003)

Poly(methyl methacrylate) is a non-degradable, transparent, thermoplastic polymer. It is commonly used in biomedical applications as well as industry. It can be synthesized using emulsion, solution and bulk polymerization methods and depending on the method used its tactility can be controlled (Salomone, 1998). It is commonly used for ophthalmologic applications due to its transparency and machinability and in orthopedic applications for its mechanical properties. It is also favored in surgical applications due to the commercialization of self-polymerizing PMMA bone cements (Navarro et al., 2008). Recently, it also became popular in MEMS and microfluidics applications due to its machinability and transparency (Li et al., 2009; Hong et al., 2010; Rizvi et al., 2013).

1.2.2. Surface patterning technologies at micro and nano level

Most commonly used micro and nanofabrication techniques are: photolithography, soft lithography, film deposition, etching, bonding, electron beam lithography (EBL), focused ion beam lithography, colloid monolayer lithography, molecular self-assembly and rapid prototyping. Of all these methods, photolithography, soft lithography, and EBL is most preferred methods for producing micro and nanopatterned surfaces.

Photolithography is the process of generating a desired pattern on the substrate surface through exposing regions of a light-sensitive material to UV light (Betancourt et al., 2006). Soft lithography, is a method to transfer a pattern onto a substrate surface. A microstructure replica is produced by molding the polymer (eg: poly(dimethyl siloxane) (PDMS)) to the master, which is manufactured by other techniques like photolithography (Li et al 2003).

1.2.3. Need for patterned substrates to study cell and nucleus

Developments in surface patterning technologies at micro and nano-scale paved the road to the study of cell-surface interactions from a completely novel point of view. Creating topographies with geometrical micro and nanopatterns, like channels, pillars

and pits with controlled dimensions became possible through the use of various methods (Hasirci et al., 2006). Cells cultured on these two-dimensional structures show various conformational changes ranging from alignment to deformation. In the study of Han et al. cells were seeded on surfaces with different micropost densities and coated with a hydrophobic polymer and fibronectin. Their results show that force generation by a cell through focal adhesions can be modulated by substrate stiffness, spread area and post density (Han et al., 2012). In the last few decades engineering topographies for generating better cell-substrate attachments, cell differentiation and proliferation for tissue engineering has been studied in detail (Rajnicek et al., 1997, Ber et al., 2005, Charest et al., 2007, Karuri et al., 2008, Zorlutuna et al., 2008, Biela et al., 2009, Lu et al., 2009, Franco et al., 2011).

These topographical cues not only distort and deform cell but also affect the nucleus within. Recent studies demonstrated that particular cell types are more prone to nuclear deformation. In the study of Davidson et al. it was shown that cell nuclei deform under the stress generated by patterned substrates (Davidson et al., 2009). In another study, it was shown that nuclei of cancer cells extensively deform under patterned substrates unlike the healthy cells (Davidson et al., 2010). This suggests a difference in both the mechanotransduction and signaling between the cancer and healthy cells and opens the door to the possibility of recognition of cancer cells through substrate. Recently a study showed similar nuclear shape deformations with bone marrow stem cells (BMSCs) (Pan et al., 2012). In the study of Badique et al. it was correlated that invasion capacity of a cancer cell is related to their deformation capacity and this can be measured by engineering a patterned surface which can deform cell nucleus (Badique et al., 2013).

1.3. Cancer cell mechanics and micropatterned substrates

Recent studies in the literature reported that osteosarcoma cells with different metastatic potentials (MG-63 and Saos-2 cell lines) showed nuclear deformations on physically patterned polymeric surfaces (Davidson et al., 2009; 2010). Non-cancerous, immortalized cells, also showed a time dependent deformation and

orientation but no nuclear deformation was observed even after 48 h of contact with such surfaces. This osteosarcoma cell nucleus deformation was explained as a reflection of the increased flexibility and deformability of cancer cells, a property that was stated to increase with the neoplastic grade of a tumor (Darling et al., 2007; Pachenari et al., 2014). The high nuclear deformability of cancer cells was explained at the molecular level as a sign of altered lamin and nesprin expression, and/or a more open chromatin configuration (Friedl et al., 2011).

The gold standard for cancer diagnosis is pathological examination of biopsy, cytology or surgical specimens. Specimen collection method, amount collected, and proximity of the specimen site to the lesion are all parameters that affect diagnostic yield of conventional pathological examination, which is further complicated by the fact that the final diagnosis depends on the interpretation of the pathologist. In certain cases, agreement between pathologists can be very low. One study found that given the same data, and a set of standardized evaluation criteria, agreement between 6 pathologists was only 58% for breast cancer diagnosis (Schnitt et al., 1992). This demonstrates the need for computer-assisted pathology and the importance of computational diagnostic algorithms (e.g., Begelman et al., 2006; Yang et al., 2009; Chang, 2012 etc.) and commercialized systems for gynecological cytology specimens. Currently, a tool that analyzes cells without standard histological preparations like embedding, sectioning and dyeing, whose use is not limited to cervical pathology (e.g., FocalPoint (Beckton Dickinson) (Wilbur et al., 2009), and the ThinPrep (Hologic) (Chivukula et al., 2007)) is not in use. Kitchener et al. (2011) found that computer assisted cervical screening was not cost effective when compared to manual readings, in addition to having significantly reduced sensitivity, and recommended against its introduction to UK health-care system (Kitchener et al., 2011).

1.4. Aim, Approach and Novelty of the Study

The hypothesis of this study is that micropatterned substrates activate the intracellular mechanotransduction pathway, resulting in a series of coordinated

events. In order to show this the effect caused by micropatterned substrates on cellular processes like adhesion, proliferation, focal adhesion signaling, cell cycle and epithelial-to-mesenchymal transition (EMT) would be studied using material science and molecular biology tools. In mechanotransduction focal adhesion related proteins are activated and the force is transferred to the nucleus causing nucleus to deform and cell cycle and cell fate related genes change. Mechanotransduction and deformation of the nucleus could modify gene expression through transcriptional control. In order to test the hypothesis, a multistep approach was planned involving an array of micropatterned substrates containing a range of pillar dimensions and interpillar spacings. The responses of different cell types to micropatterns on substrates were tested to find the ideal surface geometry to induce highest level of deformation of cell nucleus. An algorithm was designed to quantify nuclear deformation levels and the forces generated by cells while attaching to the micropillars a series of polymer blends. The outcomes of the cell-material interactions were assessed using molecular biology tools such as RT-qPCR and PCR arrays and total RNA sequencing. Expression of selected genes was quantified. Distribution and quantification of expressed proteins were achieved by immunocytochemistry.

The novelty of this study lies in the systematic design of surfaces that allow investigation of the cell-micropatterned substrate interactions and forces generated during these interactions in a controlled manner using highly controlled surface feature geometry, dimensions, and mechanical properties. The graded nature of the pattern dimensions that expose effective patterns, the custom-made algorithm used to quantify deformation levels of cell nuclei, implementation of complex models for beam bending that quantify forces that cells generate constitute the novelty of this study.

CHAPTER 2

MATERIALS AND METHODS

2.1. Materials

Silicon wafers were produced by Dr. Pu Chen with MEMS technology at Prof. Utkan Demirci's Bio-Acoustic MEMS in Medicine Laboratory, at Canary Center at Stanford for Cancer Early Detection (Palo Alto, CA).

Sylgard 184 Silicone PDMS polymer and Sylgard 184 Curing agent were bought from Dow Corning Company (UK).

Bovine serum albumin (BSA), sodium azide (ReagentPlus[®], ≥99.5%), sodium cacodylate (pH 7.4), glutaraldehyde (25%), 4',6-diamine-2-phenylindole dihydrochloride (DAPI), Amphotericin B, 1,4-Piperazinediethanesulfonic acid, Piperazine-1,4-bis(2-ethanesulfonic acid), Piperazine-N,N'-bis(2-ethanesulfonic acid) (PIPES), 100 U/mL penicillin and 100 µg/mL streptomycin, PMMA (mw~120000) were purchased from Sigma-Aldrich (Germany and USA).

McCoy5A, DMEM High Glucose, DMEM Low Glucose, RPMI 1640, DMEM High glucose colorless cell culture medium, Fetal bovine serum (FBS), L-glutamine, ascorbic acid and goat serum was purchased from Lonza (USA).

Triton X-100 was purchased from AppliChem (USA).

Alexa Fluor 488 goat anti-mouse IgG, Alexa Fluor 532 goat anti-mouse IgG, Alexa Fluor 647 goat anti-mouse IgG, Alexa Fluor 488 goat anti-rabbit IgG, Alexa Fluor 532 goat anti-rabbit IgG, Alexa Fluor 647 goat anti-rabbit IgG, Alexa Fluor 488 Phalloidin, Alexa Fluor 532 Phalloidin and Alexa Fluor 647 Phalloidin were purchased from Invitrogen (USA).

PCR primer was synthesized at Sentegen (Turkey).

Primary antibodies for Lamin A (Mouse monoclonal [133A2]), Anti-Paxillin antibody [5H11] (ab3127), Anti-alpha Tubulin antibody [4G1] (ab28439), DRAQ5™ 50 µl (5mM) (ab108410), Anti-GAPDH antibody (ab9485), Anti-COX IV [mAbcam33985] antibody, Anti-FAK antibody [EP695Y] (ab40794), Anti-FAK (phospho Y397) antibody [EP2160Y] (ab81298) were bought from Abcam plc (UK).

Poly(lactic acid-*co*-glycolic acid) (PLGA) 85:15, poly(*l*-lactic acid) (PLLA) ($\eta \approx 2.9$) were bought from ForYou Company (China).

2.2. Methods

2.2.1. Preparation of micropatterned silicon wafers

SU-8 micro-pillar array chips were fabricated using a standard photolithography procedure (Figure 11). A fresh silicon wafer (4-inch, University Wafer, MA) was used as the substrate. The silicon wafer was first cleaned in organic solvents (acetone for 15 s, isopropanol for 15 s), dehydrated (185°C, 5 min), cooled down with nitrogen, and further cleaned by oxygen plasma (oxygen flow rate: 20 cm³.s⁻¹; chamber pressure: 380 mTorr; power: 150 W, 3 min). Subsequently, the wafer was spin-coated with OmniCoat™ (MicroChem) (13 nm, 3000 rpm, 30 s) and cured (200°C, 1 min) to improve SU-8 adhesion to the substrate. After that, the wafer was spin coated with a 10 µm thick layer of SU-8 2100 photoresist (MicroChem) (1900 rpm, 45 s with a ramp rate of 500 rpm.s⁻¹), baked (65°C for 1 min, and 95°C for 2 min) and performed with edge bead removal. The SU-8 was exposed to UV (i-line, 140 mJ.cm⁻² using a SUSS MA6 Mask Aligner) through a custom designed

photomask (Fineline Imaging, CO). Photomask was tightly pressed on the solidified photoresist layer during the UV exposure to achieve an undistorted pattern transfer. The UV-exposed SU-8 was baked on a hot plate (65°C for 1 min and 95°C for 3 min) and gently washed with SU-8 developer (MicroChem) to remove uncrosslinked photoresist. SU-8 development time and hydrodynamic shear stress were carefully controlled to avoid destroying micropillars with high aspect ratio. Finally, the developed SU-8 structure was hardened by baking (175 °C, 5 min) and slowly cooled down to room temperature. The fabricated SU-8 structure was coated with a 10 μm layer of positive photoresist (S1822, Shipley Microposit) as a protective layer before dicing. The SU-8 patterned wafer was cut into 12 mm × 12 mm chiplets with an automatic dicing saw (Model DAD 321, DISCO, Japan) with a custom defined program. After cutting, the protective layer on the SU-8 structure was removed by successively washing with acetone and isopropanol, and the chiplets were dried with nitrogen for final use. Nine 3-D micropatterned chiplets decorated with a combination of square prism pillars with different size (4x4 μm² (P4), 8x8 μm² (P8), and 16x16 μm² (P16)) and interpillar distances (4 μm (G4), 8 μm (G8) and 16 μm (G16)) were manufactured. Thus the array consists of the following surfaces: P4G4, P4G8, P4G16, P8G4, P8G8, P8G16, P16G4, P16G8 and P16G16 (Figure 12). A control chiplet with no pillars was used as unpatterned control (UC).

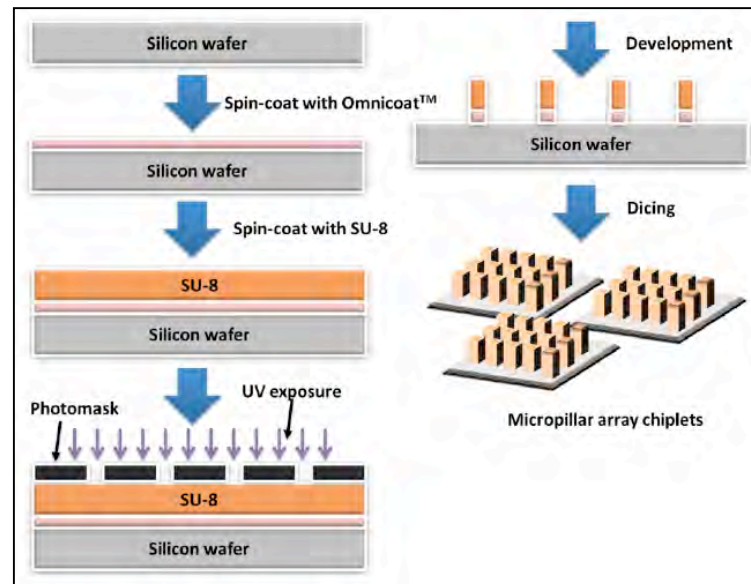


Figure 11: Production of SU-8 micropillar array chip.

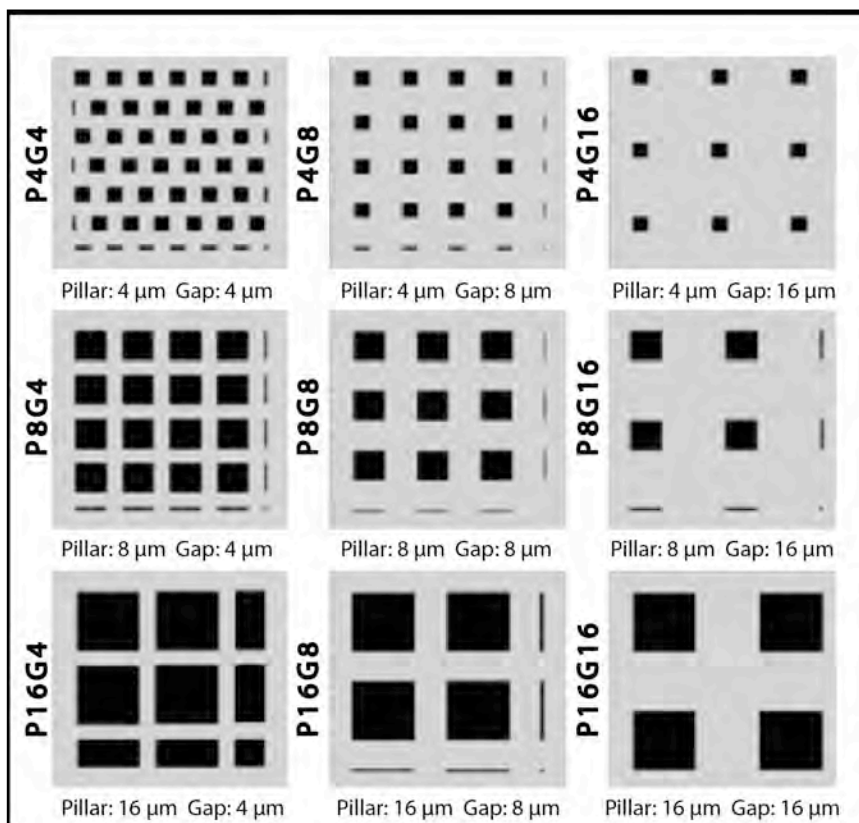


Figure 12: Representative sketch of 9 micropatterned array chips.

2.2.2. Preparation of micropatterned films

Negative copies of the wafers were molded using polydimethylsiloxane (PDMS), prepared from Sylgard 184 silicone polymer and Sylgard 184 Curing agent (Dow Corning Company, UK) mixed in a ratio of 10:1 (w/w). The silicone prepolymer mix was poured onto the patterned surface of the wafer in a petri plate, vacuum was applied for 45 min and then heated (70 °C, 4 h). After cooling, the formed PDMS structure was peeled off from the wafer producing a negative copy of the original (Figure 3). This negative mold was used to make polymer films: poly(lactic acid-*co*-glycolic acid) (PLGA), poly(*l*-lactic acid) (PLLA), PLGA:PLLA blends (50:50, 70:30, 80:20, 90:10), and poly(methyl methacrylate) (PMMA) films. A PLGA 85:15

(For You Company, China), PLLA ($\eta \approx 2.9$) (For You Company, China), or PMMA (mw~120000) (Sigma, Germany) solution in chloroform (10%, w/v) was prepared, poured onto the patterned PDMS template and air dried for 36 h (Figure 13). To prepare smooth surfaces, unpatterned PDMS molds were used. The films were stored on Teflon sheets in a desiccator at room temperature before use.

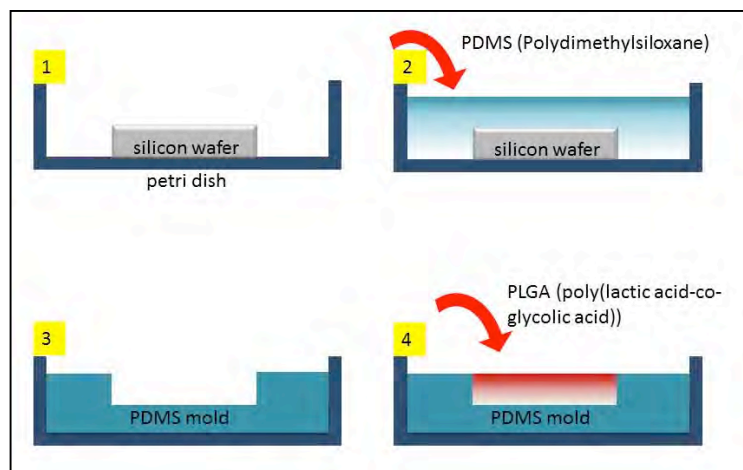


Figure 13: Preparation of PDMS molds and poly(lactic acid-co-glycolic acid) (PLGA) (85:15) micropatterned films from SU-8 micropatterned array chips.

2.2.3. Characterization of films

2.2.3.1. Surface profilometry

The characterization of silicon wafers, PDMS molds, PLGA and PLLA films were performed using an optical surface profilometer (Zygo, NewView™ 3D Optical Surface Profiler, USA).

2.2.3.2. Contact angle measurements

Water contact angles of dry samples PLGA micropatterned films (P4G4, P4G8, P4G16, P8G4, P8G8, P8G16, P16G4, P16G8, P16G16) and UC, PLLA and

PLGA:PLLA blends (50:50, 70:30, 80:20, 90:10) (P8G4, P8G8, P8G16) and UC; PMMA films (P4G4 and UC) were measured using a goniometer (*Attension, Biolin Scientific, Sweden*). 3-5 samples of each were tested using 7 μL of dH_2O . Contact angles were calculated using Young-Laplace equation:

$$\gamma_{sv} = \gamma_{sl} + \gamma_{lv} \cos\theta \quad (1)$$

where γ_{sv} , γ_{sl} and γ_{lv} were solid-vapor, solid-liquid, and liquid-vapor interfacial tensions respectively and $\cos\theta$ was the wetting angle.

2.2.3.3. Scanning Electron Microscopy (SEM)

There were two types of SEM specimens. Cell seeded and blank micropatterned films. Cell seeded SEM specimens were washed twice with PIPES (piperazine- $\text{N,N}'$ -bis(ethanesulfonic acid)) buffer (Sigma Aldrich, USA), and fixed in 4% paraformaldehyde solution for 5 min. After washing with PIPES buffer, the samples were stained with 1% osmium tetroxide (OsO_4) (Sigma Aldrich, USA), washed twice with PIPES buffer and dehydrated by immersing in an ethanol series. Cell seeded and unseeded films were coated with Au-Pd under vacuum and examined with the SEM (400F Field Emission SEM, USA).

2.2.3.4. Tensile testing

Polymer samples were produced in 50x10 mm PDMS molds with solvent casting method. PLGA 85:15, PLLA and PLGA:PLLA blends (50:50, 70:30, 80:20, 90:10) were tested. All mechanical tests were conducted on a Shimadzu AGS-X universal test machine (Japan). Crosshead speed of the load cells was 1 mm/min. Elastic modulus (Young's Modulus, E), ultimate tensile strength (UTS), and strain of the samples were calculated from the following equation:

$$UTS = \frac{F}{A} \quad (2)$$

where F was the force (N) and A was the cross-sectional area of the sample (mm^2).

Another property measured was the Elastic Modulus (E):

$$E = \frac{\varepsilon}{\delta} = \frac{F}{\Delta L} \times \frac{l}{A} \quad (3)$$

where E was the Elastic Modulus (MPa), ε was the stress (MPa), δ was the strain, ΔL was the difference in sample length (mm) and l was the initial sample length (mm).

2.2.4. *In vitro* studies

2.2.4.1. Cell culture

2.2.4.1.1. Isolation and culture of human osteoblast like (hOB) cells

After obtaining ethical committee authorization from both Gülhane Medical Military Academy (GATA) and METU for harvesting bone fragments from elective joint replacement surgery patients, specimens were taken during surgery and transferred to sterile growth medium containers and transported to tissue culture laboratory. All the isolation procedures were performed on fresh tissue. Cells were isolated using outgrowth method (Gartland et al., 2005) (Figure 14). When 90% confluence was reached cells were trypsinized and further passaged or cryopreserved until intended use. Cells were characterized for osteogenic markers osteopontin, osteonectin, osteocalcin and ALP with RT-qPCR (Data not shown) were found to be strongly positive for these markers.

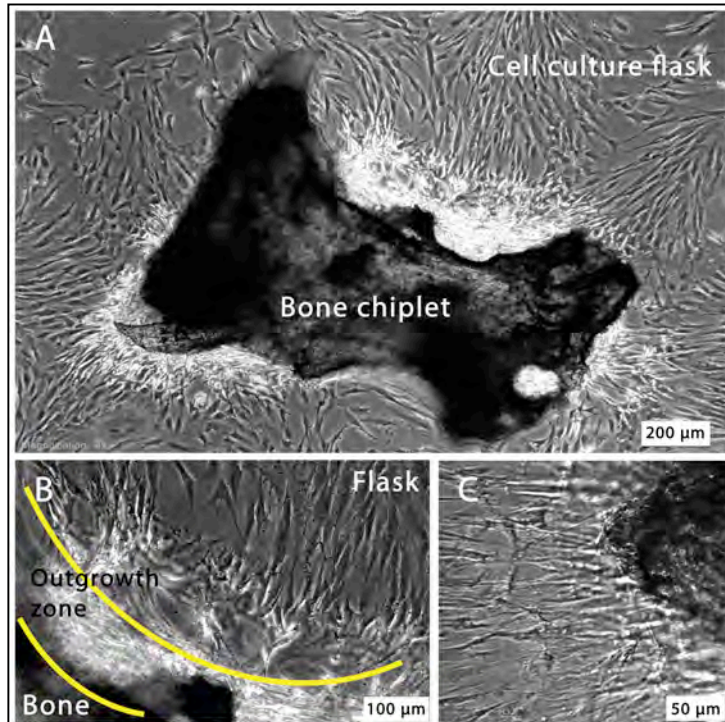


Figure 14: Primary isolation of hOB cells. (A) Cells were outgrown onto the cell culture flask from the bone chiplets. (B) After several days of culture an outgrowth zone neighbouring the bone chiplets became visible. (C) Higher magnification view of the outgrowth zone. Spindle like osteoblast cells bridging between the bone matrix and TCPS surface was observed.

hOB cells were isolated as described above and cultured in McCoy5A growth medium (Lonza, USA) supplemented with 10% fetal bovine serum (FBS) (Lonza, USA), 100 U/mL penicillin (Sigma, USA), and 100 μg/mL streptomycin (Sigma, USA), 2 mM l-glutamine (Lonza, USA), 50 μg/ml of ascorbic acid (Sigma, USA), 0.25 μg/mL Amphotericin-B (Sigma, USA.).

2.2.4.1.2. Saos-2, MCF-7, MDA-MB 231, SH-SY5Y, L929 cell culture

Saos-2 cells were cultured in RPMI 1640 medium supplemented with 10% fetal bovine serum (FBS) (Lonza, USA), 100 U/mL penicillin (Sigma, USA), and 100 μg/mL streptomycin (Sigma, USA). Saos-2 cells used in the experiments were

obtained from ATCC (ATCC No: HTB-85) and were between passages 17 and 25. The cells were cultured in tissue culture polystyrene (TCPS) flasks at 37 °C in a humidified atmosphere with 5% CO₂. The cells were removed from the culture flasks with Trypsin-EDTA, diluted to 0.05% from a 0.25% stock in PBS.

MCF-7 and SHSY5Y cells were cultured in DMEM Low glucose medium (Lonza, USA) supplemented with 10% fetal bovine serum (FBS) (Lonza, USA), 100 U/mL penicillin (Sigma, USA), and 100 µg/mL streptomycin (Sigma, USA).

MDA-MB-231 and L929 cells were cultured in DMEM High glucose medium (Lonza, USA) supplemented with 10% fetal bovine serum (FBS) (Lonza, USA), 100 U/mL penicillin (Sigma, USA), and 100 µg/mL streptomycin (Sigma, USA).

2.2.4.1.3. Cell seeding onto the micropatterned films

Micropatterned films were sterilized by exposing both sides to UV in a laminar flow hood for 25 min and then placed in 12 well tissue culture plates. Cells were seeded at a desired density suspended in 50 µL of the growth medium of choice per film (ca 64 mm²). After allowing the cells to adhere to the surfaces for 1 h; 2mL of growth medium was added into each well and plates were incubated at 37 °C and 5% CO₂.

2.2.4.2. Determination of cell viability, adhesion and proliferation by Alamar Blue assay

Alamar cell viability assay was conducted on days 1, 4, 7, 14, 21 of cell culture in order to determine the adhesion and proliferation of the cells. The study was conducted in triplicate. Cells were seeded on unpatterned films for material control, and on TCPS for positive control. Unseeded unpatterned films were used for negative control. At each time point, the medium was removed; films were washed twice with PBS and transferred to a new 12 well cell culture plate. Alamar Blue solution (10%) was prepared by using Alamar Blue (Invitrogen, USA), DMEM modified (Hyclone, USA) and 100 U/mL penicillin, and 100 µg/mL streptomycin.

After addition of 500 μL of prepared solution, 12 well cell culture flasks were incubated for 1 h at 37 $^{\circ}\text{C}$ and 5% CO_2 incubator. After incubation, 200 μL of the solution from every well were transferred to a 96 well plate and optical densities were measured at 570 nm and 595 nm with the Elisa Plate Reader. The average of 3 tests was converted into cell numbers by using a calibration curve (Appendix A).

2.2.4.3. Cell cycle analysis with flow cytometry

MDA-MB231 cells were cultured in either DMEM high growth media supplemented with 10% FBS (SM) or 0.1% FBS (SFM) (Lonza, USA), 100 U/mL penicillin (Sigma, USA), and 100 $\mu\text{g}/\text{mL}$ streptomycin (Sigma, USA). Cells were seeded onto T25 flasks and cultured for 24 with 10% FBS (24 h SM) supplemented growth medium at 37 $^{\circ}\text{C}$ and 5% CO_2 . At the end of 24 h growth media was aspirated and flasks were washed with PBS twice. Growth media with 0.1% FBS were added to flasks for cell cycle synchronization. Cell cycle progression was analyzed using FxCycleViolet (Life Technologies, USA) dye with LSR II 405 nm Violet laser 50 mW (BD, USA), after fixation with 4% paraformaldehyde for 15 min at 24 (24 h SFM), 48 (48 h SFM) and 72 h (72 h SFM). After 48 h of culture with 0.1% FBS supplemented media, it was aspirated and cells were supplemented with growth media containing 10% FBS for 4 (48 h SFM + 4 h SM), 12 (48 h SFM + 12 h SM) and 24 h (48 h SFM + 24 h SM) and cell cycle progression was analyzed. Cells were also seeded on unpatterned and P4G4 PMMA substrates after 24h of 10% FBS supplemented media or 48 h 0.1% FBS supplemented media and cultured for 24 h (24 SM or 48h SFM + 24 h SM).

2.2.5. Microscopy

2.2.5.1. Specimen preparation for fluorescence microscopy

Micropatterned films were removed from the growth medium and washed twice with PBS, the cells were fixed in 4% paraformaldehyde and permeabilized with 1% Triton-X 100 solution (Applichem, Germany).

2.2.5.2. Nuclear stains to study nuclear deformation

Micropatterned films were incubated for 5 min at room temperature with DAPI (Invitrogen, USA) or DRAQ5 (Abcam, UK) for nucleic acids.

2.2.5.3. Immunocytochemistry

Micropatterned films were prepared for fluorescence and confocal microscopy. Specimens were incubated for 1 h at 37 °C with Alexa Fluor 532 Phalloidin (Invitrogen, USA) for staining of the actin cytoskeleton. After preparation specimens were kept in dark, humidified containers until microscopic examination. For mitotic figure imaging tubulin antibody (Anti-alpha Tubulin antibody [4G1] ab28439, Abcam, UK) and Ki-67 (Anti-Ki67 antibody [SP6] ab16667, Abcam, UK) were used according to manufacturer's directions.

2.2.5.4. Confocal Laser Scanning Microscope (CLSM) and widefield fluorescence microscope imaging

Fluorescence micrographs of the cells were obtained using an upright fluorescence microscope under 350 nm, 488 nm, 550 nm or 630 nm LED sources and appropriate filter sets (Zeiss Axio Imager M2, Germany) or with an upright confocal microscope under 488 nm, 532 nm, 630 nm lasers (Leica DM2500, Germany or and Zeiss LSM710, Germany).

2.2.6. Analysis of nucleus deformation

2.2.6.1. Image-based quantification of cell deformation

Fluorescence micrographs were obtained using a Zeiss Axiovert M2 microscope equipped with x63 water immersion objective and analyzed using a custom program written using MATLAB (Mathworks Inc., Natick MA, USA) to quantify the extent of nucleus deformation on each patterned surface. Original images were in Red (R),

Green (G), Blue (B) format, and had width (W) and height (H) of 2452 and 2056 pixels, respectively. For faster processing, images were resized to 30% of their original dimensions. Only the B channel, which contained the most information, was kept to obtain a gray scale image (Ig).

2.2.6.2. Image pre-processing

We performed a number of image quality checks. First, cells with standard deviation of gray scale intensities greater than 0.5 were eliminated. These were generally out of focus cells or were unevenly illuminated due to vignetting. Then, images were binarized (Ib) using Otsu's method (Otsu et al., 1979). Cells that were attached to any of the four boundaries of the image were also eliminated, because only a fraction of these cells were visible in the photographs, and it was not possible to assess their true shape or deformation. Following this, we categorized cells based on size and those with areas that were too small (fewer than 50 pixels) or too big (larger than 1% of image H x W) were removed. As the final step, cells that were going through mitosis were identified using watershed transform (Meyer, 1994) and excluded from analysis. The remaining cells were smoothed using a Gaussian filter ($n = 5$, $\sigma = 10$) to even pixel roughness on the edges, and morphological opening was performed to eliminate any artifacts. To achieve rotation invariance, each arbitrarily oriented cell was rotated to a common orientation (Yang et al., 2008) by aligning its major axis with the y-axis, and ensuring the centroid was always on the right side of the major axis. For scale invariance, each cell was resized so that its largest dimension (H) was 64 pixels long, and its width was scaled accordingly to maintain the original aspect ratio. As a final data quality check, we re-filtered the cells with the same Gaussian kernel, followed by a median filter ($n = 3$) to eliminate salt-and-pepper noise, and also excluded cells whose pixels occupied 100% of their bounding boxes; these were likely to cause residual image processing artifacts.

2.2.6.3. Feature extraction

After pre-processing the images, we extracted two scale, rotation and translation

invariant features from binary images of cells; rectangularity and circle variance. Rectangularity (R) is the ratio of the area of the cell to that of the minimum rectangle that encompasses it, and is a measure of the compactness of the cell. The rectangularity of an ideal circle is $\pi/4$, and we subtracted this value from the rectangularity of all cells so an ideal circle would have a value of zero:

$$R = \left| \frac{\pi}{4} - \frac{A_{cell}}{A_{bounding\ box}} \right| \quad (7)$$

Circle variance (CV) is the ratio of the standard deviation (σ_R) of the radial Euclidean distances (d_i) between the centroid of a cell to each of its N boundary points, to that of their mean (μ_R), where:

$$\mu_R = \frac{1}{N} \sum_{i=1}^{N-1} d_i, \quad \mu_R = \frac{1}{N} \sum_{i=1}^{N-1} d_i \quad (8)$$

and

$$\sigma_R = \sqrt{\frac{1}{N} \sum_{i=1}^{N-1} (d_i - \mu_R)^2}, \quad (9)$$

yielding

$$CV = \frac{\sigma_R}{\mu_R}. \quad (10)$$

Circle variance is zero for an ideal circle as all distances d_i are equal to the radius of the circle, with their standard deviation being 0, and mean 1. In addition to being scale, rotation and translation invariant, use of these two simple descriptors has the advantage that data can easily be visualized using two-dimensions without the need for dimensionality reduction. Furthermore, they have low computational complexity, allowing for inexpensive hardware implementations.

2.2.6.4. Surface selection

For the purpose of identifying the surface type that induced maximal nucleus

deformation, we used micrographs of Saos-2 cells, which were known to undergo extreme deformations (Lu et al., 1999), seeded on surfaces UC, P4G4, P4G8, P4G16, P8G4, P8G8, P8G16, P16G4, P16G8 and P16G16. Following the pre-processing steps as described (Materials and Methods, Image pre-processing), we extracted CV and R from each cell and categorized them as 'undeformed' if $R \leq 0.2$ and $CV \leq 0.2$, and 'deformed' if $R > 0.2$ and $CV > 0.2$. Kolmogorov-Smirnov test was used to check the normality of distributions. Samples did not show normal distribution and revealed heteroscedastic distribution. Analyses were conducted using non-parametric Welch's ANOVA test for the first principal component of R and CV. For pairwise comparisons of samples Games-Howell *post hoc* test was used ($p < 0.05$).

2.2.6.5. Nuclear deformation on the P4G4 surface

Using only the P4G4 surface, which induced the highest level of nuclear deformation, we evaluated the diagnostic performance of our software algorithm using six different cell types: L929, Saos-2, hOB, MCF-7, and SH-SY5Y. To accurately distinguish undeformed cell populations from deformed ones, we developed a finer scoring rubric than the one we used for surface selection. We defined a *deformation score (DS)*, which combined how much the shape of a cell deviated from an ideal circle with whether it stayed more compact (e.g., like an ellipse) or obtained a bent shape (e.g., the shape of the letter "L"). To derive the parameters of this rubric, we created a database of synthesized cell nuclei. We designed 11 main cell *templates* (i.e., variants of deformed cells) we expected to see on cells on the P4G4 surface, with 50 examples of each (550 cells total). Each cell had a random orientation and scale, and was randomly filtered using Pinch, Twirl, Wave and Ripple filters in Photoshop (Adobe, Inc.) to distort and add noise, simulating actual data. Then, based on the distribution of these test data in the two-dimensional rectangularity and circle variance space, we performed gating to obtain the five regions. The regions were characterized as follows:

R1 ($R_1, CV_1 \leq 0.1, 0.1$): no deformation,

R2 ($0.1, 0.1 < R_2, CV_2 \leq 0.2, 0.2$): low deformation-more compact,

R3 (0.2, $0 < R_3, CV_3 \leq 0.5$, 0.3) low deformation-less compact,

R4 (0, $0.3 < R_4, CV_4 \leq 0.2$, 0.5) high deformation-more compact and

R5 (0.2, $0.3 < R_5, CV_5 \leq 0.5$, 0.5) high deformation-less compact.

Following this, we assigned weights to each cell based on the region it fell in $w_i=1:5$, where $i=R1$ to $R5$. These weights indicate the deformation score at an individual cell level and are used as input to calculate population-level deformation score as follows:

$$DS = \mathbf{w} * \mathbf{p}' / 100, \quad (11)$$

where \mathbf{p}' is a vector representing the percentage of cells that fall in each of the regions R1-R5. An undeformed cell population would have minimally or none deformed cells (e.g., theoretically, 100% of its cells would fall gating area #1 and receive the minimum score of $DS=1$). Similarly, a deformed cell population would have cells that deform extensively (e.g., theoretically 100% of its cells should fall in the gating area #5) and receive the maximum score of $DS=5$. Based on this convention, the *undeformed* and *deformed* classes in the Surface Selection section correspond to $DS \leq 3$ and $DS > 3$, respectively. We adopted this threshold as the cut-off between undeformed and deformed populations.

We quantified morphological differences in cell nuclei using two features extracted from binary images: rectangularity and circle variance (Equations 4-8). Rectangularity measures the ratio of the area a cell occupies relative to the area of the smallest bounding rectangle that fits around it, and is a measure of compactness. Circle variance is the ratio of the standard deviation to the mean of the distribution of distances from the centroid of the cell to each point on its perimeter. When combined, these two features quantitatively show how much a cell deviates from an ideal circle (circularity), and how it deviates from an ideal circle (rectangularity): is the morphology compact like an ellipse, occupying most of its bounding box, or has it deformed into a less compact shape like an “L”, with some unoccupied space within its bounding box. The range of deformation of severely deformable cells

varies from near-circular or elliptical shapes to “#” shapes in the most extreme cases, when the nuclei fill the entire area available to them. Throughout this range, cells can take shapes resembling the letters “T”, “L”, “U”, and “C”, bending around the pillars. Rectangularity and circle variance, both of which are scale, rotation and translation invariant, are ideal and sufficient features for quantifying deformations of cells on our micropatterned surfaces (Rosin 2004; Zhang et al., 2014).

2.2.7 Bending of Pillars

Bending of a micro pillar was modeled according to Timoshenko Beam Theory (considering bending and shear deformations) (Timoshenko, 1921). In the model, the beam is fixed to a rigid support at one end, (just like the pillars on the substrate in our case) while the tip is free. Four different load application cases were used.

Case a: point load at the free end of the beam:

$$\text{without shear} \quad \Delta_{max} = \frac{PL^3}{3EI} \quad (12)$$

$$\text{with shear} \quad \Delta_{max} = \frac{PL^3}{3EI} + \frac{PL}{A_v G} \quad (13)$$

Case b: uniformly distributed load along the length of the beam:

$$\Delta_{max} = \frac{wL^4}{8EI} \quad (14)$$

Case c: distributed load decreasing toward the tip of the beam:

$$\text{without shear} \quad \Delta_{max} = \frac{11wL^3}{60EI} \quad (15)$$

$$\text{with shear} \quad \Delta_{max} = \frac{11wL^3}{60EI} + \frac{wL}{2A_v G} \quad (16)$$

Case d: distributed load increasing toward the tip of the beam:

$$\Delta_{max} = \frac{wL^3}{15EI} \quad (17)$$

where P is the total load, A cross sectional area, E Young's modulus, G Shear modulus, w distributed load, L height of the pillar, I lateral deformation. These

$$G = \frac{E}{2(1 + \nu)} \quad (18)$$

where E is Young's modulus, and ν is Poisson's ratio.

2.2.8. Molecular biology studies

2.2.8.1. qPCR studies

2.2.8.1.1. Isolation of total RNA

MCF-7 and MDA-MB231 RNAs were isolated from cells using Masterpure RNA Purification Kit (Epicenter, USA) and RNA samples were DNase treated using DNA-free™ DNA Removal Kit (Thermo Fisher Scientific, USA) according to the manufacturers instructions. 1 µg RNA from each sample was converted to cDNA using RevertAid First Strand cDNA Synthesis kit (Thermo Fisher Scientific, USA). RNA concentrations were measured by Nanodrop 2000C (Thermo Scientific, USA).

2.2.8.1.2. Primer Design

Primers for GAPDH (glyceraldehyde-6-phosphate dehydrogenase) was selected using NCBI Primer-BLAST using accession number NM_001289746.1 respectively (Zhang et al., 2015). Primers for epithelial to mesenchymal transition markers vimentin, E-cadherine, N-cadherine were also selected using NCBI Primer-BLAST using accession numbers NM_003380.3, NM_004360.3, and NM_001792.4 respectively (Nam et al., 2012; Brozovic et al., 2015). Primers were synthesized by Sentegen (Sentegen, Turkey) according to the sequences (Table 1).

Table 3: Primer sequences

GAPDH	Forward Primer (5' – 3')	CACCCACTCCTCCACCTTTG
	Reverse Primer (5' – 3')	CCACCACCCTGTTGCTGTAG
CDKN1A	Forward Primer (5' – 3')	ATGTGGACCTGTCACTGTCTTG
	Reverse Primer (5' – 3')	CGTTTGGAGTGGTAGAAATCTG
CCNA	Forward Primer (5' – 3')	AGCTGCCTTTCATTTAGCACTCTAC
	Reverse Primer (5' – 3')	TTAAGACTTTCCAGGGTATATCCAGTC
CCNB	Forward Primer (5' – 3')	TATGCAGCACCTGGCTAAGA
	Reverse Primer (5' – 3')	CATGCTTCGATGTGGCATACT
VIMENTIN	Forward Primer (5' – 3')	CCTGCAATCTTTCAGACAGG
	Reverse Primer (5' – 3')	CTCCTGGATTTCTCTTCGT
E CADHERINE	Forward Primer (5' – 3')	TGAAGGTGACAGAGCCTCTGGAT
	Reverse Primer (5' – 3')	TGGGTGAATTCGGGCTTGTT
N CADHERINE	Forward Primer (5' – 3')	GTGCATGAAGGACAGCCTCT
	Reverse Primer (5' – 3')	ATGCCATCTTCATCCACCTT
Ki-67	Forward Primer (5' – 3')	ATTGATCGTTCCTTCAGGTATG
	Reverse Primer (5' – 3')	TCATCAGGGTCAGAAGAGAA

2.2.7.1.3. cDNA synthesis

First-strand cDNA synthesis via RT-PCR was performed with 1 µg RNA from each sample with RevertAid First Strand cDNA Synthesis Kit (Thermo Fisher Scientific, USA) and a thermal cycler () with the oligo(dT)₁₈ primers supplied with the kit. The reverse transcription step ran for 60 min at 42 °C, followed by reaction termination for 5 min at 70 °C.

2.2.7.1.4. qPCR and analysis

qPCR analysis was conducted with Saos-2 and hOB cells for osteogenic markers.

Qiagen Rotor Gene SYBR Green master mix (Qiagen, Germany) was used under the conditions 5 min 95°C (HotStarTaq activation), 30-40 cycles of 5 s denaturation at

95 °C and 10 s annealing/extension at 60 °C followed by melting. For each reaction 50 ng-0.005 ng cDNA sample was run according to manufacturers directions.

qPCR analysis was conducted for MDA-MB-231 cells for EMT markers. Promega qPCR Master Mix (Promega, USA) was used under the conditions 2 min 95°C (HotStarTaq activation), 30-40 cycles of 15 s denaturation at 95 °C and 60 s annealing/extension at 60 °C followed by melting. For each reaction 50 ng-0.005 ng cDNA sample was run according to manufacturers directions. For the evaluation of isolation quality of RNA samples RNA and for primer quality PCR products of the target gene were run on 1% and 2% agarose gel respectively. For negative controls non template and no reverse transcription reactions were performed (Appendix B).

2.2.7.1.5. *The Human Focal Adhesions RT² Profiler PCR Array*

RT2 focal adhesion PCR array (PAHS-145Z, Sabioscience, USA) was performed for hOB and Saos2 cells cultured on PLLA and PLGA unpatterned, P8G4 and P8G8 substrates for 48 h. 5 films each seeded with 50000 cells were pooled for a single RNA sample. Duplicate RNA samples were run with the array (biological replicates). Selected surfaces and tested cell types for the PCR array is given in Table 2.

Table 4: Selection of micropatterned substrate and cell type for RT2 focal adhesion PCR array.

	hOB			Saos2		
	Unpatterned	P8G4	P8G8	Unpatterned	P8G4	P8G8
PLLA	2	2	2	2	2	2
PLGA	2	2	2	2	2	2

After RNA isolation DNase treatment and cDNA synthesis were performed according to RT²Profiler PCR array kit in single step. cDNA (200ng/ rotor) was loaded to 100 well rotor with immobilized primers (Appendix C) (Parsons et al., 2000; McLean et al., 2003; Cordes et al., 2003; Persad et al., 2003; Attwell et al.,

2003; Yano et al., 2004; Playford et al., 2004; Hannigan et al., 2005; Guo et al., 2005; Blattner et al., 2005; Sawai et al., 2005; Wade et al., 2006, Legate et al., 2006). PCR reaction was conducted under the conditions 10 min 95°C (HotStarTaq activation), 40 cycles of 15 s denaturation at 95 °C and 30 s annealing/extension at 60 °C followed by melting.

Ct results were exported to an excel file and uploaded to the manufacturer's website for analysis¹. $\Delta\Delta C_t$ values, fold changes and fold regulation values were analyzed using the online tool. All PCR runs were normalized to GAPDH expression and $\Delta\Delta C_t$ values were calculated using unpatterned control PCR results for each cell type and polymer. PCR controls were read from wells H6-12.

2.2.8.2. RNA Sequencing

Following RNA isolation as described above, RNA was quality checked with Bioanalyzer (Agilent Bioanalyzer, USA) and NanoDrop (Thermo Scientific, USA). Illumina HT was performed by Dr. Gözde Durmuş as a courtesy of Prof. Ronald W. Davis and Prof. Lars Steinmetz at the Stanford Genome Technology Center using the Illumina HiSeq 2500 system.

¹ <http://pcrdataanalysis.sabiosciences.com/pcr/arrayanalysis.php> (accessed March 2016)

CHAPTER 3

RESULTS AND DISCUSSION

3.1. Characterization

3.1.1. Thermal characterization using DSC

In this study, PLLA and PLGA were used as the substrate and thermal characterization was important to learn about the differences in the organization of the polymer chains. Therefore, DSC was conducted for the thermal characterization of PLLA and PLGA 85:15 polymers. Polymers were scanned between 0-240°C and 20-80°C. 20-80°C scans were conducted in order to identify the glass transition peak (T_g). In Figure 15 an endothermic peak at 177°C was observed for PLLA indicating the melting point (T_m). This result was concordant with the literature, where Zhai et al. found T_m of the PLA ($\eta=1.24$) as 148° C and Chen et al. found T_m of the PLLA ($\eta=1.20$) as 175° C (Chen et al., 2003; Zhai et al., 2009). A melting peak is obtained because of the crystalline regions of the polymer showing that PLLA is semicrystalline in nature (Bastioli, 2005; Běhálek et al., 2013). Poly(lactic acid) (PLA) has an asymmetric α -carbon resulting in two stereochemical centers (*D* and *L*), which can form two enantiomers (Kamaly et al., 2016). It is reported that these stereo co-polymers of *D*-lactic acid and *L*-lactic acid (PDLLA or PLDLA) has lower T_m and T_g values and crystallinity compared to PLLA (Bastioli, 2005). Bastioli showed that 100% *L*-lactic acid polymer (PLLA) has a T_m of 184°C. As the *L*-lactic acid content decreases (PL,D-LA) T_m decreases to 176.2°C (98% *L*-lactic acid),

158.5°C (92.2%). Polymer becomes amorphous and T_m disappears when *L*-lactic acid content is lower than 87% (Bastioli, 2005). On the other hand, on PLGA 85:15 copolymer thermogram no prominent melting peak was observed (Figure 15). Copolymerization of lactic acid and glycolic acid into PLGA yield an equal distribution of *D*-lactic acid and *L*-lactic acid (poly(*D,L*-lactic acid-*co*-glycolic acid)) in lactic acid block resulting in amorphousness (Kamaly et al., 2016). Due to disruption of PLA chains by PGA and *D* and *L*-lactic acid forms PLGA is amorphous (Gentile et al., 2014). DSC of PLGA 85:15 tested, had no melting point hence amorphous.

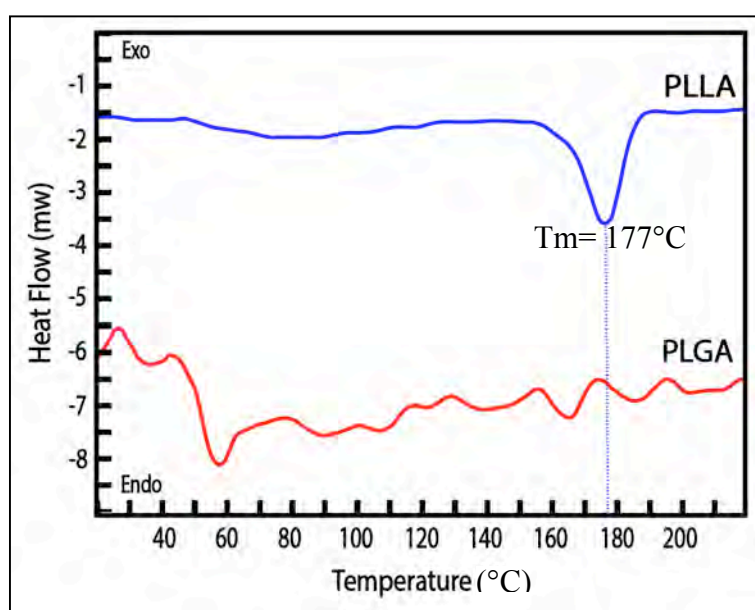


Figure 15: DSC thermograms of PLLA and PLGA polymers. Scan was conducted between 0-240°C (T_m endothermic peak was shown with dotted lines).

The scans in the 20-80°C range showed an endothermic peak at 56°C for PLLA and one for PLGA at 58°C (Figure 16). These peaks indicated the T_g of the polymers and were in accordance with the reports in the literature where Zhai et al. reported T_g of PLLA at 50-60°C, Chen et al. at 57.4°C and Makadia et al. reported T_g of PLGA above 37°C (Zhai et al., 2009; Chen et al., 2003, Makadia et al., 2011). At room

temperature and at culture conditions (37°C) both PLLA and PLGA is in glassy state. Since PLGA is amorphous it showed a large T_g peak in the thermogram (Figure 16). On the other hand, semicrystalline PLLA showed a small T_g peak.

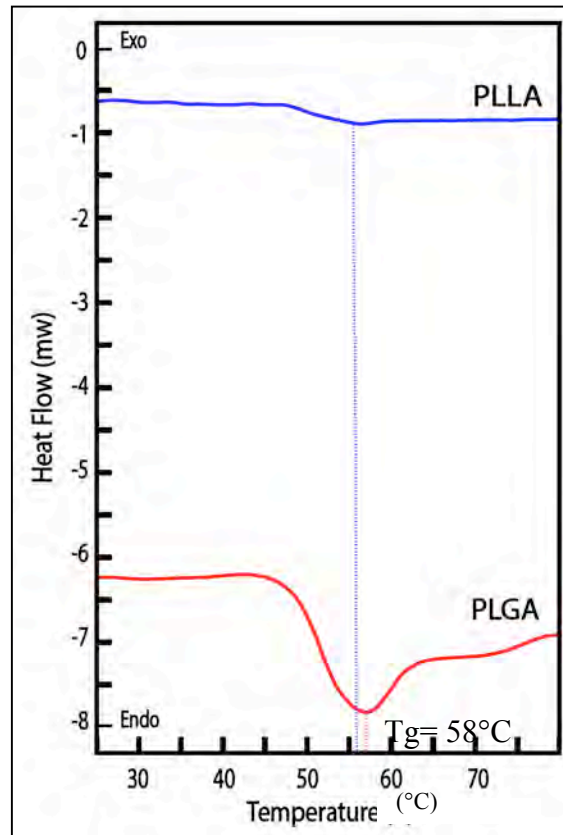


Figure 16: DSC thermograms of PLLA and PLGA polymers. Scan was conducted between 20-80°C (T_g endothermic peaks were shown with dotted lines).

3.1.2. Tensile testing

Tensile testing of polymers is an important step in finding certain mechanical properties such as stiffness (Young's Modulus), yield strength and ultimate tensile strength (UTS). Since it is reported that substrate mechanical properties influence response of the cells seeded on them, it is very important in this study (Bao et al., 2003; Nemir et al., 2010). Tensile testing of PLLA, PLGA and blends revealed a viscoelastic behavior expected from a typical polymer (Figure 17). Representative

stress-strain curve of PLLA shows higher UTS compared to PLGA, while PLGA has more percent elongation before break.

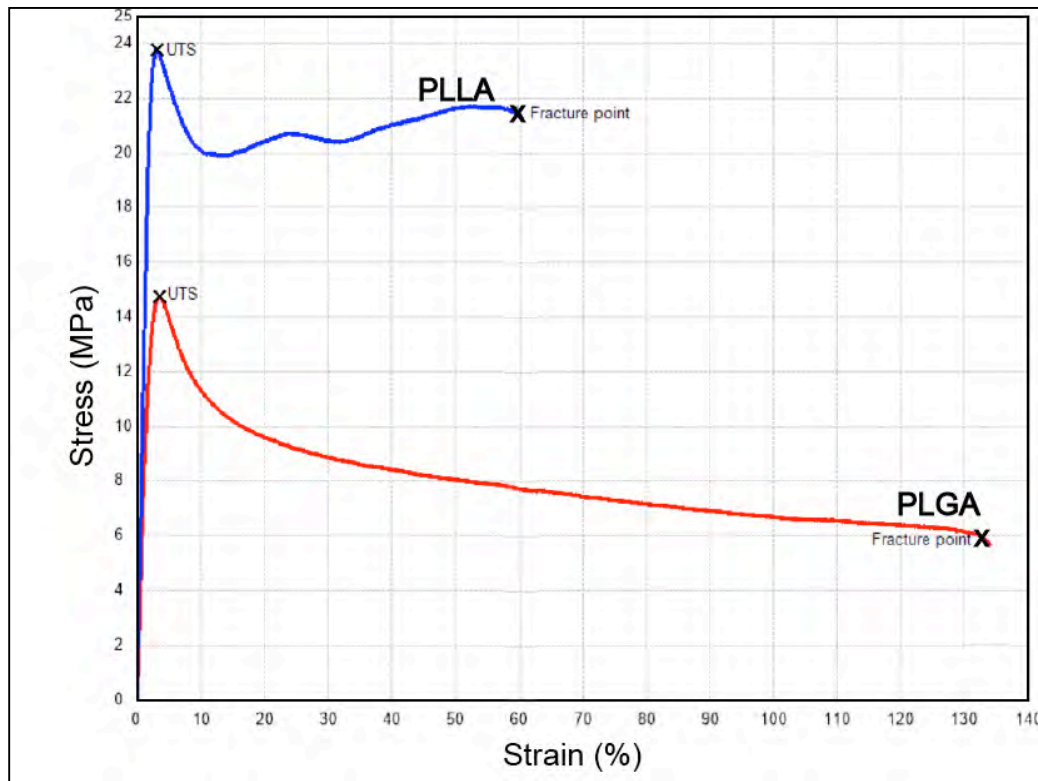


Figure 17: Representative stress-strain curves for PLGA and PLLA polymers.

Young's moduli of PLGA and PLLA blends show an increasing trend as the PLLA proportion in the blend increases (Figure 18). PLLA polymer was found to be semi-crystalline (Figure 15). Blending disrupts crystallinity and increases the amorphousness of the polymer chains in the blend. Pure PLGA is also amorphous and introduction of it into PLLA chains increases the amorphousness as observed from the difference between Young's Moduli of (100:0) and (90:10). Ultimate tensile strength (UTS) values also follow the same trend. Observed Young's moduli of the polymers and blends were lower than literature (Gentile et al., 2014). Since tested materials were prepared using solvent casting method, this drop in tensile properties can be explained by the solvent casting method (Lim et al., 2013).

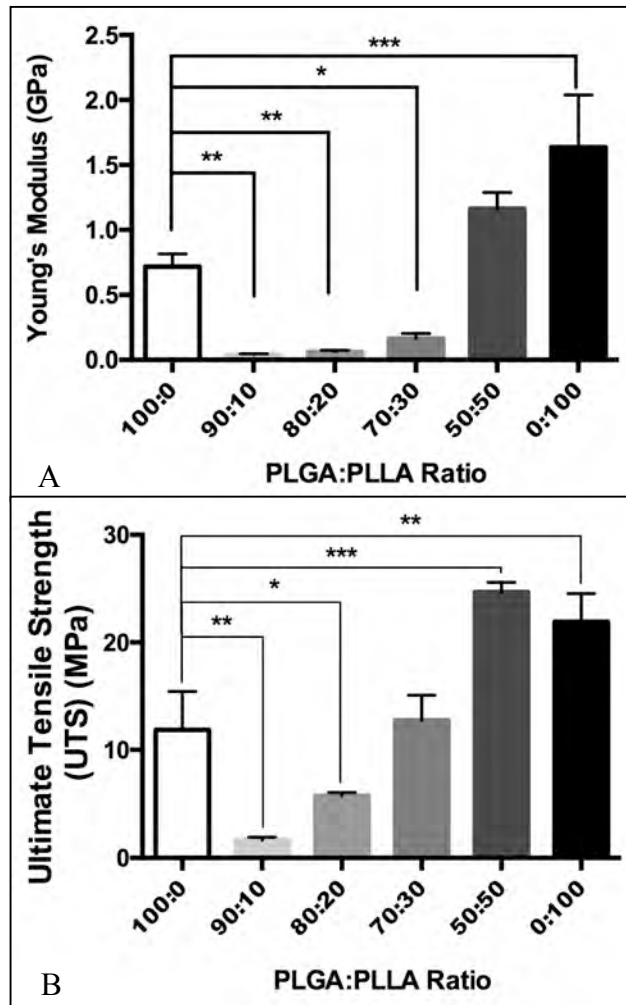


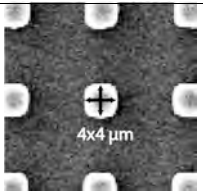
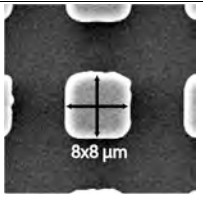
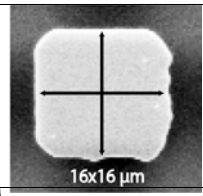
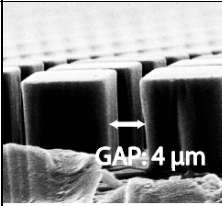
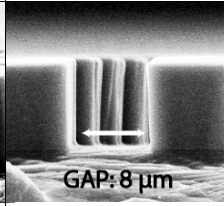
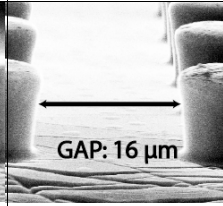
Figure 18: Mechanical property change with the composition of the polymer. (A) Young's Modulus and (B) Ultimate Tensile Strength of blends of PLGA and PLLA. Results are averages of 5 tests per sample. Statistical significance was calculated using one-way ANOVA and Tukey *post hoc* test (* $p < 0.05$, ** $p < 0.01$, *** $p < 0.005$, **** $p < 0.001$).

3.1.3. Surface design and characterization

It was observed in our laboratories and that micropatterns deformed cell nuclei (Ozcelik, 2012; Davidson et al., 2009; Davidson et al., 2010; Badique et al., 2013). It was proposed that the extend of deformations could give insight to the nature and state of health of the cells. Surfaces were designed to amplify the cellular responses and give clues about these cells. We created pillar arrays with different spatial distributions in the range of 1-25 μm . This range was selected to start from smaller than cell size to somewhat larger than cell size. It was observed in our earlier studies that low micron sized pillars with high aspect ratios deform under cellular forces (Ozcelik et al., 2014). It was also observed that features larger than a cell did not cause deformation. Taking these into consideration, we aimed to produce surfaces that would induce maximum deformation in cell nuclei and used photolithography. Nine different surfaces were produced decorated with square prism pillars $4 \times 4 \mu\text{m}^2$, $8 \times 8 \mu\text{m}^2$ and $16 \times 16 \mu\text{m}^2$ sizes and interpillar distances of 4 μm , 8 μm and 16 μm (Table 5). These surfaces were labeled according to pillar size (P) and interpillar distance (gap) dimensions (G) as P4G4, P4G8, P8G4, etc (Scheme in Table 5). SEM showed an average pillar height of $8.3 \mu\text{m} \pm 0.2 \mu\text{m}$ (Table 5).

An unpatterned control surface was manufactured using an undecorated silicon wafer (Control). To change polymer stiffness without significantly changing substrate chemistry poly(lactic acid-*co*-glycolic acid) (PLGA) was used. PLGA (lactic acid: glycolic acid 85:15), was chosen for its slow degradability ($\sim 80\%$ weight preservation in 6 weeks for high LA:GA) (Lu et al., 1999).

Table 5: Abbreviations of the surfaces according to the pillar dimensions and spacings in the array.

Pillar area (μm^2)	Gap width (μm)			
	4	8	16	
4x4	P4G4	P4G8	P4G16	
8x8	P8G4	P8G8	P8G16	
16x16	P16G4	P16G8	P16G16	
				

When equal areas of the micrographs of micropatterned arrays are selected, it is observed that the ratio of the areas at the top of the pillars to the areas outside the pillars is 0.8 regardless of the type of array. Certain pillar arrays had high aspect ratio (pillar height: pillar top dimension, AR) decorations (P4G4, P4G8, and P4G16 with AR 2.08), while others were intermediate aspect ratio surfaces (P8G4, P8G8, and P8G16 with AR 1.04) and small aspect ratio surfaces (P16G4, P16G8, and P16G16 with AR 0.58). It can therefore be stated that any differences observed between the surfaces in cell responses do not originate from occupation of the surface by the pillars (top area:base area ratio) but rather from the interpillar distances and pillar AR.

3.1.4. Surface Profilometry

In order to study the fidelity of the feature transfer process, the surfaces were studied with surface profilometry. Measurement of surface feature dimensions using the micrographs showed that during pattern transfer 93% of the feature height was retained (Wafer 9.05 μm vs PDMS mold 8.40 μm , PDMS mold 8.49 μm vs PLGA 8.30 μm) (Figure 19). The pillars were sharp and with reproducible dimensions, all being between 8 and 9 μm . It can safely be stated that the fidelity of pattern replication process was highly successful.

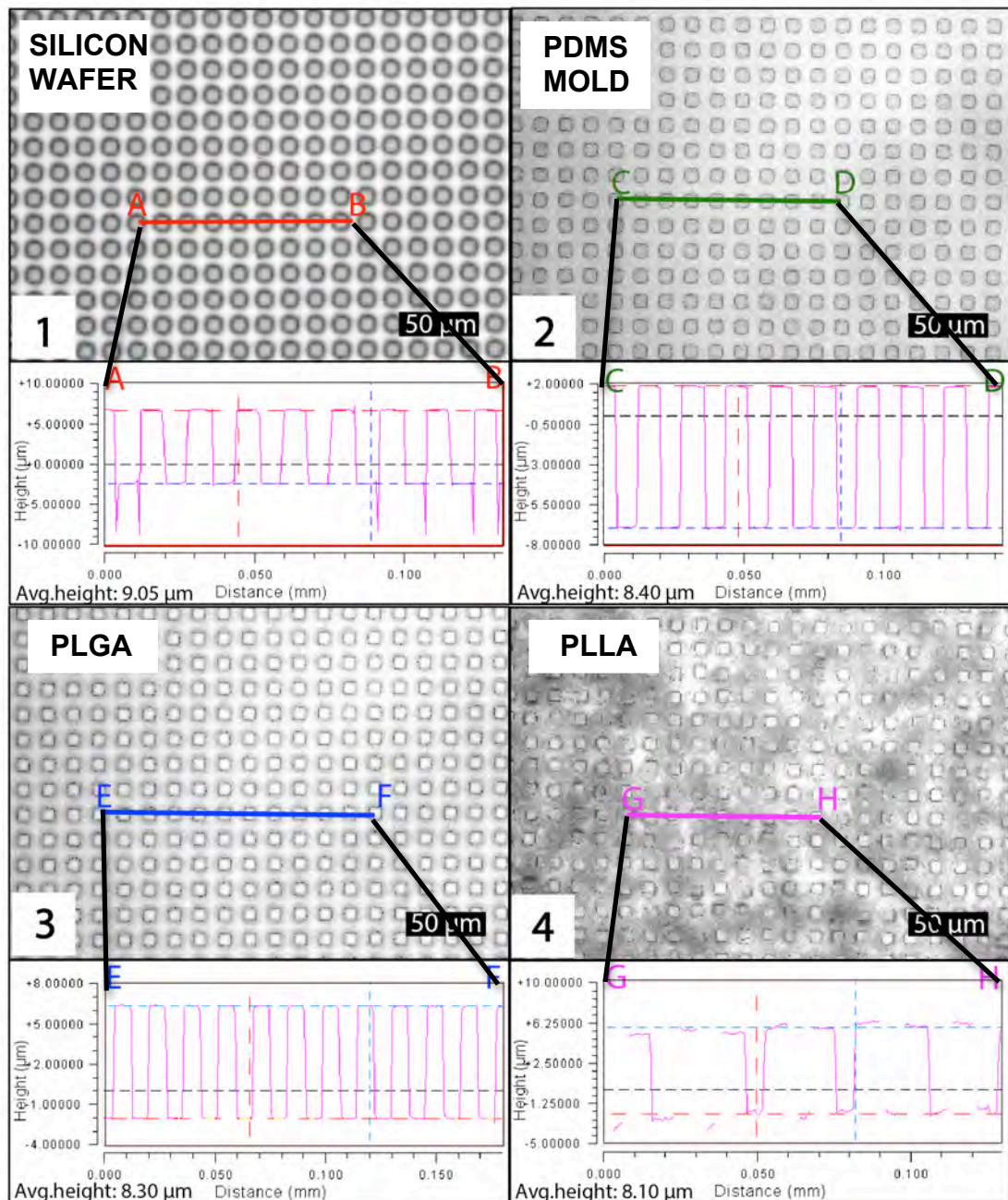


Figure 19: Surface profilometry results for various patterned surfaces. (1) Silicon wafer, the original template, (2) PDMS mold, the intermediate template or the mold, and (3) PLGA and (4) PLLA films. Top panels are the optical images of the surfaces and the bottom panels are the corresponding profilometry plots. Average heights are presented in the profilometry histograms.

3.1.5. Water contact angles and wettability

Water contact angles allow the researchers to calculate surface energy and also enable the comparison of surface wettability by liquids. In this study of PLLA, PLGA and blends of PLGA:PLLA were measured using the sessile drop method (Figure 20). Contact angles were found to be $88.45 \pm 0.78^\circ$ for PLGA:PLLA 100:0; $68.14 \pm 0.84^\circ$ for 90:10; $77.54 \pm 0.43^\circ$ for 80:20; $92.66 \pm 2.42^\circ$ for 70:30; $100.1 \pm 2.26^\circ$ for 50:50 and $79.17 \pm 516^\circ$ for 0:100. All contact angle measurements were significantly different from one another ($p < 0.0005$) except between 100:0 and 70:30 and between 80:20 and 0:100 (One-way ANOVA, $P < 0.0001$). PLGA had a higher water contact angle than PLLA (88.45° vs 79.17°) to PLLA. Ma et al. measured 82° water contact angle for PLLA films and since PLGA has glycolic acid blocks, which are more hydrophilic PLGA should have a smaller contact angle (Ma et al., 2002). In their study comparing PLGA and PLA thick films, Edith et al. found that PLGA films were slightly more hydrophobic than PLA and explained this phenomenon by the exposure of the methyl side groups to the surface of the films in PLGA but not as much in PLA (Edith et al., 2006).

For the PLGA:PLLA blends, as the lactic acid ratio in the blend increased the contact angle increased which is probably because introduction of crystalline compartment resulting in a more crystalline polymer (Liu et al., 2012). Wettability of micropatterned PLGA surfaces were analyzed using sessile drop method also. 9 micropatterned surfaces (P4G4, P4G8, P4G16, P8G4, P8G8, P8G16, P16G4, P16G8, and P16G16) and unpatterned control surface made up of PLGA polymer were tested (Figure 21).

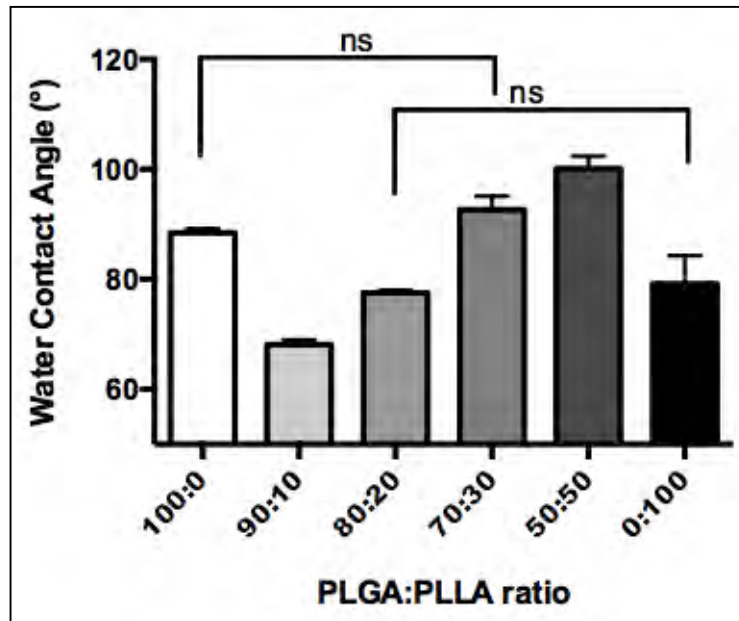


Figure 20: Water contact angles of unpatterned PLLA, PLGA and PLGA:PLLA blend films, measured by sessile drop method. (One-way ANOVA, $P < 0.0001$, $n=3$)

For each pillar size group (P4, P8 or P16), 4 μm gaps (G4) yielded the highest contact angle while 16 μm gaps (G16) the lowest. All contact angle measurements were significantly higher than unpatterned control (One-way ANOVA, $p < 0.0001$, $n=3$).

Within each pillar size group (P4, P8 and P16) contact angles of different gap sizes (G4, G8 and G16) were significantly different (One-way ANOVA, $p < 0.005$, $n=3$). P4 and P8 group has similar contact angles for the same gap dimensions. P16 group had the highest CA of all (Figure 21). Unpatterned PLGA ($88.45 \pm 0.78^\circ$) is borderline hydrophobic ($\approx 90^\circ$) and surface patterning apparently leads to increased hydrophobicity. On P16G4 surface CA ($146.5 \pm 3.03^\circ$) approaches superhydrophobicity ($\geq 150^\circ$).

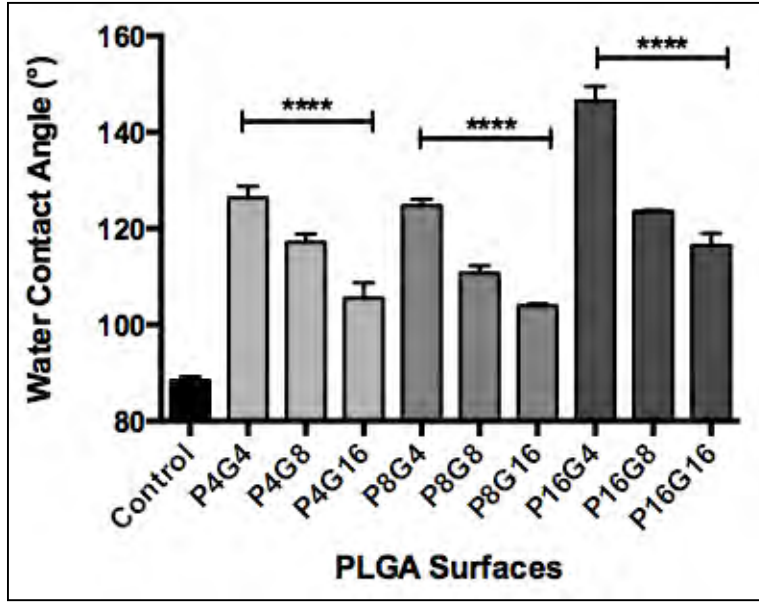


Figure 21: Water contact angles of mictopatterned PLGA films measured by sessile drop method. (One-way ANOVA, $P < 0.005$, $n=3$).

Superhydrophobicity is known to be induced by surface roughness and this is called the Lotus effect (Zheng et al., 2014). When a droplet is placed on a rough surface (micropatterns in this case) wetting can be explained by either Wenzel's (Wenzel 1936) or Cassie-Baxter's (Cassie et al., 1944) approach. In Wenzel state, the liquid fills the surface grooves and ridges, while in Cassie-Baxter the water droplet is attached to the surface while still on top of the grooves and ridges and allows formation of air pockets. Generally, one of these states is stable for a surface depending on roughness and chemistry parameters while the other state is metastable (Zheng et al., 2014). Wenzel (19) and Cassie-Baxter (20) states use the following equations to calculate apparent contact angle θ^* :

$$\text{Wenzel state: } \cos\theta^* = r\cos\theta \quad (19)$$

$$\text{Cassie-Baxter state: } \cos\theta^* = -1 + (1 + \cos\theta)f \quad (20)$$

where r is the ratio of the wet surface area to its projection on the apparent solid

plane, and f is the area fraction of the wet part of the solid (Zheng et al., 2014). When a systematically decorated surface is in question (like micropatterns) the crosssection of a pillar (square in our study) introduces a new parameter to the equation. Since neither Wenzel nor Cassie Baxter state has this shape parameter (S), in the recent studies known equations were modified to include this geometrical parameter (22) (Wong et al., 2009; Zheng et al., 2010):

$$\cos\theta^* = -1 + (1 + \cos\theta)\left(1 - \frac{l_{cr}}{S}\right)f \quad (21)$$

Where l_{cr} is the critical parameter. In the hypothetical case where $S \leq l_{cr}$ CA will get close to the extreme value of 180° ($\cos 180^\circ = -1$) since $\left(1 - \frac{l_{cr}}{S}\right)$ approaches 0. Shape parameter is defined as:

$$S = a/4 \quad (22)$$

for a pillar with a square cross section, where a is the edge length of the square (Zheng et al., 2014). Together with this parameter pillar size and spacing found to be influential on contact angles. In their study, Zheng et al. showed that $30 \mu\text{m}$ size square pillars with $30 \mu\text{m}$ spacing resulted in a water contact angle of 144° while decreasing the spacing to $20 \mu\text{m}$ increase CA to 153° (Zheng et al., 2010). Apparently the dimension factor (S) reflecting the shape, pillar and gap sizes are all influential on the wettability of rough surfaces. Smaller S , pillar size or gap size higher the observed water contact angle (Zheng et al., 2010). Our results are in agreement with these previous studies in the literature.

3.2. Isolation of Human Osteoblast Like Cells (hOBs)

In order to test the patterned surfaces with healthy human cells bone explants were obtained from consenting donors. Bone explants in the form of small fragments were cultured over a month. Cells migrating from bone matrix were observed using a phase contrast microscope (Figure 22). Morphology of the first passage of the hOB cells were observed with a fluorescence microscope by staining for cytoskeletal elements (actin and tubulin) and DNA (Figure 23). Morphology of these cells were compared with those in the literature and were found to be similar to with osteoblast-like cells (Rickard et al., 1996; McManus et al., 2012).

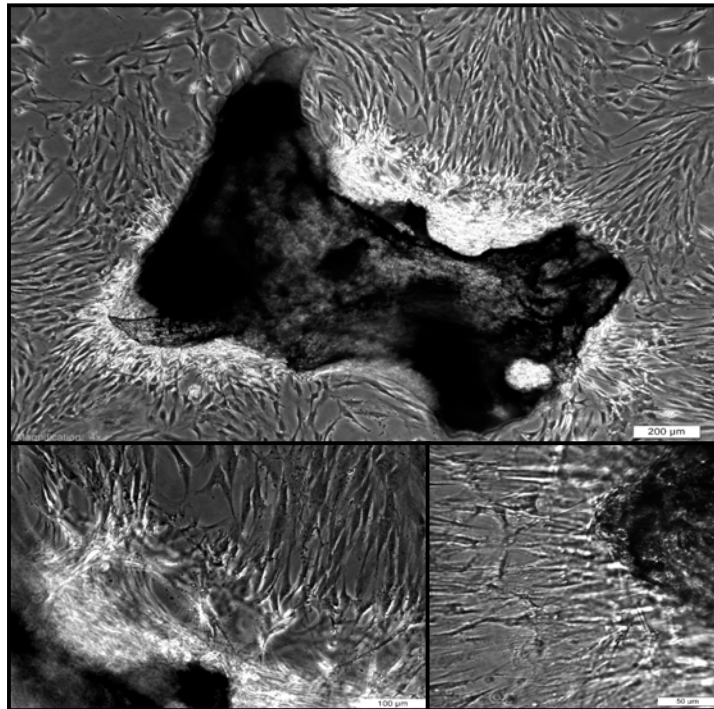


Figure 22: Human osteoblast like cells (HOB) were isolated from surgical bone explants by incubating for a month in culture medium. Osteoblasts started to migrate out of the spongy bone on to the TCPS surface at the 2nd week and reached confluence at around 1 month.

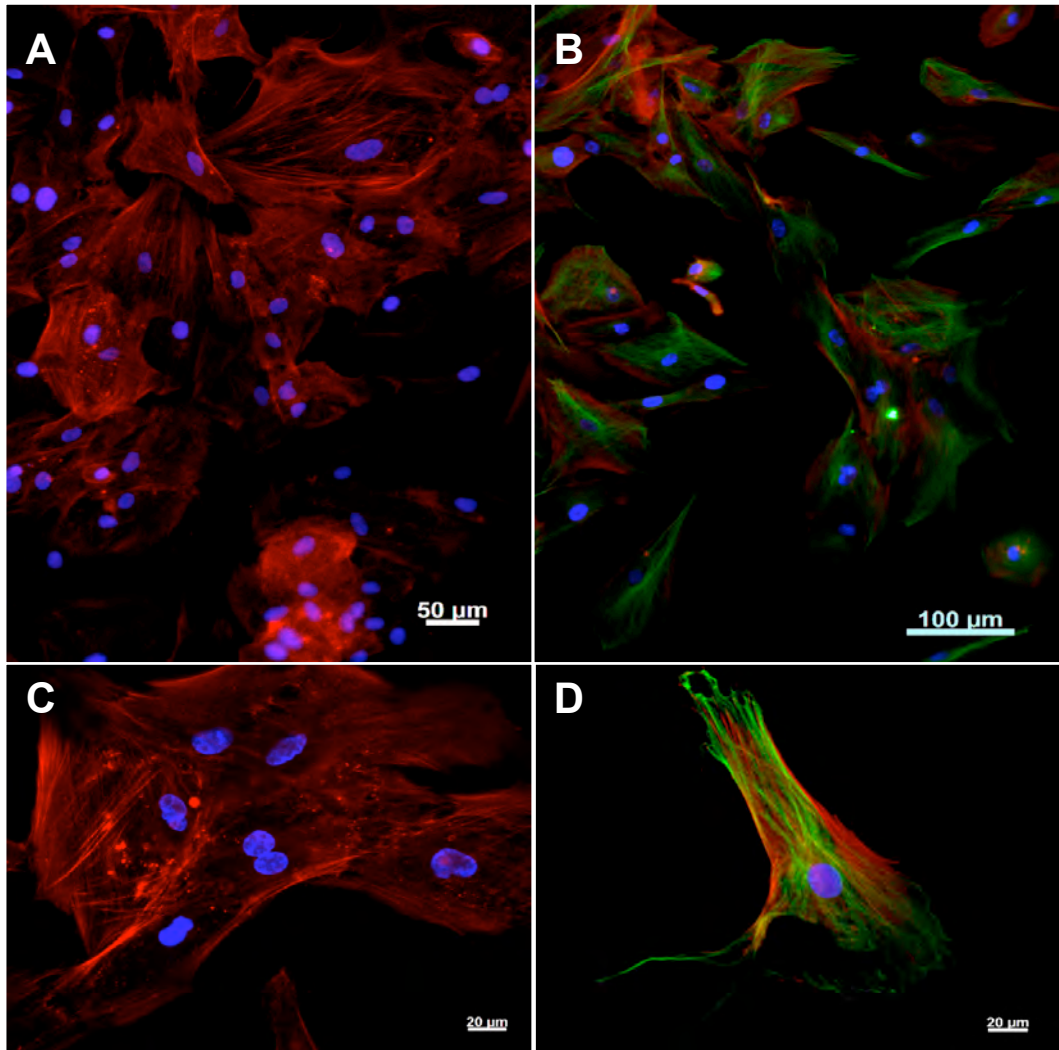


Figure 23: Fluorescent microscopy images of HOB cells. (A-C) Actin cytoskeleton and nucleus (x10 and x63 objective). (B-D) Actin and tubulin cytoskeleton and nucleus (x10 and x63 objective). HOB cells have small nuclei and large cell surface on unpatterned surfaces. (red: actin/Alexa Fluor Phalloidin 532, blue: DNA/DAPI, green: tubulin/Anti-tubulin Ab-Alexa Fluor 488)

3.3. Nucleus Deformation on Micropatterned Substrates

Deformations of the cell nuclei were studied using a micropatterned substrate array (Figure 24). In order to design the surface structure parameters like pillar size, gap dimension or pillar height a literature review was conducted. Previous studies in the literature reported that cancer cells with different metastatic potentials (MG-63 and Saos-2 cell lines) show nuclear deformations (Davidson et al., 2009, 2010) on micropatterned polymeric surfaces with pillar dimensions ranging from 2-25 μm . nuclear elasticity as reflected in the cell shape.

Nuclei of the stem cells were shown to deform on micropatterned surfaces with pillar dimensions ranging from 0.2 to 5 μm (Pan et al., 2012). Healthy immortalized cells, on the other hand, showed a time dependent deformation but deformations were transient and disappeared at 48 h of culture (Davidson et al., 2010). These suggested that together with the surface properties of the substrate, differentiation state of the cells as well as their carcinogenic nature effects deformability of the nucleus. Keeping in mind that the nucleus of the cancer cells deforms the most, our initial experiments were conducted with Saos-2 human osteosarcoma cell line (Figure 24c).

Preliminary testing of the effect of the micropillar array on Saos-2 nuclei revealed deformation of the nucleus. These deformations appeared to vary with the gap size of the micropatterns (Figure 24 c2-c3).

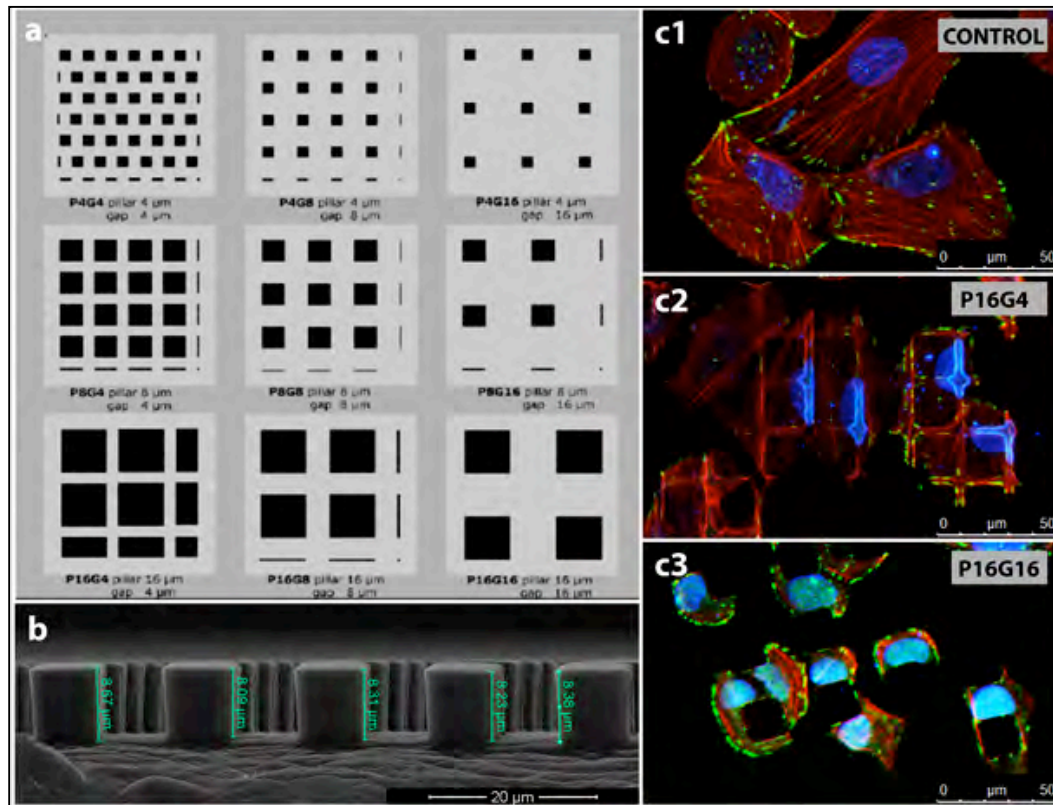


Figure 24: Design of the micropillar array chip and response of the Saos-2 cells to test the effect of pillar dimensions and spacing on deformations of the nucleus. (a) The array showing 9 different surfaces, (b) SEM of the P8G8 surface, and (c) deformations of nucleus of Saos-2 on P16G4 and P16G16. (a) Top row of the array consists of 4x4 μm pillars, spacing between the pillars are 4 μm, 8 μm, 16 μm, from left to right. Middle row consist of 8x8 μm pillars, and bottom row consists of 16x16 μm pillars. (b) Heights of the pillars were determined using SEM and average height was 8.3 μm (± 0.2). (c1) Saos2 osteosarcoma cells cultured on unpatterned, smooth surfaces show round-to-oval nuclei. Different levels on nuclear deformation were observed on (c2) P16G4 and (c3) P16G16, more distinct deformation on the narrower gap (G4), respectively. Stains: Blue-nucleus/anti-LMNA, Red- cytoskeleton/ Alexa-Phalloidin, Green- focal adhesions/anti-Paxillin).

3.4. Cell Viability on Micropatterned Substrates

Alamar Blue® cell viability assay was conducted to study the viability of the cells and the first day data is used as an indicator of cell adhesion. Cell numbers were calculated from the calibration curve (Appendix A) constructed using reduction in the UV absorbance of a dye and known cell numbers.

All the surfaces were made up from PLGA polymer. All the surfaces were found to be biocompatible. Cell proliferation rates were always $\geq 30\%$ of the TCPS.

Day 1 results were used as the indicator of cell adhesion (Figure 25). The lowest number of cells adhered to unpatterned PLGA control and highest number of cells adhered to P8G16. Statistical analysis of the day 1 Alamar Blue® analysis were significant. No significant difference was observed in the adherence of the cells on P4 surfaces (P4G4, P4G8, and P4G16). Adherence of the cells to P8G4 and P8G8 pair; P8G4 and P8G16 pair were significant and the latter ones had more cells.

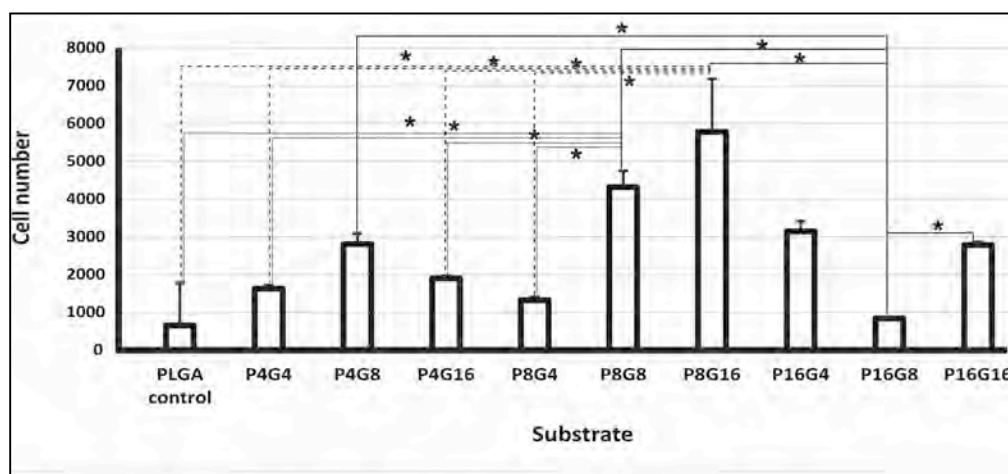


Figure 25: Day 1 Alamar Blue® results of 9 micropillar array surfaces and control, seeded with 5000 Saos-2 cells (One-way ANOVA, $n=3$, $p<0.005$. Tukey test for pairwise comparison, $*p<0.005$)

As the gap sizes gets smaller cell adhesion to the surface decreases (for P8 (P8G4, P8G8, and P8G16) and P16 (P16G8 and P16G16) surfaces). Even though there was statistical significance between pillar sizes for some surfaces, there is no recognizable pattern between pillar size and attachment to the surfaces. On the other, more cells adhered to micropatterned surfaces compared to smooth control. Lourenço et al., showed bovine articular chondrocytes (BAC) cultured on smooth and micro-rough poly(L-lactic acid) (PLLA) substrates with random surface patterns that, at day 1 less cells adhered on to the micro-rough substrates (Lourenço, 2011). These results are in consensus with the day 1 Alamar Blue® results of the Saos-2 cells.

14 days of culture on PLGA micropatterned surfaces revealed a similar trend for all the surfaces and unpatterned control (Figure 26), where proliferation rate accelerated after 7th day of culture. On P4G16, P8G16 and P16G8 surfaces proliferation rate of Saos-2 cells were faster than unpatterned control. Cell number determination using Alamar Blue® assay was found statistically significant (One-way ANOVA, $p < 0.005$).

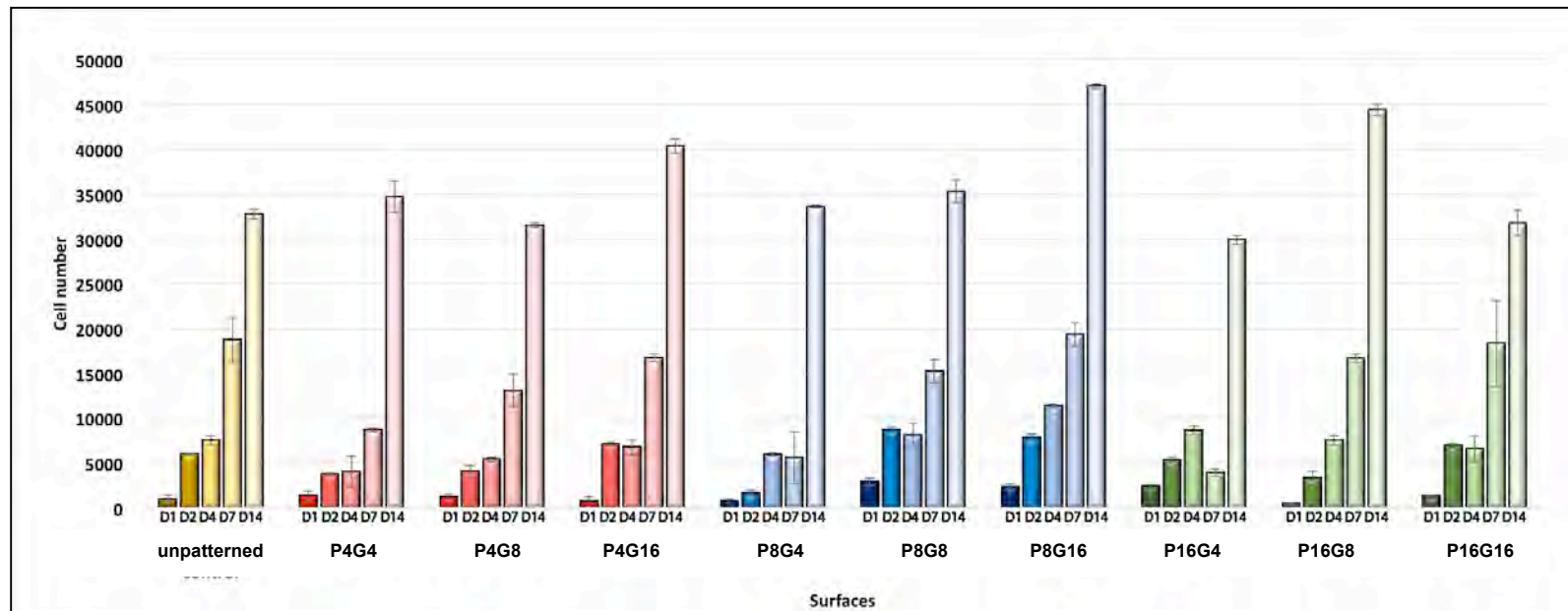


Figure 26: Alamar Blue® results of 9 micropillar array surfaces and control seeded with 5000 Saos-2 cells showing proliferation on different substrate topographies. One-way ANOVA analysis was performed and population means were found significantly different ($p < 0.005$). Cell numbers were calculated for days 1, 2, 4, 7 and 14.

3.5. Quantification of nuclear deformation on micropatterned substrates

The preliminary experiments indicated that the major factor in determining the extent of nuclear deformation was interpillar spacing. The 9 micropatterned surfaces (Figure 12, Table 5) we have designed differed in the spacing and size of pillars. To choose the surface that best amplifies the plasticity of the cancer cell nuclei, these nine surfaces were seeded with Saos-2 cells and cultured for 48 h. Based on the parameters for quantifying deformation described in the Materials and Methods section, it was found that pillar gap (*spacing*) was more effective than pillar size for inducing nuclear deformation. In addition, it was observed that the most significant nuclear deformations were caused by the P4G4 surface (Figure 27).

To identify the major determinant of nuclear deformation on these surfaces, the micrographs were analyzed and nuclei from each surface were examined for the shape descriptors Circle Variance and Rectangularity. In order to combine these two descriptors and make them a single parameter, a common dimensionality reduction technique, Principal Components Analysis (PCA), a common dimensionality reduction technique was used (Jolliffe, 2002). This method projects Circle Variance and Rectangularity onto a single axis that preserves the highest variance. Using only this dimension for statistical analysis and comparison of array surfaces, it was found that all the micropatterned surfaces had significantly different distributions compared to the control (Figure 27b). In the 4 μm spacing group, only P4G4 showed a different distribution than the other two. In the 8 μm spacing group only P16G8 showed a different distribution than the other two. In the 16 spacing μm group only P4G16 showed a different distribution than the other G16 surfaces. Among all the surfaces P4G4 had the most significant difference in population mean with the UC ($\mu_{x\text{ control}} = -0.15$, $\mu_{x\text{ P4G4}} = 0.084$).

In addition to interpillar spacing, dimensions of the pillars had an effect on the extent of deformation; the smaller the pillar size, the more extreme the deformations were. It must be kept in mind that these propositions are valid as long as the sizes

considered are in micron scale (comparable with the size of a single cell) (Karuri et al., 2004; Versaevel et al, 2012).

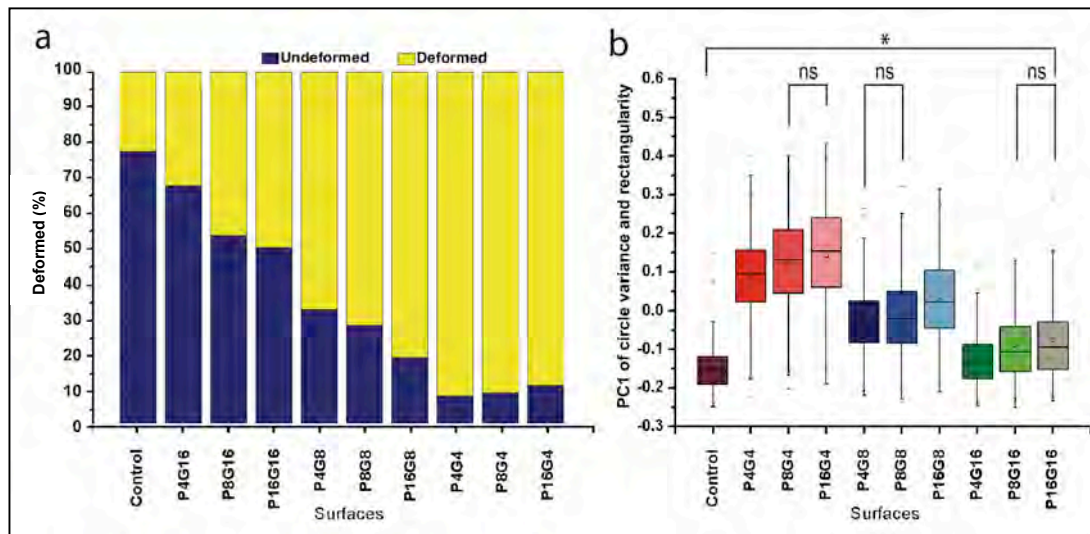


Figure 27: Deformation frequency and Principal Component 1 (PC1) of Saos2 cells on 10 surfaces tested. Two descriptors, circle variance and rectangularity were used to characterize the extent of deformation on the surfaces. (a) Deformed and undeformed nucleus frequency of Saos-2 cells on tested surfaces (yellow bar: deformed, blue bar: undeformed). (b) Saos-2 nucleus deformation analysis of Principal Component 1 (PC1) of the circle variance and rectangularity descriptors (* $p < 0.05$, ns: non-significant, Normality test: Kolmogorov-Smirnov, Welch's ANOVA with Games-Howell Test $p < 0.05$).

For further experimentation P4G4 surface was chosen. A 'Deformation Score' (DS) was devised for each population (Materials and Methods, Subsection 2.2.6.5). This DS combined how much the shape of a cell deviated from an ideal circle with whether it stayed more compact (e.g., like an ellipse) or obtained a bent shape (e.g., the shape of the letter "L"). This method was first tested with hypothetical (computer generated) shapes that resembled cell nuclei (Figure 27A1). R and CV values of the computer generated shapes were calculated and plotted onto the R-CV graph. 5 distinct regions were observed in the plot. These regions were named R1-5. DSs

were calculated for each population according to the distribution of cell nuclei into these 5 regions (Figure 28A2).

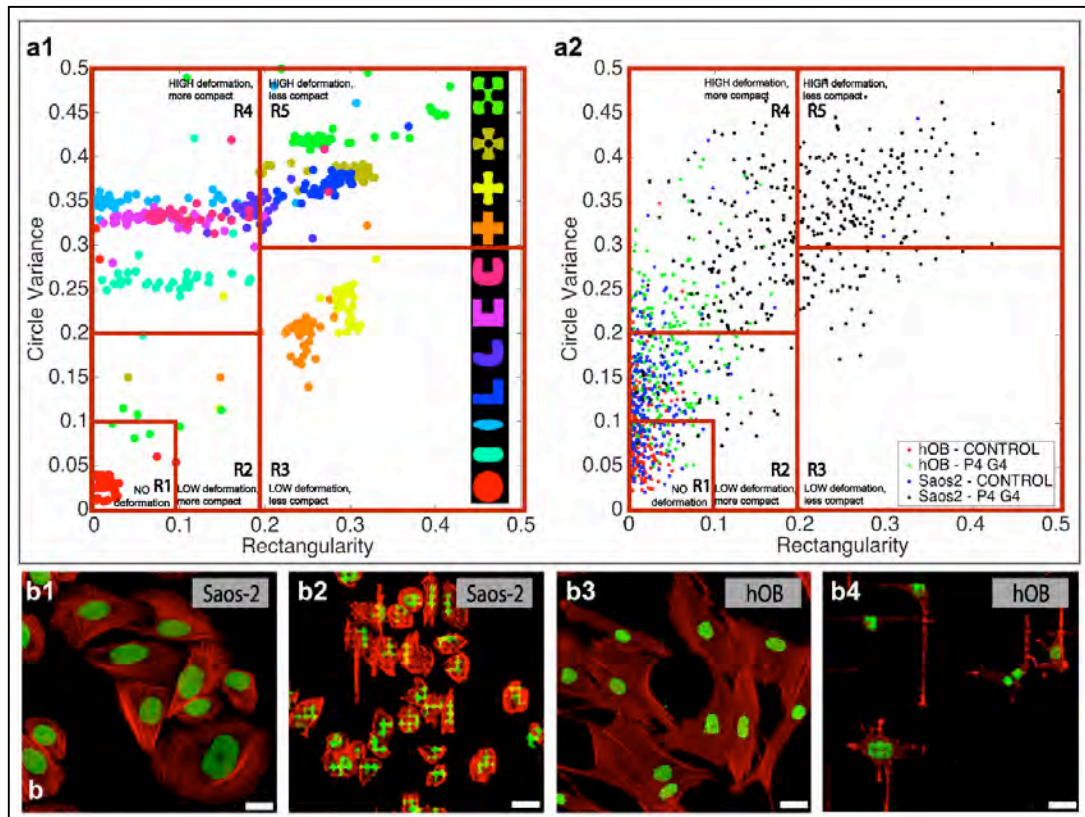


Figure 28: Circle variance (CV) and rectangularity (R) graphs of hypothetical nucleus deformations, Saos-2 and hOB cells. (a1) R and CV values were calculated from 11 hypothetical (artificially generated) templates mimicking nuclear deformations of actual cancer cells ($[R_1, CV_1 \leq 0.1, 0.1]$: no deformation, $[0.1, 0.1 < R_2, CV_2 \leq 0.2, 0.2]$: low deformation-more compact, $[0.2, 0 < R_3, CV_3 \leq 0.5, 0.3]$: low deformation-less compact, $[0, 0.3 < R_4, CV_4 \leq 0.2, 0.5]$: high deformation-more compact and $[0.2, 0.3 < R_5, CV_5 \leq 0.5, 0.5]$: high deformation-less compact). (a2) R and CV values were calculated from Saos-2 and hOB cells cultured on P4G4 and control PLGA surfaces. all. (b) Confocal micrographs of Saos-2 and hOB nuclei on control and P4G4.

Regions 1 and 2 were grouped as ‘non-deformed’ and Regions 3 to 5 as ‘deformed’. When these regions were defined and number of nuclei falling into each region was counted; it was found that 97% of the hOB cells on P4G4 were non-deformed while 70% of Saos-2 cells were deformed. On the control surface, almost all the cells were found to be undeformed (hOB 99%, Saos-2 96%).

From these results DS were calculated for each cell population. Deformation scores of hOB and Saos-2 cell populations were 1.04 and 1.22 on control, and 1.58 and 3.55 on the P4G4, respectively. The deformation score of Saos-2 on the P4G4 was at least twice as high as that of hOB. But their deformation scores on the control were similar. This shows that P4G4 surface can distinguish between Saos-2 and hOB. These results are also supported by the deformations observed in the CLSM micrographs (Fig.28b).

After establishing the regions and DS micropatterned substrates and quantification algorithm was tested with two non-cancerous (L929 cell line and hOB cells) and 3 cancer cell lines (Saos-2, MCF-7, and SH-SY5Y) (Figure 29). C.V vs R plots were obtained for all the tested cells. L929 and hOB (non-cancerous cell types tested) had the highest number of nuclei in R1-2, while SH-SY5Y, MCF7 and Saos-2 (cancerous cell lines) had the highest number of nuclei in R3-5. Their corresponding deformations scores were L929: 2.17, hOB: 2.54, Saos-2: 4.02, MCF-7: 3.90 and SH-SY5Y: 3.55 (Figure 29). On P4G4, hOB and L929 had $DS < 3$, while for MCF7, Saos-2, and SH-SY5Y, DS were greater than 3 (Fig.15b). In z-stack cross sections in the CLSM micrographs of L929 and hOB it was observed that nuclei were localized on top of the pillars (Figure 29c, d). For Saos-2, MCF7 and SH-SY5Y cells (Fig.29e-g) nuclear deformations were more distinct with Saos-2 and MCF7 presenting the most extreme deformations ($DS > 3.5$). These all showed that cancer cells from different tissue origins had different responses towards micropatterned substrates.

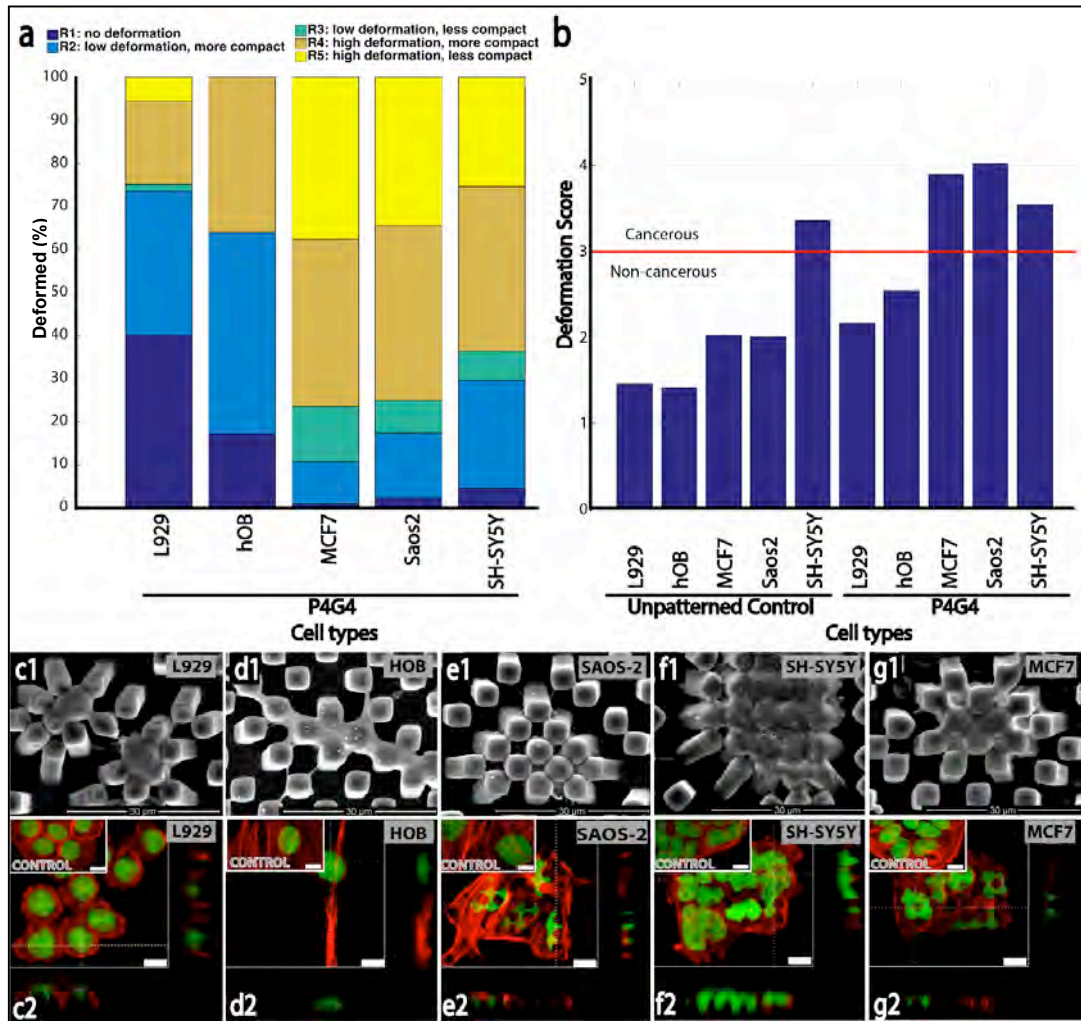


Figure 29: Quantification of deformation of two non-cancerous (hOB, L-929) and three cancer cell (Saos-2, MCF-7, SH-SY5Y) types on P4G4 surface. (a) Number of cell nuclei falling in R1-5 for each cell population. (b) Comparison of deformation scores of the cells tested on unpatterned control and P4G4 (DS: L929: 2.17, hOB: 2.54, Saos-2: 4.02, MCF-7: 3.90 and SH-SY5Y: 3.55). (c-g) 6 different cells: L-929, hOB, Saos-2, SH-SY5Y, and MCF7 were imaged. (c1-g1) SEM images (Scale bars: 30 μm. Stains: OsO₄). (c2-g2) CLSM images and z-stacks (Scale bars: 10 μm. Stains: Green: Nucleus/, DRAQ5, Red: actin cytoskeleton/ Alexa Fluor 532-Phalloidin).

3.6. Effect of Micropatterns on Cell Adhesion

Cell adhesion is the integral part of many cellular processes including proliferation and differentiation. Cell-material interactions play an important role in cell adhesion. In order to test the response of cells to substrates the polymers PLGA, PLLA and blends (PLGA:PLLA 100:0, 90:10, 80:20, 70:30, 50:50) and a range of micropatterned substrates (P8G4, P8G8, P8G16) were used. Two cells types, Saos-2 osteosarcoma and hOB (human osteoblast like) cells were employed.

3.6.1. Cell behavior on micropatterned substrates

Saos-2 cells on PLLA and PLGA micropatterned substrates (P8G16) were recorded with SEM and fluorescence microscopy to show the focal adhesions and anti-vinculin antibody was used (Figure 30). On unpatterned control PLLA (Figure 30 A1) and PLGA (A2) surfaces cells were spread and filopodia (yellow triangles) were visible. On PLGA surface more filopodia were observed because it provided a better attachment surface for cells (Figure 30 A2). On P8G16 PLLA surface (Figure 30 B1) a single osteosarcoma cell is seen stretched over the pillars (red arrows) and no filopodia was observed. On PLGA P8G16 surface (Figure 30 B2) a single osteosarcoma cell attached to at least three pillars with some cellular extensions reaching towards the ground (yellow triangle) along with extensive deformation and bending of the pillars were visible. On fluorescence microscope of the control PLGA surface focal adhesions (indicated by white chevron) are perpendicular to the cell body while on P8G16 surface focal adhesions follow the cell perimeter like a belt (Figure 30 A3, B3).

3.6.2. Patterned surfaces and focal adhesions

Saos2 cells were cultured on control, P4G16, P16G16 and P16G8 PLGA surfaces stained with anti-vinculin antibody (Figure 31). Distribution of focal adhesion of the cells changed with the surface topography. On a smooth surface, focal adhesions were localized at the periphery of the cell and were parallel to the actin fibers (Figure

31 A). On patterned surfaces (P4G16 and P8G16) focal adhesions were observed only at the edges of the cells neighboring the pillars and followed the periphery (Figure 31 B, C). On these surfaces the pillar areas were significantly smaller than the gap dimensions. When the pillar dimensions were larger than or similar to the spacing between them, the cells tended to occupy the gaps and focal adhesions were formed around the pillars(Figure 31 D, E).

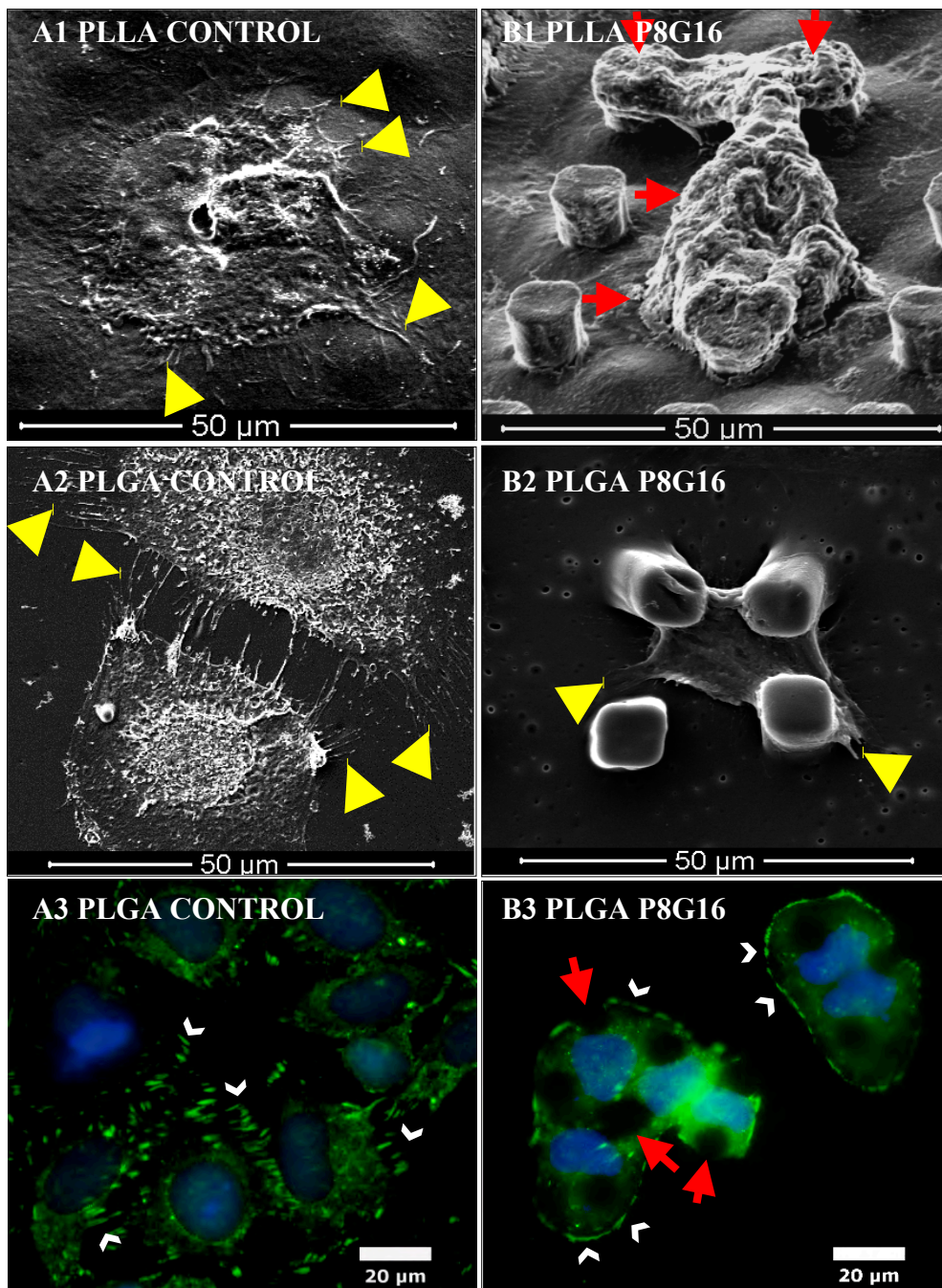


Figure 30: Saos-2 osteosarcoma cells cultured for 48 h on PLLA and PLGA surfaces. (A) Saos-2 cells cultured on unpatterned control surfaces (A1 PLLA, A2 PLGA, A3 PLGA). (B) Saos-2 cells cultured on P8G16 surfaces (B1 PLLA, B2 PLGA, B3 PLGA). (A1, A2, B1 B2) SEM images of the Saos-2 cells (OsO₄ staining, x4000). (A3, B3) Fluorescence micrographs of the Saos-2 cells (blue: DAPI, green: anti-vinculin, x63 objective)

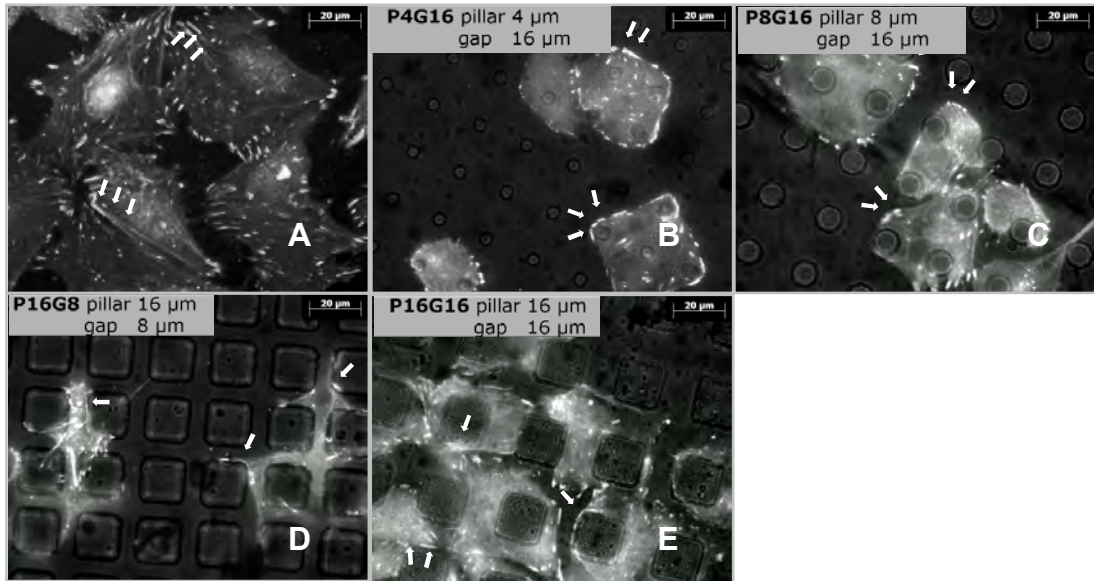


Figure 31: Overlaid images of focal adhesions stained with anti-vinculin antibody and actin cytoskeleton of Saos-2 cells cultured on PLGA (A) control, (B) P4G16, (C) P8G16, (D) P16G8, (E) P16G16 substrates. White arrows show focal adhesions observed from the vinculin signal (Scale bar: 20 μ m, x63 objective).

Saos-2 cells were cultured on control, P4G4, P16G4 and P16G16 surface and anti-paxillin antibody was used to stain the focal adhesions (Figure 32). It was observed that vinculin and paxillin distributions were similar. On the control surface, focal adhesions points were observed to align with the cell periphery (Figure 32 A). Focal adhesions were spaced with equidistance and all around the cell border (yellow arrows). On the P4G4 surface, where the pillars were very small compared to the spacing in between them, distribution of focal adhesions were similar to the control (Figure 32 B). Unlike the control, the distribution of focal adhesions were discontinuous (yellow arrows) on this surface. On P16G4 surface, where pillars are much large than the spacing, focal adhesions were observed to be localized at the edges of the pillars (yellow arrows) (Figure 32 C). On P16G16 surface, where both pillars and interpillar spacing are much larger than the size of the cell, focal adhesions were observed only at the borders between a pillar and a cell (Figure 32 D).

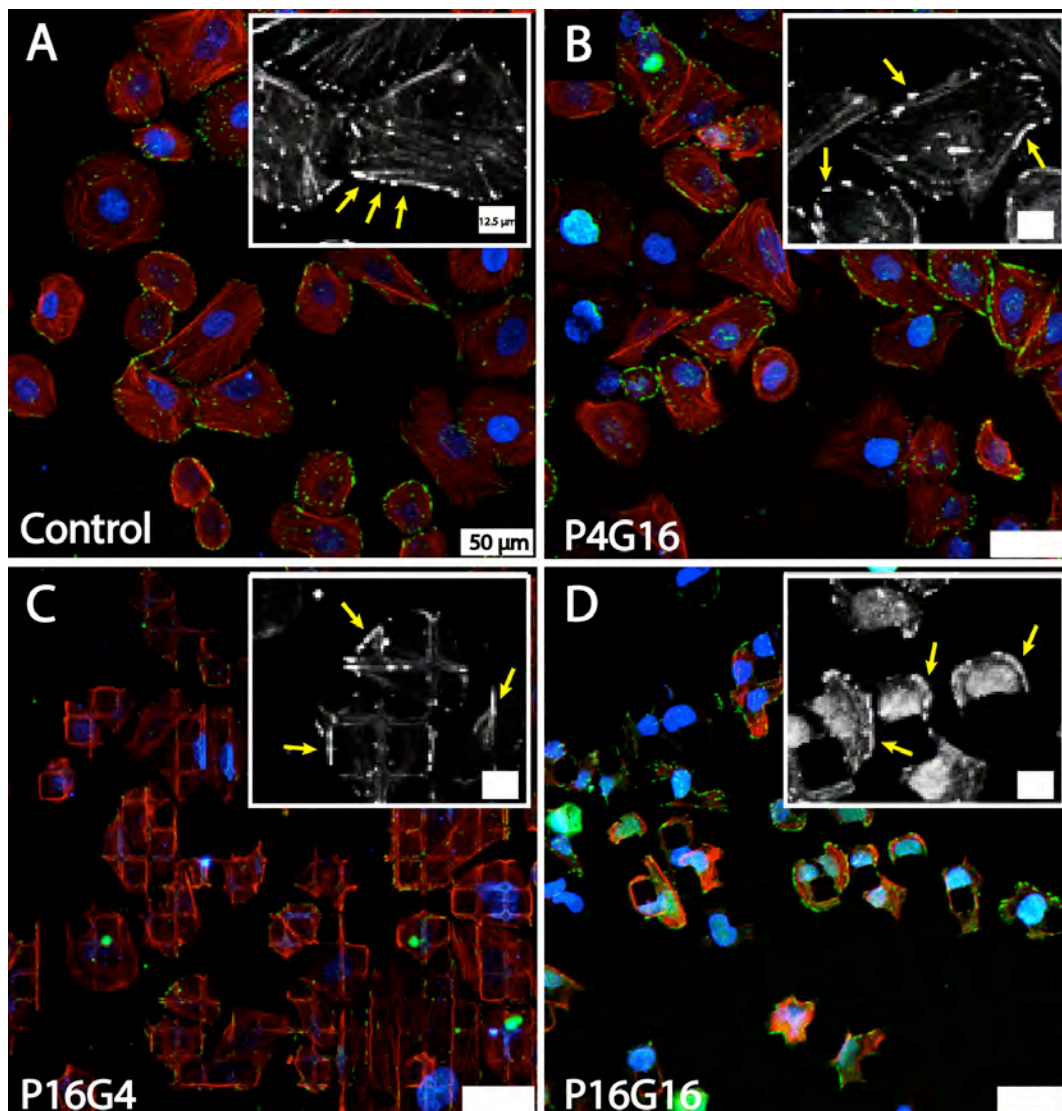


Figure 32: CLSM micrographs of Saos-2 osteosarcoma cells cultured on PLGA surfaces for 48 h, fixed and imaged (A) control, (B) P4G16, (C) P16G4, (D) P16G16 surfaces. (x20 objective. Scale bar: 50 μm, red: actin, blue: nucleus, green: paxillin. Inserts: x40 objective, scale bar: 12.5 μm)

3.6.3. Cell Type and Surface Interaction

The Saos-2 and hOB cells were studied on P8G8 and P8G16 PLGA surfaces using SEM. (Figure 33). On all the surfaces hOB cells maintained their spindle like geometry with cell nuclei prominent at the middle portion of the cells (Figure 33 A, C). hOB cells attached to the pillars at the very bottom through their cellular protrusions (filopodia). On the other hand, Saos-2 cells had bulky, rounded cell bodies and appeared to be draped onto the pillars (Figure 33 B, D). This localization of osteosarcoma cells on the pillars enabled them to deform and bend pillars more distinctly than hOB cells.

As the pillar spacing got smaller, osteoblast cells aligned with each other more (Figure 33 C). Saos-2 cells (Figure 33 B, D) preserved their polygonal shape and did not elongate or align.

3.6.4. Calculations of Pillar Bending Force

After observing bending of the pillars under the tug of the cells, a method was sought to calculate the cellular force. This would allow to relate material stiffness and the extend of cell-material interaction to cellular force generated. Bending of a micro pillar was modeled according to Timoshenko Beam Theory (considering bending and shear deformations) (Timoshenko, 1921). This model takes into consideration the Young's modulus of the material (the beam), the beam dimensions (x , y , h) and the deflection of the tip in x (Δ_x) and y (Δ_y) direction. In the model, the beam is fixed to a rigid support at one end, (just like the pillars on the substrate in our case) while the tip is free. Four different load application cases were used. Case a: point load at the free end of the beam, b: uniformly distributed load along the length of the beam, c: distributed load decreasing toward the tip of the beam, and d: distributed load increasing toward the tip of the beam (Blodgett, 1966) (Figure 34).

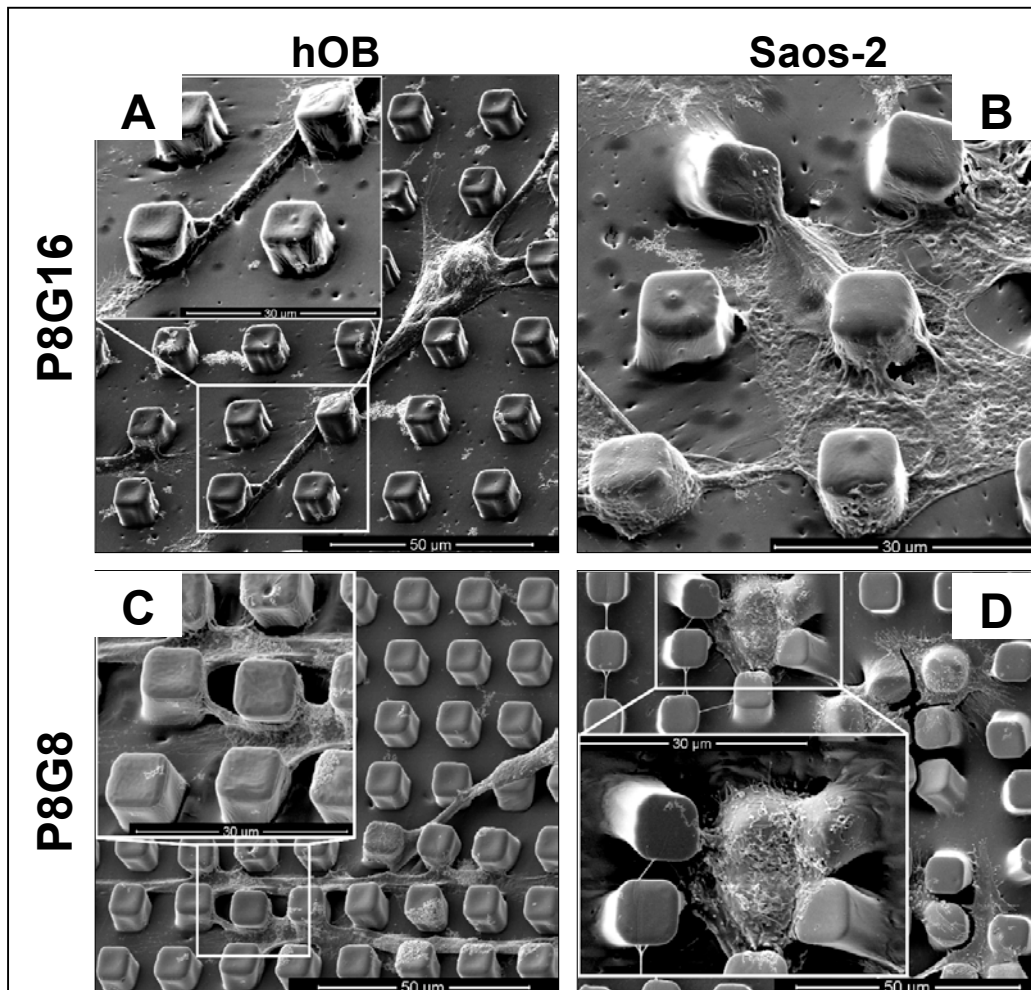


Figure 33: SEM micrographs of hOB and Saos-2 cultured on P8G16, and P8G8 PLGA micropatterned surfaces. (A) hOB cells on P8G16, (B) Saos-2 cells on P8G16, (C) hOB cells on P8G8, and (D) Saos-2 cells on P8G8 (Scale bar: 50 μm, x4000, inserts: scale bar: 30 μm, x8000)

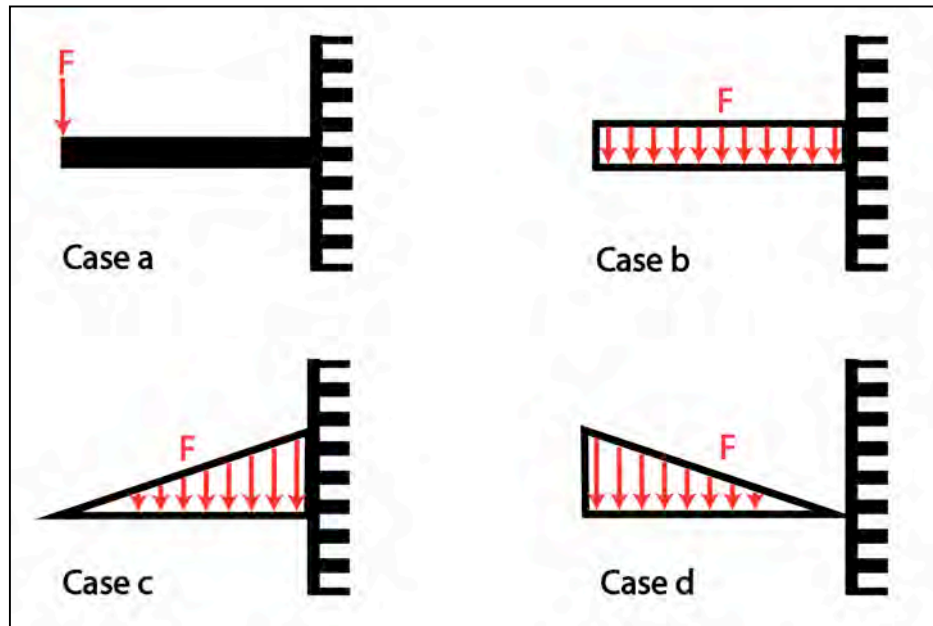


Figure 34: Calculation of pillar bending forces was modeled according to beam bending equations. Force can be applied to the beam in four different ways. Case a: to the free end of the beam, b: to whole length of the shaft of the beam uniformly, c: to whole length of the shaft of the beam, decreasing towards the free end, and d: to whole length of the shaft of the beam, increasing towards the free end (Adapted from Blodgett, 1966).

Since Saos-2 cells prefer to attach to pillar tops case d is chosen for the model that best reflects the mechanism of pillar bending by Saos-2 cells. Four versions of the beam-bending model were applied to a single bent pillar (Figure 35, pillar 1). Forces required to create the same amount of deflection were calculated for each loading case. Our calculations revealed that, the order of the force required to create the same amount of deflection was $c > b > d > a$ (Figure 36). Case a is a simplistic model, which assumes a point force is applied to the pillar tip by the cell. From the SEM images it is clear that this is not the case, and cells attach to a surface rather than a point (Figure 33). Nevertheless, this model was included as a simple reference and for comparison.

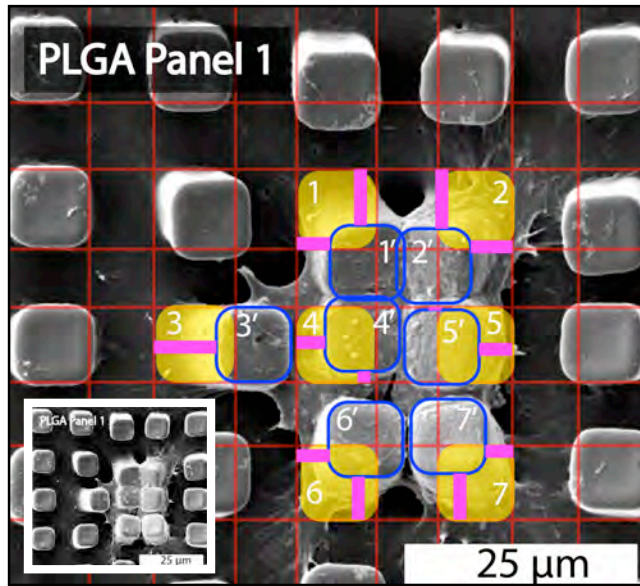


Figure 35: Bending of pillars were calculated from the deflection in x and y axis (Δ_x, Δ_y) of the SEM images of the pillars. Yellow boxes indicate the original position of the pillars and blue borders indicate the deflected position. Red lines show amount of deformation in x and y axes. (Insert: original image, scale bars: 25 μm)

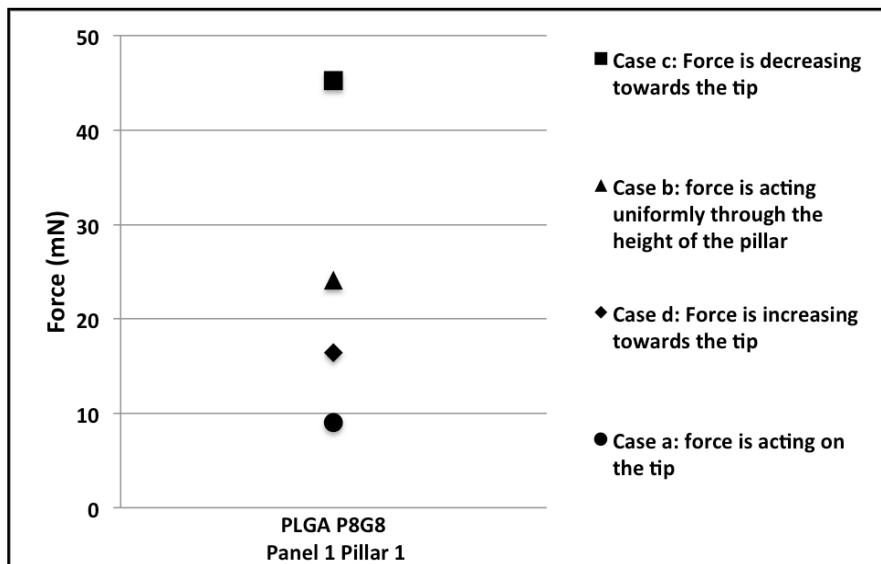


Figure 36: Bending force on PLGA Pillar 1 (Panel 1). Data was calculated by using the 4 versions of the beam bending model ($\Delta_x=0.0084$ mm, $E=7.17 \times 10^8$ Pa, $\nu=0.45$, $G=2.422 \times 10^8$ Pa).

Case b represents the optimal situation, in which the cell attaches to the entire length of the pillar and applies a uniform force. This also is not the case, because Saos-2 cells prefer to attach to pillar tops (Figure 33). In the other two cases forces are not uniformly distributed throughout the pillar. Case c assumes that force applied decreases towards the tip and case d assumes force increases towards the tip. Pillar bending was most commonly observed with Saos-2 samples (Figure 33), and pillar bending calculations will be performed on micrographs of Saos-2 samples.

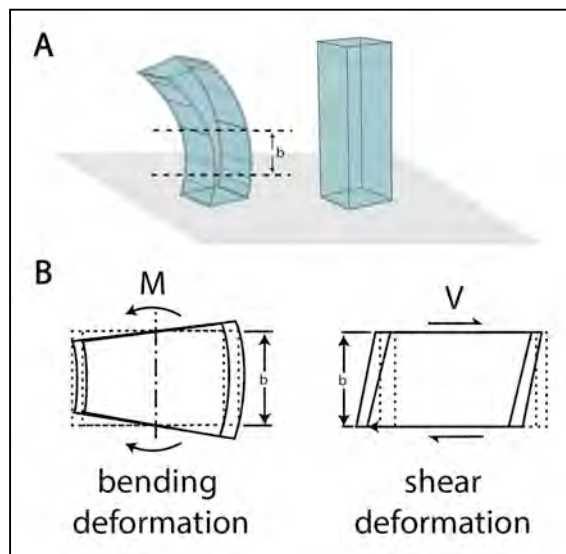


Figure 37: Schematic representation of a bending pillar. (A) A small aspect ratio pillar bends with two modes of deformation taking place. (B) Cross section of the pillar at ‘b’ region. During bending deformation, the length of the side of the pillar towards bending direction is decreased while the side against bending direction is expanded. In the case of shear deformation, the change of shape resulting from a move (slide) perpendicular to the deformation direction is observed.

Further explanation regarding the effects of shear deformations is required to prove the validity of shear deformation in this model. Shear forces cause sliding type of deformations in solid objects (Figure 37). These sliding effects are insignificant in tall and slender objects (large aspect ratio) due to the fact that the bending deformations are much larger than the shear deformations. This is because the

bending deformations are proportional to the cube of the length of the pillar, whereas the shear deformations are linearly proportional to the height of the pillar (Material methods section, derived from Timoshenko Beam Theory) (Timoshenko, 1921). For shorter objects like the pillars, where the aspect ratio is close to one, the sliding effects can compose up to 30% of the total deformation.

Shear deformations were included in the calculations of the two cases (Case a and d) (Figure 38). Bending deformations calculated with shear taken into consideration were lower than without shear because shear deformations could constitute ca 30% of the total deformation. It was concluded that calculating the force from the formula where force is applied to the whole length of the shaft of the beam, increasing towards the free end while taking shear bending into consideration will represent our pillar bending more accurately (case d, w/ shear deflection).

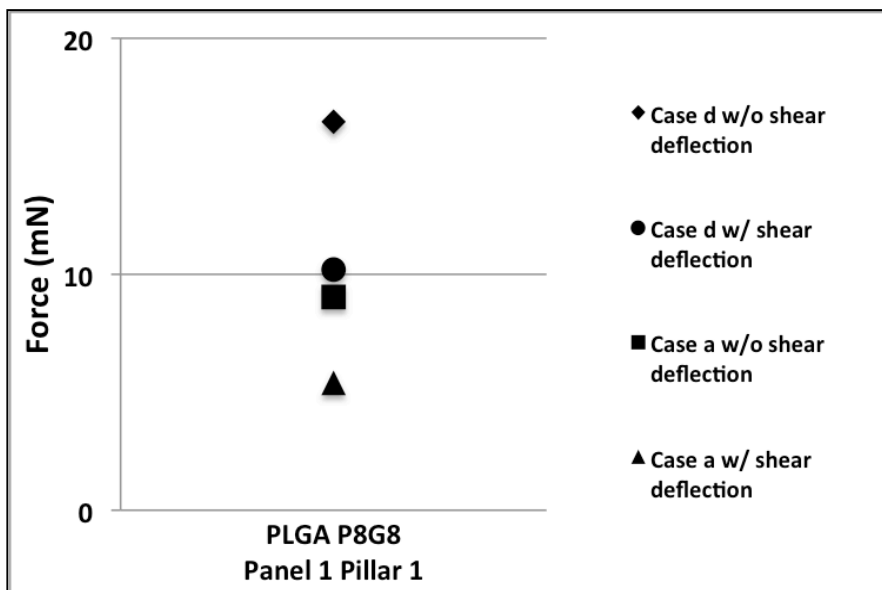


Figure 38: Bending force of the Pillar 1 of PLGA Panel 1 calculated according to Case a (to the free end of the beam), and Case d (to whole length of the shaft of the beam, increasing towards the free end) with and without taking shear deflection into consideration. ($\Delta_x=0.0084$ mm, $E=7.17 \times 10^8$ Pa, $\nu=0.45$, $G=2.42 \times 10^8$ Pa).

3.6.4.1 Saos-2 cells pillar bending forces on PLGA micropatterned surfaces

Bending of polymeric pillars on a substrate by the cells seeded depends on mechanical properties, pillar dimension and pillar spacing which determines the number of pillars per unit area. In order to study the effect of pillar density (which is a result of the differences in the width of the gaps between the pillars while pillar areas are the same) on extent of pillar bending 3 surfaces were chosen: P8G4, P8G8 and P8G16. Since the pillar size is kept the same while changing the interpillar spacing, number of pillars per unit area (pillar density) decreases in the following order: P8G4>P8G8>P8G16. SEM images were used to measure pillar displacements (Figure 39 PLGA P8G4, Figure 40 PLGA P8G8, and Figure 41 PLGA P8G16). ImageJ software was used for the measurements and then pillar bending equation (described in Materials and Methods, Calculation of Pillar Bending) was used to calculate forces that led to bending. Saos-2 cells bent the pillars on all 3 surfaces (Figure 42). Pillar displacement was smallest in P8G4, and in G8 and G16 more prominent (Figure 42A). Since pillar height was ca. 8 μm , on P8G4 surface, the pillars were too close to deform as much as they could. On the other hand, an interpillar spacing $\geq 8 \mu\text{m}$ (G8, G16) led to the highest displacement because the entire height of a pillar could be at most equal to the interpillar distances on those surfaces (Figure 42 A). Forces calculated from pillar displacements reflect a trend similar to that of pillars (Figure 42 B). P8G4 had the smallest force, while $\geq 8 \mu\text{m}$ interpillar spacing (G8, G16) had similar bending force to one another and were higher than G4 (Figure 42 B).

Our results were in good agreement with the few literature data available. Han et al. showed that cellular traction forces that bend micropillars were directly related to the density of the pillars underneath a cell (Han et al, 2012). They also postulated that by increasing the pillar density, arrays effective shear modulus was increased, and further stiffness was added to the materials properties.

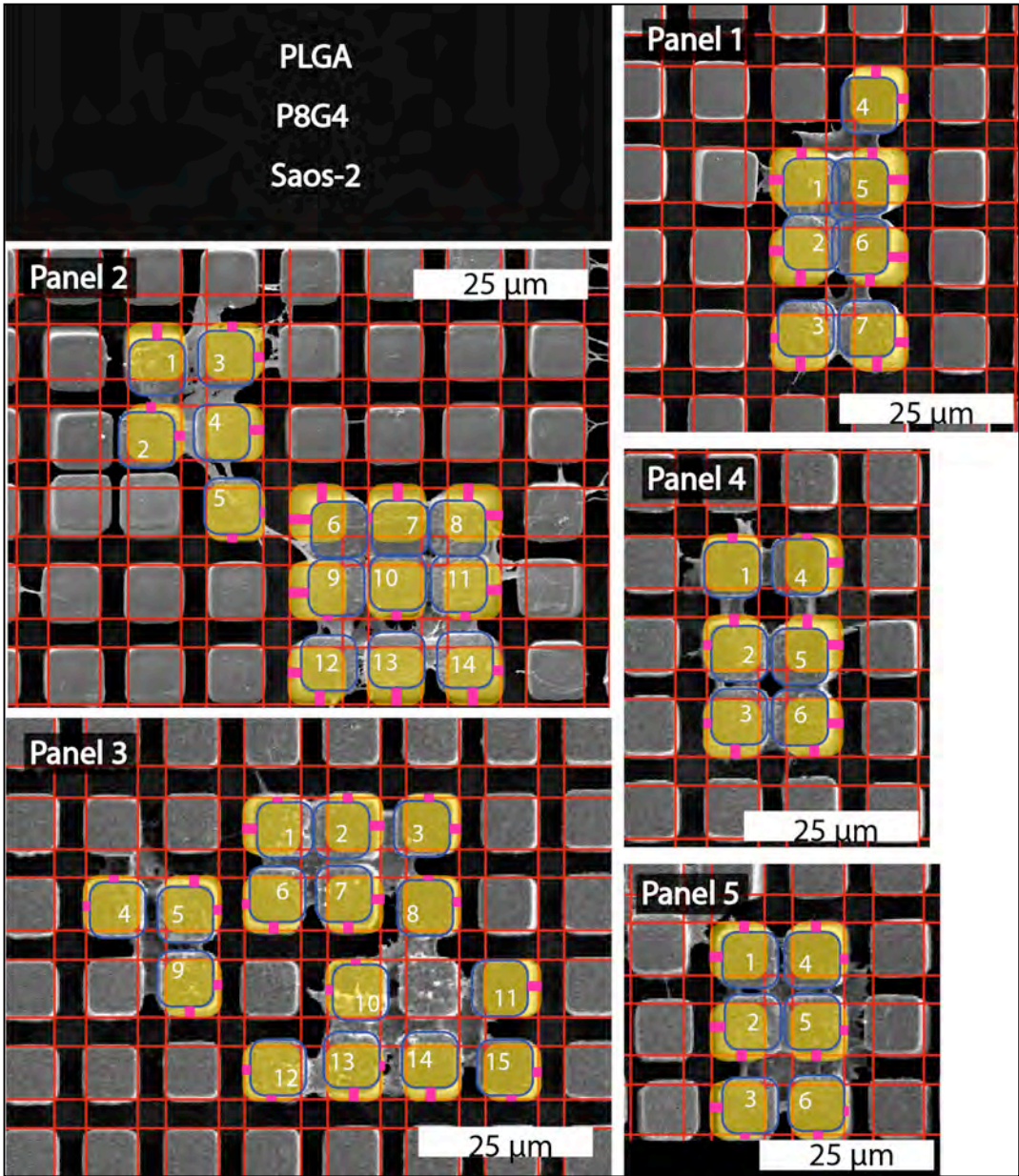


Figure 39: SEM micrographs of Saos-2 cells cultured on P8G4 PLGA substrate for 48 h. Deflection of pillars in x and y axis were calculated from 5 panels (yellow box: original pillar location, blue box: deflected pillar location, scale bar 25 μm, x2000).

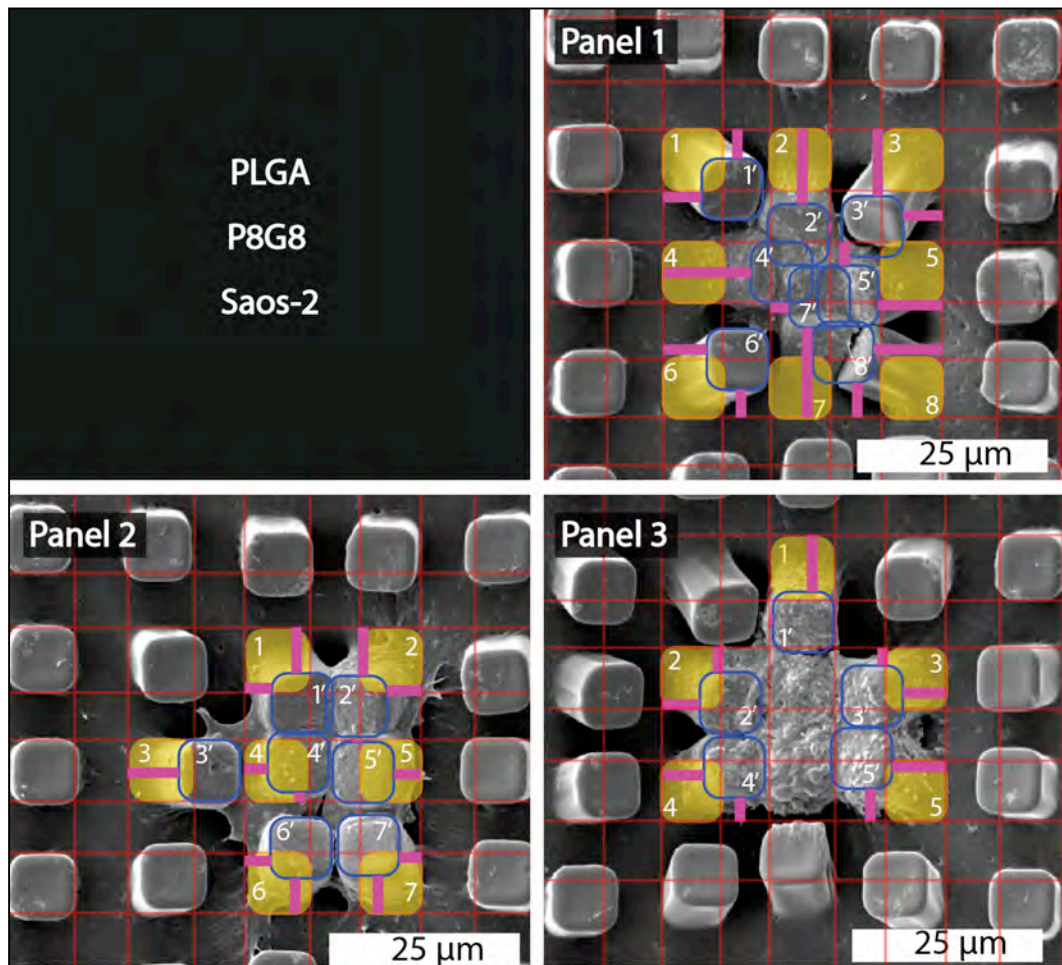


Figure 40: SEM micrographs of Saos-2 cells cultured on P8G8 PLGA substrate for 48 h. Deflection of pillars in x and y axis were calculated from 5 panels (3 panels are presented here)(yellow box: original location, blue box: displaced pillar location, scale bar 25 μm , x2000).

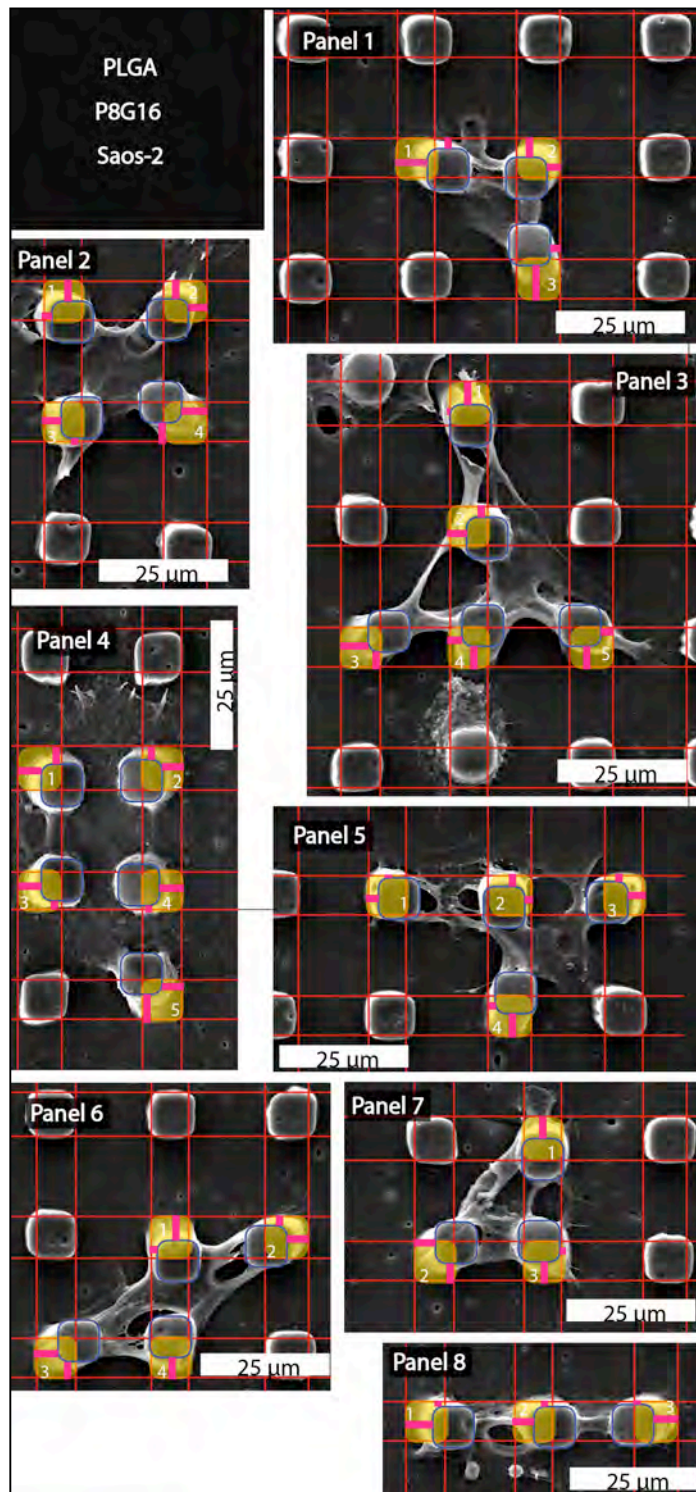


Figure 41: SEM micrographs of Saos-2 cells cultured on P8G16 PLGA substrate for 48 h. Deflection of pillars in x and y axis were calculated from 8 panels (yellow box: original location, blue box: displaced pillar location, scale bar 25 μm , x2000).

Beam bending theory was used to calculate forces exerted by the cells on microposts on arrays (Sniadecki et al., 2007; Schoen et al., 2010; Han et al., 2012). Novelty of the present study lies in the fact that while references used soft and cylindrical micropatternes (PDMS 1-3 MPa, Schoen et al., 2010, PDMS 2.5 MPa, Sniadecki et al., 2007; PDMS 2.5 MPa, Han et al., 2012) considerably stiffer substrates (PLGA 0.72 GPa, PLLA 1.64 GPa and PLGA:PLLA 80:20 0.06 GPa) were used in the present study. Even the softest substrate (PLGA:PLLA 80:20) was ≥ 50 times stiffer than the substrates reported. Since the current substrates were stiffer, bending forces calculated were also considerably high (For example Saos-2 cells on PLGA:PLLA 0.222 mN). Sniadecki et al. measured forces in the range of 1-100 nN (Sniadecki et al., 2007), Schoen et al. measured up to 60 nN with 3T3 fibroblasts (Schoen et al., 2010) and Han et al. measured up to 10 nN per post and 500 nN per cell (Han et al., 2012) whereas the forces calculated in this study were in the range of μN .

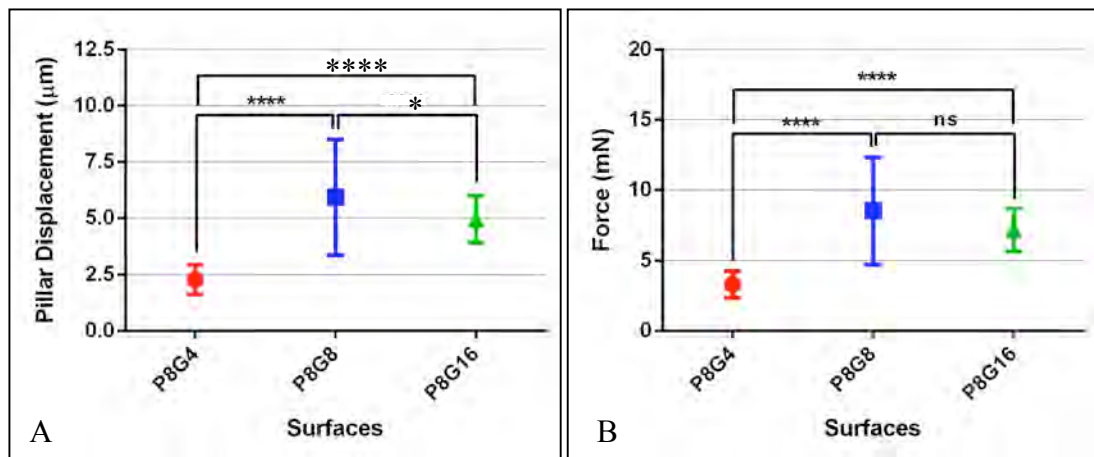


Figure 42: Pillar displacements and forces calculated using SEM micrographs of Saos-2 cells cultured on micropatterned P8G4, P8G8, P8G16 substrates. (A) Pillar displacements were measured from SEM micrographs using NIH ImageJ software. The sum vectors of Δ_x and Δ_y for each pillar were calculated. (B) Forces corresponding to sum vectors for each pillar was calculated according to case d while taking shear deflections into consideration. (One-way ANOVA, $p < 0.001$, * $p < 0.05$, ** $p < 0.001$, *** $p < 0.005$, **** $p < 0.001$, $n \geq 30$).

3.6.4.2 Bending of PLGA P8G8 pillars by Saos-2 vs hOB cells

In order to compare the strength of the tug on pillars by two cells originating from bone tissue, Saos-2 osteosarcoma cells and hOB human osteoblast like cells were used. PLGA P8G8 surfaces were seeded with Saos-2 or hOB cells (Figures 40 and 43 respectively) and pillar displacements were measured as described above. hOB cells led to smaller pillar displacements compared to Saos-2 cells (Figure 44 A). Consequently, forces calculated were smaller in the hOB group (Figure 44 B). SEM images were studied to compare number of pillar each cell interacted (Figure 45 A). Saos-2 cells interacted with a lower number of pillars. Saos-2 is known to have a polygonal shape (Figure 32 A) while hOB cells are elongated and span more pillars throughout their cellular processes (Figures 33 A, C).

Average force per cell was calculated by adding up the forces for all the pillars that each cell interacted (Figure 45 B). Surprisingly, both hOB and Saos-2 cells had a similar average force per cell. This indicates that even though Saos-2 cells interact with a lower number of pillars, exerted more force per pillar than hOB cells.

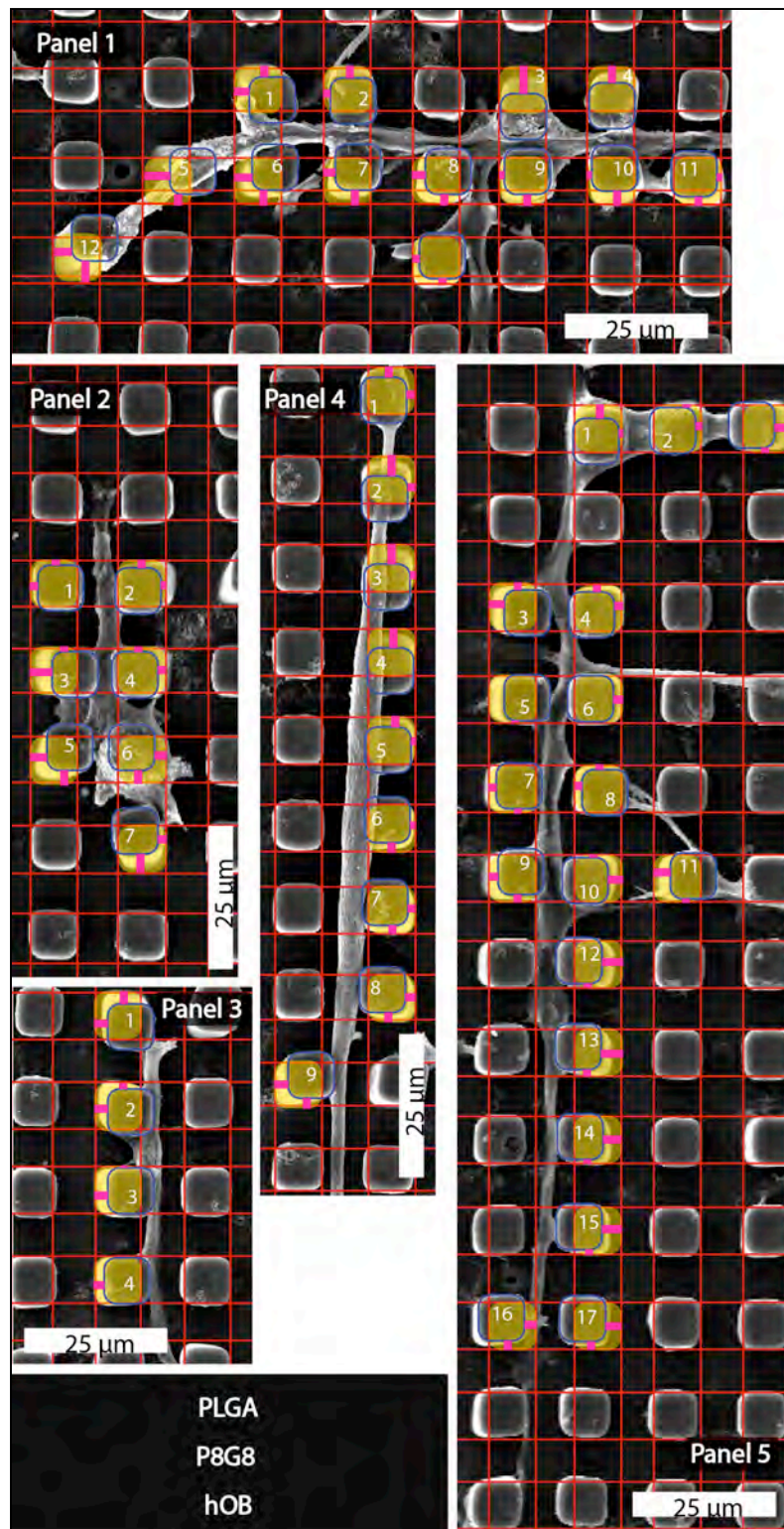


Figure 43: SEM micrographs of hOB cells cultured on P8G8 PLGA substrate for 48 h. Deflection of pillars in x and y axis were calculated from 5 panels (yellow box: original location, blue box: displaced pillar location, scale bar 25 μm, x2000).

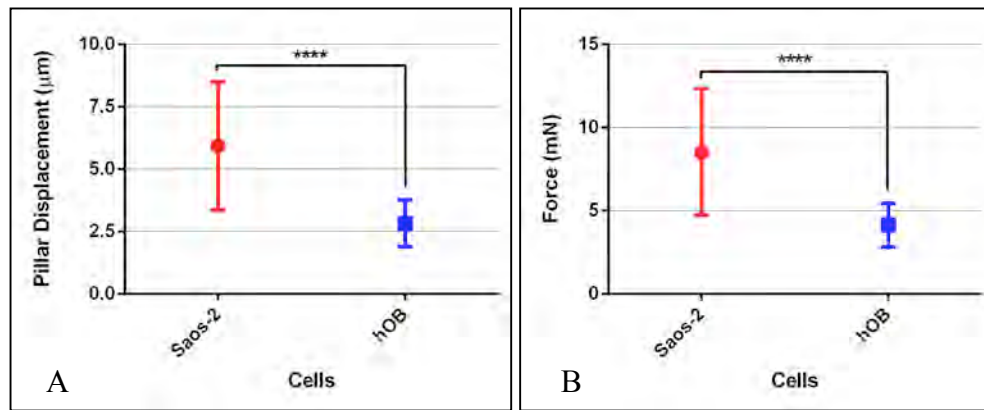


Figure 44: Pillar displacements and forces calculated from SEM micrographs of Saos-2 and hOB cells cultured on P8G8 micropatterned substrates. (A) Pillar displacements were measured from SEM micrographs using NIH ImageJ software. The sum vectors of Δ_x and Δ_y for each pillar were calculated. (B) Forces corresponding to sum vectors for each pillar was calculated according to case d while taking shear deflections into consideration. (unpaired t-test, $p < 0.001$, * $p < 0.05$, ** $p < 0.001$, *** $p < 0.005$, **** $p < 0.001$, $n \geq 30$)

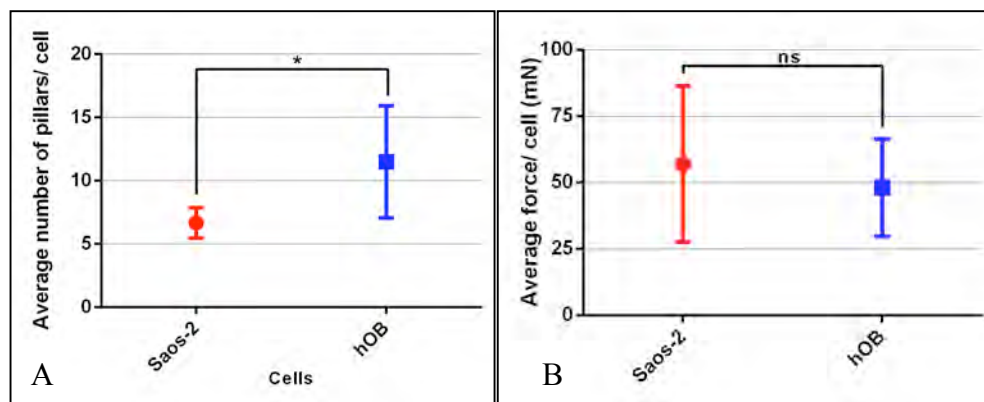


Figure 45: Average number of pillars each cell interacted and average force per cell calculated from these measurements. (A) Average number of pillars was calculated from SEM images. (B) Average force for each cell was calculated from addition of forces of each pillar a cell interacts (unpaired t-test, $p < 0.001$, * $p < 0.05$, ** $p < 0.001$, *** $p < 0.005$, **** $p < 0.001$, $n \geq 3$).

3.6.4.3 Saos-2 cells pillar bending forces on P8G4 PLGA vs PLLA vs PLGA:PLLA 80:20

Finally, effect of substrate stiffness on pillar binding was studied. Saos-2 cells were cultured on PLGA:PLLA 100:0, 0:100, 80:20 P8G4 substrates (Figures 39, 46 and 48 respectively). Pillar displacement was highest on PLGA and smallest on PLLA surface (Figure 48 A). Bending forces on the other hand was similar on PLGA and PLLA (Figure 48 B). This result correlates with the Young moduli of the polymers (PLGA 0.72 GPa and PLLA 1.64 GPa). On the other hand PLGA:PLLA 80:20 was considerably softer, $E=0.06$ GPa. Average force on PLGA:PLLA 80:20 was 0.22 mN, 15 times smaller than PLGA or PLLA (3.2 and 3.6 mN respectively).

There results were comparable with the literature. Sniadecki et al. used PDMS with $E=2.5$ MPa (40 times softer than PLGA:PLLA 80:20) with pillar dimensions $2\ \mu\text{m}$ and height $8\ \mu\text{m}$ and measured 100 nN force (2200 times smaller than PLGA:PLLA 80:20) (Sniadecki et al., 2007) since they had 4 times smaller pillars. When their values are used with the beam bending formulation of the current study ($D=2\ \mu\text{m}$, $h=8\ \mu\text{m}$, $E=2.5$ MPa), Case c with shear deformation formula yields 0.00018 mN (180 nM) for Sniadecki et al. study.

Considering that the cell type and pillar geometry was different these results seem to correlate with our force calculations.

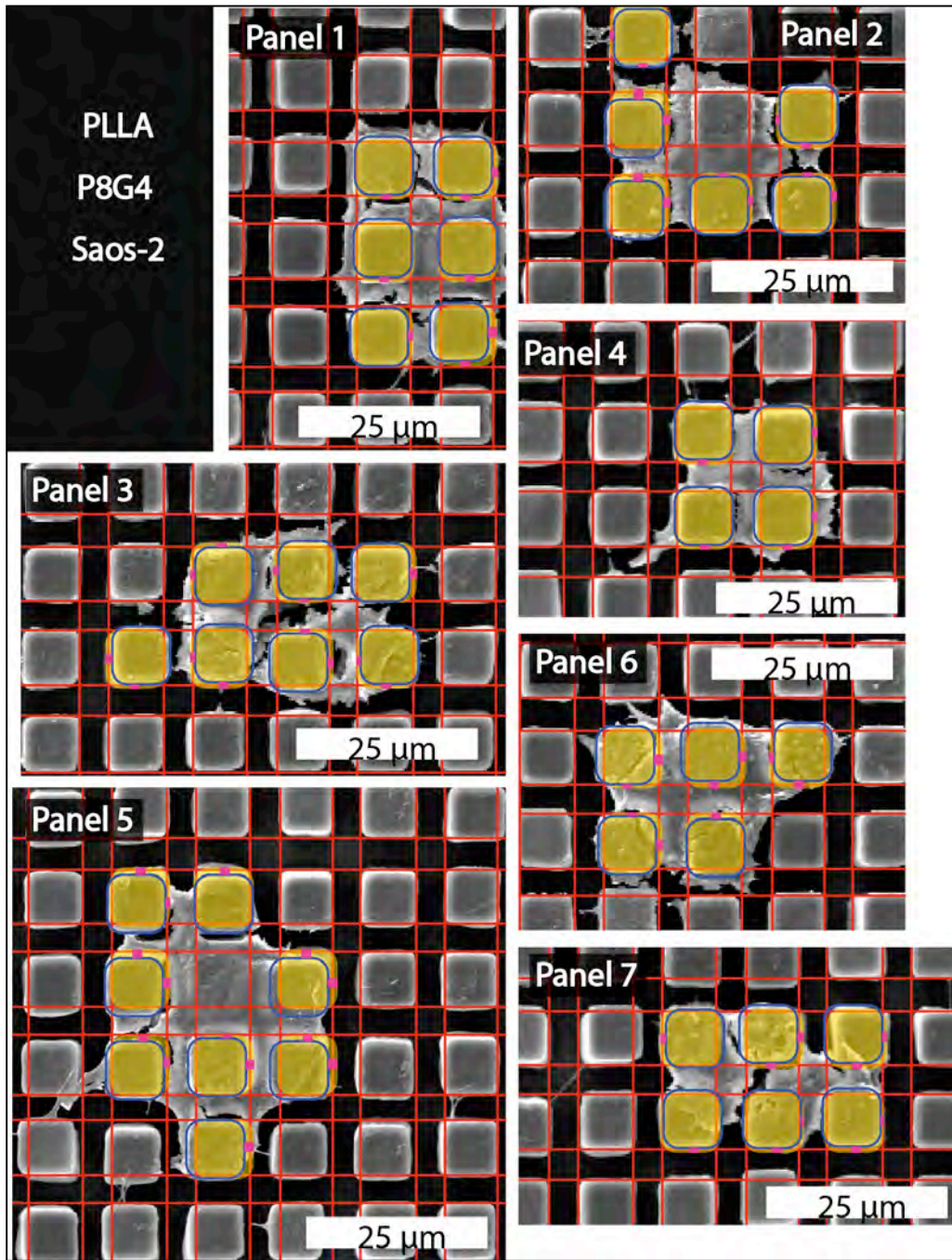


Figure 46: SEM micrographs of Saos-2 cells cultured on P8G4 PLLA substrate for 48 h. Deflection of pillars in x and y axis were calculated from 8 panels (yellow box: original location, blue box: displaced pillar location, scale bar 25 μm , x2000).

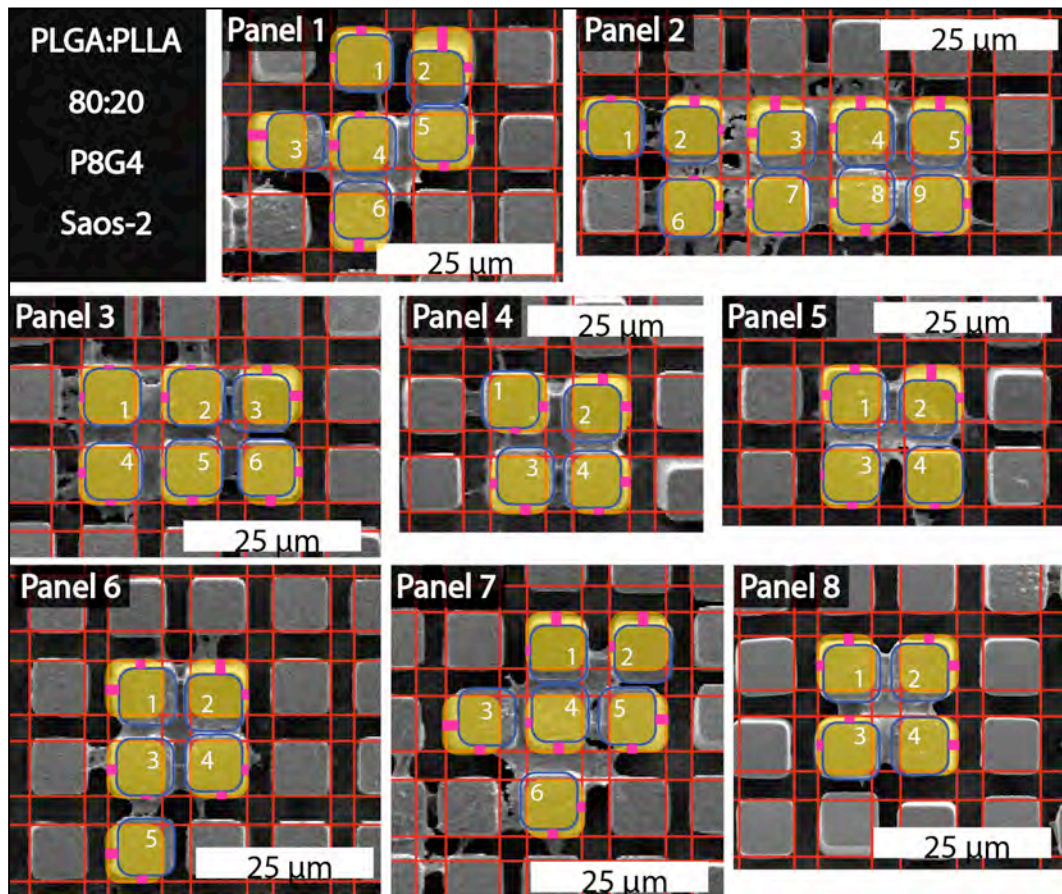


Figure 47: SEM micrographs of Saos-2 cells cultured on P8G4 PLGA:PLLA 80:20 substrate for 48 h. Deflection of pillars in x and y axis were calculated from 8 panels (yellow box: original location, blue box: displaced pillar location, scale bar 25 μm, x2000).

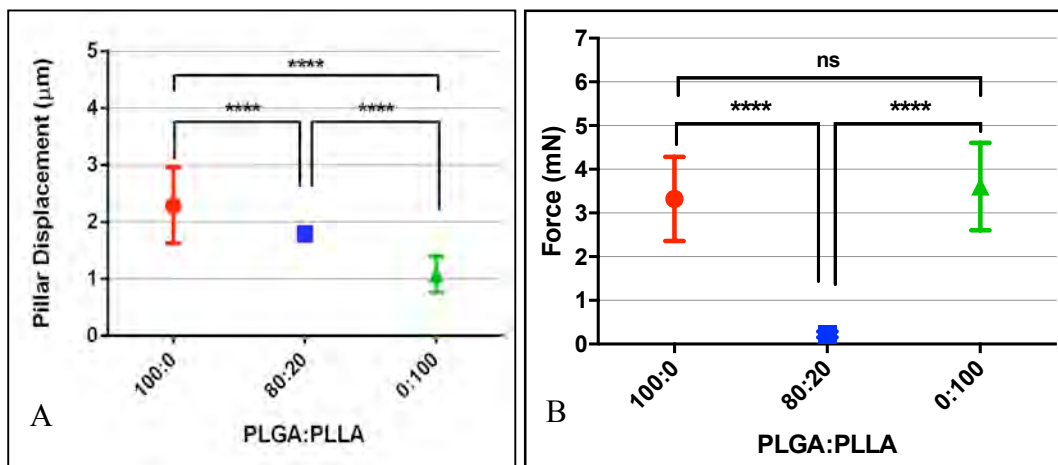


Figure 48: Pillar displacements and forces calculated from SEM micrographs of Saos-2 cells cultured on P8G4 PLGA:PLLA 100:0, 0:100 and 80:20 micropatterned substrates. (A) Pillar displacements were measured from SEM micrographs using NIH ImageJ software. The sum vectors of Δ_x and Δ_y for each pillar were calculated. (B) Forces corresponding to sum vectors for each pillar was calculated according to case d while taking shear deflections into consideration. (One-way ANOVA, $p < 0.001$, * $p < 0.05$, ** $p < 0.001$, *** $p < 0.005$, **** $p < 0.001$, $n \geq 30$)

3.6.5. PCR Array of Focal Adhesion Related Genes of hOB and Saos2 on Micropatterned Substrates

Saos-2 and hOB cells were cultured on micropatterned (P8G4 and P8G8) and control PLLA and PLGA substrates and a PCR array was performed which included 84 key genes in focal adhesion pathway. Genes were normalized to housekeeping gene (GAPDH). Fold regulations were calculated by comparing micropatterned and unpatterned substrates. Fold regulation of all genes for P8G4 PLGA and PLLA surfaces and with Saos-2 and hOB cells were plotted (Figure 49, Appendix A1-4 individually). The results show that Saos-2 cells on PLLA has many upregulated FA genes while on PLGA most were unchanged. hOB cells on PLLA and PLGA

substrates showed significant upregulation. Saos-2 and hOB cells cultured on PLLA micropatterned substrates had higher upregulation of FA genes compared to PLGA substrate (Figure 49 Appendix D1-4).

FA genes of hOB and Saos-2 cells cultured on micropatterned PLGA substrates showed upregulation and this increase was higher with hOB cells (Figure 49, Appendix D1 and D4). On the other hand, the Saos-2 cells cultured on PLLA showed a higher number of upregulated genes than on PLGA substrates (Figure 49, Appendix D1-2). While, hOB on PLGA and PLLA had similar number of genes upregulated but the fold regulations were smaller (Figure 49).

PLLA (stiffer) micropatterned substrates induced higher upregulation in more genes in both Saos-2 and hOB cells (Figure 20, green and pink lines) the PLGA (softer).

When the effect of pillar density on Saos-2 cells seeded on PLLA was studied using PLLA P8G4 and P8G8 surfaces and Saos-2 cells (Figure 50), it was observed that P8G4 surfaces (higher pillar density) induced slightly higher upregulation than lower density surface (P8G8).

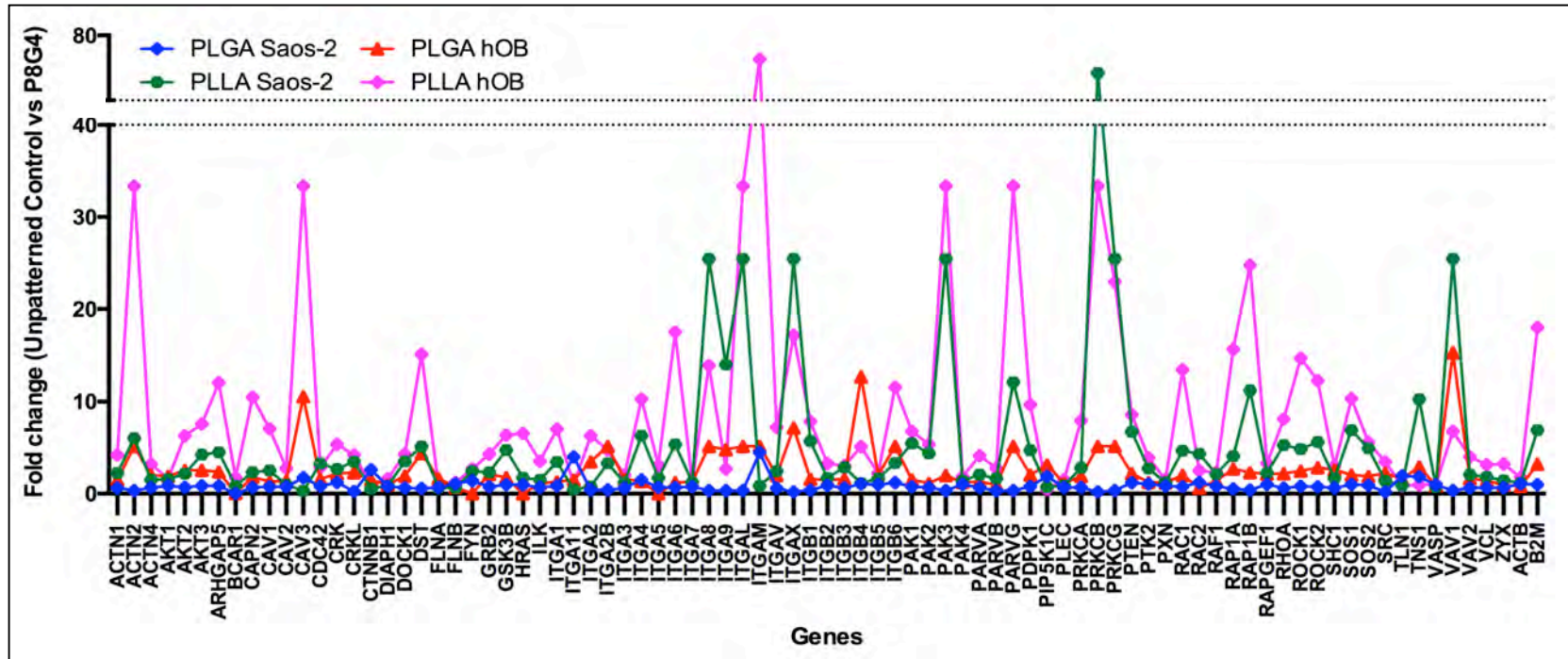


Figure 49: Fold changes of the focal adhesion genes for Saos-2 and hOB cells cultured on PLLA and PLGA substrates with P8G4 patterns. Ct values for normalized to GAPDH and fold changes were calculated against control surfaces for each cell type and surface.

Three pathways were selected: integrins, FAK signalling, and cytoskeletal regulators (Figure 51). When integrins are taken into consideration, the highest upregulation is observed in the hOB cells cultured on PLLA micropatterned substrate (Figure 51 A). Saos-2 cells on the same substrate showed the second highest response. ITGAL (integrin alpha L) and ITGAM (complement component 3 receptor 3 subunit) were upregulated (fold change >40) within hOB on PLLA group. These genes also have a role in osteogenic differentiation and were found to be upregulated in mesenchymal stem cells cultured on nanopatterned substrates (Dalby et al. 2007). Since hOB cells are immature osteoblast-like cells rather than fully differentiated osteocytes a similar mechanism of further osteodifferentiation may be induced by our micropillar array. Saos-2 cells on PLLA micropatterned substrate showed increased expression of ITGA8 (integrin subunit alpha 8) in addition to these genes. ITGA8 was reported to be mutated in some cases of osteosarcoma and differentially expressed in prostate cancer are proposed to be related to regulation of cell adhesion in cancer (Du et al., 2014; Gerald, 2003 respectively).

Two genes (PRKCB and PRKCG) from the FAK signaling pathway were upregulated in both Saos-2 and hOB cells on stiff micropatterned substrates (Figure 51 B). PRKCB (protein kinase C beta) and PRKCG (protein kinase C gamma) are protein kinases that phosphorylate histones and regulate methylation at a variety of gene promoter regions (Niini et al., 2014). This upregulation may indicate the effect of micropatterns on epigenetic regulations resulting from FAK pathway.

Cytoskeletal regulator gene results showed that ACTN 1,2 (actinin alpha 1 and 2) and were upregulated in hOB cells on micropatterned PLLA substrate (Figure 51 C). Focal adhesion structural proteins DST (dystonin) was highly upregulated and VCL (vinculin) and ZYX (zyxin) were moderately upregulated in Saos-2 and hOB on micropatterned PLLA substrates. When moderate upregulations in focal adhesion structural proteins and change in their cellular distribution (Figure 30, 31, and 32) considered, these proteins seem to be relocating according to the focal adhesions rather than being strongly upregulated by the physical cues of the substrate.

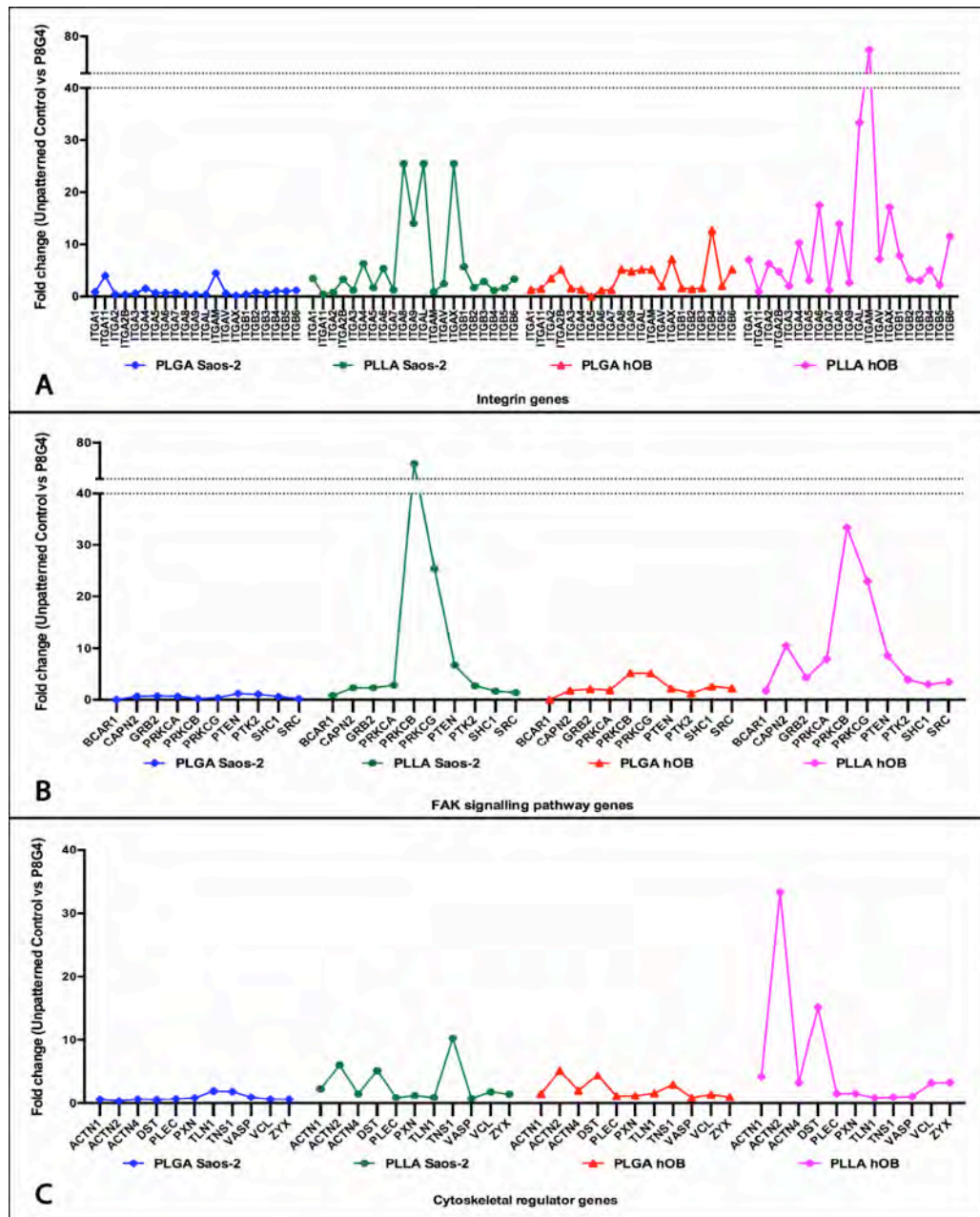


Figure 51: Fold changes of the 3 groups genes (integrins, FAK signaling pathway, cytoskeletal regulator genes) of focal adhesion PCR array for Saos-2 and hOB cells cultured on P8G4 PLLA and PLGA. Ct values normalized to GAPDH and fold changes were calculated against unpatterned controls for each cell type and surface.

3.7. Cell division and cell cycle progression on micropatterned substrates

3.7.1. Saos-2 Cells

Phases of mitosis are prophase, prometaphase, metaphase, anaphase and telophase. The cell division process is finalized with cytokinesis, which is the separation of cytoplasm for the two newly formed daughter cells. During these phases cells go through specific changes at predetermined times (Figure 52 A). Mitosis phases were studied with Saos-2 cells on micropatterned substrates. Cells were cultured on P8G4, P8G8 and P8G16 PLGA substrates for 48 h. Samples were stained for α -tubulin, actin and DNA, and imaged with CLSM (Figure 52). Previous experiments showed that Saos-2 cell nuclei deform extensively when cultured on such micropatterned substrates. What happens during cell division was not observed yet. For that purpose, samples were scanned for mitotic figures. Several mitotic figures were observed. During mitosis, Saos-2 cells lost their polygonal shape and assumed a circular form and proceeded to prophase, prometaphase, metaphase (Figure 52 B1), anaphase and telophase (Figure 52 B2). After cytokinesis (Figure 52 B3) they formed contacts with the substrate and nuclear deformations reappeared.

Deformation of the nucleus was observed in non-mitotic, adherent cells. Nuclear deformation was lost after the start of the cell division condensation of chromatin into chromosomes (Figure 52 B1). Nuclear deformation was again observed at the cytokinesis step again (Figure 52 B3). This was also observed within the z-stacks of CLSM (Figure 53), in which a Saos-2 cell at telophase with undeformed nuclear material (nuclear envelope disintegrates at prometaphase) was observed on top of the pillars, while Saos-2 cells that were not in mitotic cell division had deformed nuclei and were located in between the pillars (Figure 53).

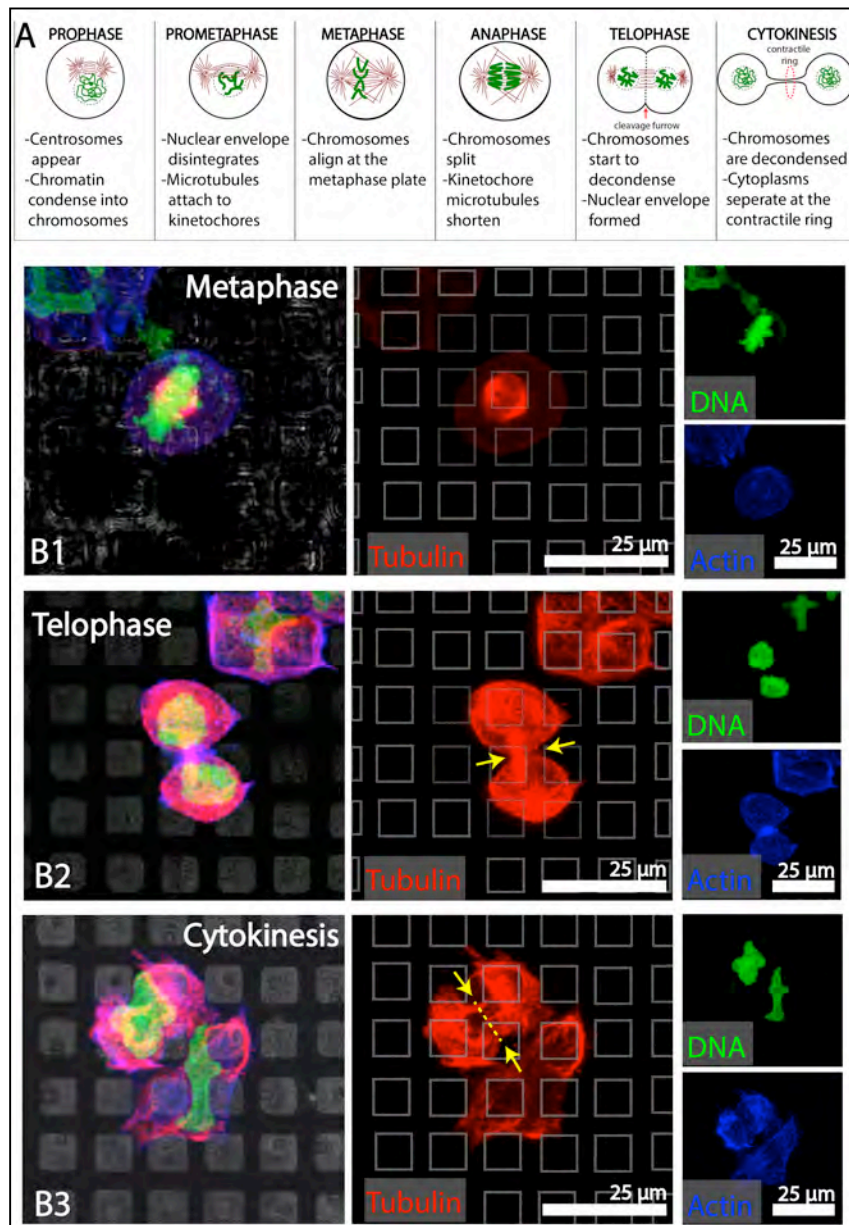


Figure 52: Schematic representation and microscopy of cell division phases. (A) Schematic representation of cell division (green: chromatin/chromosomes, red: kinetochores and microtubules, black: nuclear and cell membranes). (B) Confocal microscopy of dividing Saos-2 cells, (B1) metaphase, (B2) telophase, (B3) cytokinesis. Cells were cultured on PLGA P8G4 substrate for 48 h (B1, B2, B3 left panel overlaid images, middle panel tubulin showing mitotic spindles, right panel DNA and actin imaging; arrows: cleavage furrow; dashed lines: contractile ring; red: tubulin-Alexa goat anti mouse 488, green: DNA-DRAQ5, blue: actin-Alexa 532 Phalloidin, x40 objective)

Cells become round up during mitosis. From adherent state to round up for some of the actin cytoskeleton and FA were left on the substrate. These structures are called retraction fibers. While doing so they form retraction fibers that connect cell adhesion pattern to the rounded up mitotic cell body (Théry, 2010). In another study it was shown that mitotic cells have a dynamic subcortical actin network, whose form is biased by the initial adhesion geometry of the parent cell (Fink et al., 2011).

Théry et al. (2005) manufactured cell adhesive geometric shapes of ECM with microcontact printing on substrates. They studied dividing HeLa cells on those micropatterns. Cells conform to the ECM micropattern deforming their shapes. They concluded that spindle orientation is dependent on substrate geometry and actin fiber ruffles, which maintain the cell adhesion pattern during rounding up of the cell act as a guide for adhesion of two daughter cells. Our results that show cells rounding up during mitosis but regain a deformed geometry following cytokinesis is in agreement with their findings. Since daughter cells follow parents' adhesion pattern, they are also expected to deform following mitosis.

In another study was conducted with atypical Werner syndrome cells, a disease resulting from WS gene mutations together with Lamin A mutations and deformed, lobulated cell nuclei, prolonged S-phase and defective G2 phase checkpoint. They showed that Werner Syndrome cells undergo mitosis but at a slower rate. Nuclear deformations slowed down the cell cycle but did not affect centrosome number, assembly of the nuclear lamina and nuclear pore distribution (Adelfalk et al., 2005). It can therefore be proposed that nuclear shape and cell cycle progression are interrelated but not completely in unison. Mutation resulting in nuclear deformations does not completely interrupt cell cycle. These findings are also coherent with our results that mitotic figures were observed on micropatterned substrates (Figure 52) and the proliferation results (Cell Viability on Micropatterned Substrates, Figure 26), where cells cultured on surfaces known to induce more pronounced deformations (G4 family substrates) have slower proliferation rates.

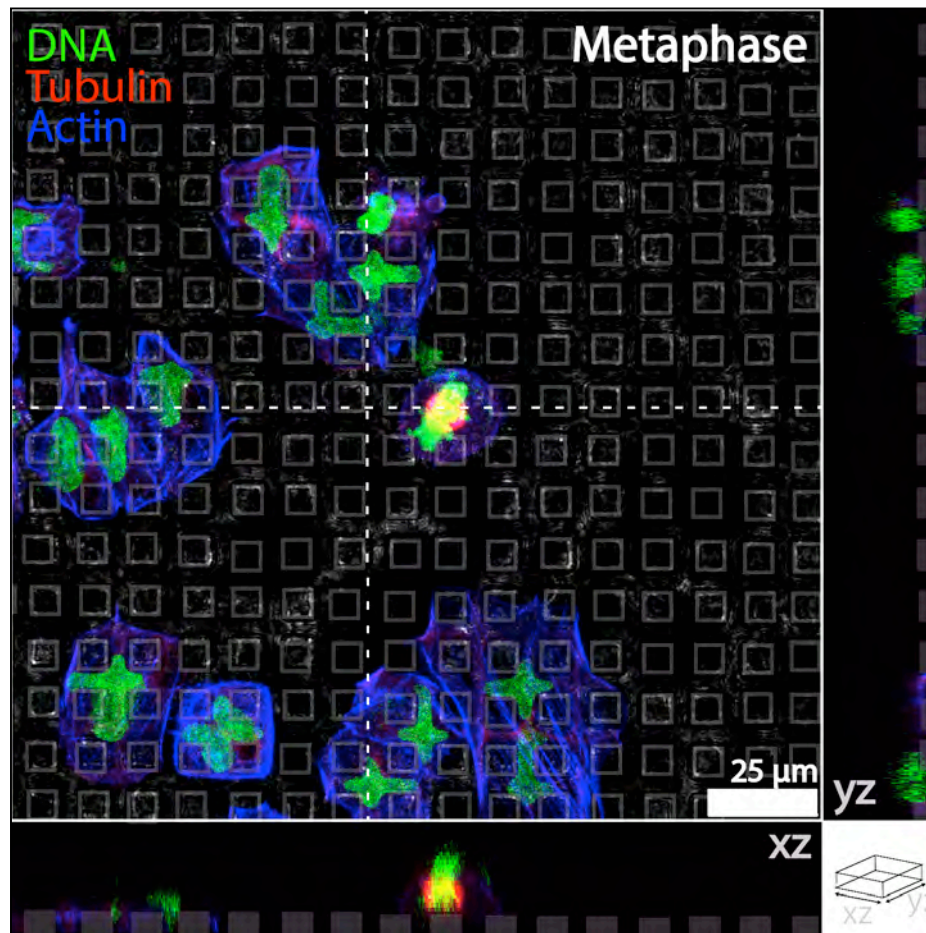


Figure 53: Top view and cross sections (at the edges as xz and yz axes) of Saos-2 cells cultured on P8G4 substrate. Crosshair shows the y-z and x-z section planes. On x-z section Saos-2 cell in metaphase was observed on top of the pillars while non mitotic cell (left side) nuclei are deformed and in between the pillars. On y-z section a non-mitotic deformed Saos-2 cell nuclei was observed. (dashed lines: cross section planes for x-z and y-z projections; red: tubulin-alexa goat anti mouse 488, green: DNA-DRAQ5, blue: actin-alexa 532 phalloidin, x40 objective)

3.7.2. MDA-MB-231 cells

MDA-MB-231 invasive breast carcinoma cell were used for cell cycle studies. Serum deprivation method was used for cell cycle synchronization at G0. In order to do so, adherent cells were deprived from serum (0.1 % FBS) for 24, 48 and 72 h (24 h SFM, 48 h SFM, 72 h SFM). G0 synchronization plateaued at 48 h (G0/G1: 24 h SM 63.60%, 24 h SFM 72.57%, 48 h SFM 77.79%, 72 h SFM 77.98%) (Figure 54 A). Serum was replenished after 48 h and recovery of the population from cell cycle arrest was observed for 4, 12 and 24 h (48h SFM+4h SM, 48h SFM+12h SM, 48h SFM+24h SM). Since 48 h serum deprivation had the best results, this time point was chosen for further experimentation.

Next 48h SFM cells and untreated cells were cultured on micropatterned and unpatterned PMMA films (Figures 54 A-B). Untreated cells cultured for 48h on unpatterned PMMA films had 69% of the population at G0/G1 and 48h SFM cells on the same substrate had 70% of the population at G0/G1 (Figures 54 B-C). On the other hand, untreated cells cultured for 48h on micropatterned PMMA films had 81% of the population at G0/G1 and 48h SFM cells on the same substrate had 82% of the population at G0/G1 (Figures 54 B-C).

Upon serum addition at 24 h highest number of cells were at G2/M stage (39%). On micropatterned surfaces with or without serum deprivation (24 h SM and 48 h SFM + 24 h SM) percentage of G0/G1 cells were similar to 48 h SFM on TCPS. This showed that P4G4 micropatterned substrate arrests cells at G0/G1 checkpoint in 24 h SM group and further lengthens G0/G1 arrest in 48 h SFM+ 2 4h SM group. An unpaired t-test result of the flow cytometric analysis of cell cycle was significant ($p < 0.05$). 48 h SFM + 24 h SM group had significantly higher fractions of G2/M cells ((%95 CI, $p < 0.01$). Cells cultured on unpatterned PMMA in SM and 48 h SFM + 24 h SM were not significantly different. Cells cultured on P4G4 PMMA in SM and 48 h SFM + 24 h SM were not significantly different.

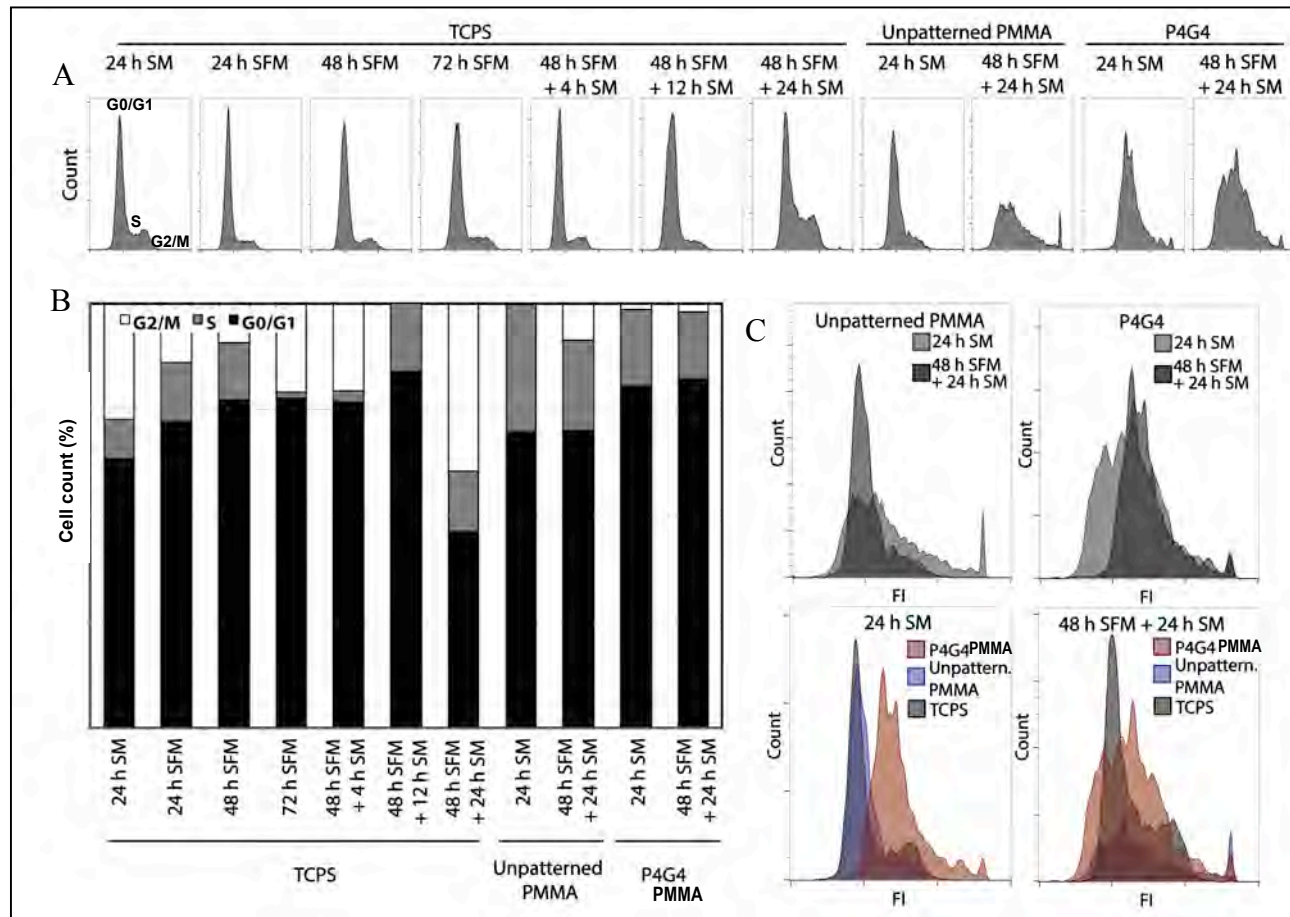


Figure 54: Cell cycle analysis of MDA-MB-231 cells using flow cytometry. (A) DNA quantification histograms of samples. (B) Cell counts of each sample for G0/G1, S and G2/M phases (%95 CI, $p < 0.05$). (C) Histograms of unpatterned PMMA, micropatterned PMMA, synchronization and control. (B: cell numbers in each cell cycle phase was normalized to total number of cells acquired)

Vergani et al. concluded from their studies on nuclear size and gene expression that as the cells were forced to occupy a smaller area, nuclear area also decreases resulting in chromosome condensation (Vergani et al., 2004). Beyec et al. demonstrated that forcing mammary epithelial cells to take a spherical geometry, histone deacetylation was increased, therefore, chromatin condensation was observed. Gene expression was reduced globally (Beyec et al., 2007). In an earlier study by Folkman and Moscona, it was shown that cell shape was tightly coupled with DNA synthesis. When the cells assume a spherical geometry they fail to enter S phase (Folkman et al., 1978). In their studies on cell confinement and geometry Chen et al. concluded that deformation of the cell or nucleus is a result of local mechanical cues which modifies cells to filter the same chemical input (from ECM or soluble factors) and express different functional outputs (proliferation vs apoptosis) (Chen et al., 1997). Results in the present study are in agreement with these studies such that forcing nuclear deformations slows down the cell cycle and decreases the M, G2/S subpopulation.

When samples treated with 24 SM or 48h SFM + 24h SM on P4G4 were stained with Ki-67 proliferation marker, 48 h SFM + 24 h SM showed higher fraction of cells stained positive for the proliferation marker compared to 24 h SM group (Figure 55 A-B). A mitotic and a non-mitotic adherent cell were imaged with CLSM. 57 images were gathered from the sample top to bottom corresponding to different focal plane sections (Figure 55 C). From the top to the 27th section only the mitotic cell (Figure 55 C, *m) was observed. After the 27th z-stack section, focal plane was at the level of micropatterns on the surface and the non-mitotic, adherent cell (Figure 55 C, *a) started to show. From these results and z-stack cross sections (Figure 55 D) it was concluded that during mitosis the cell is elevated from the micropatterned substrate and takes a spherical form. Also, during this process, nuclear deformation and cytoskeletal geometry are lost. This observation is also in agreement with Saos-2 cell micrographs in which mitotic cells lose their nuclear deformation and stay on top of the pillars during mitosis, while the non-mitotic cell nuclei deform in between the pillars (Figure 53).

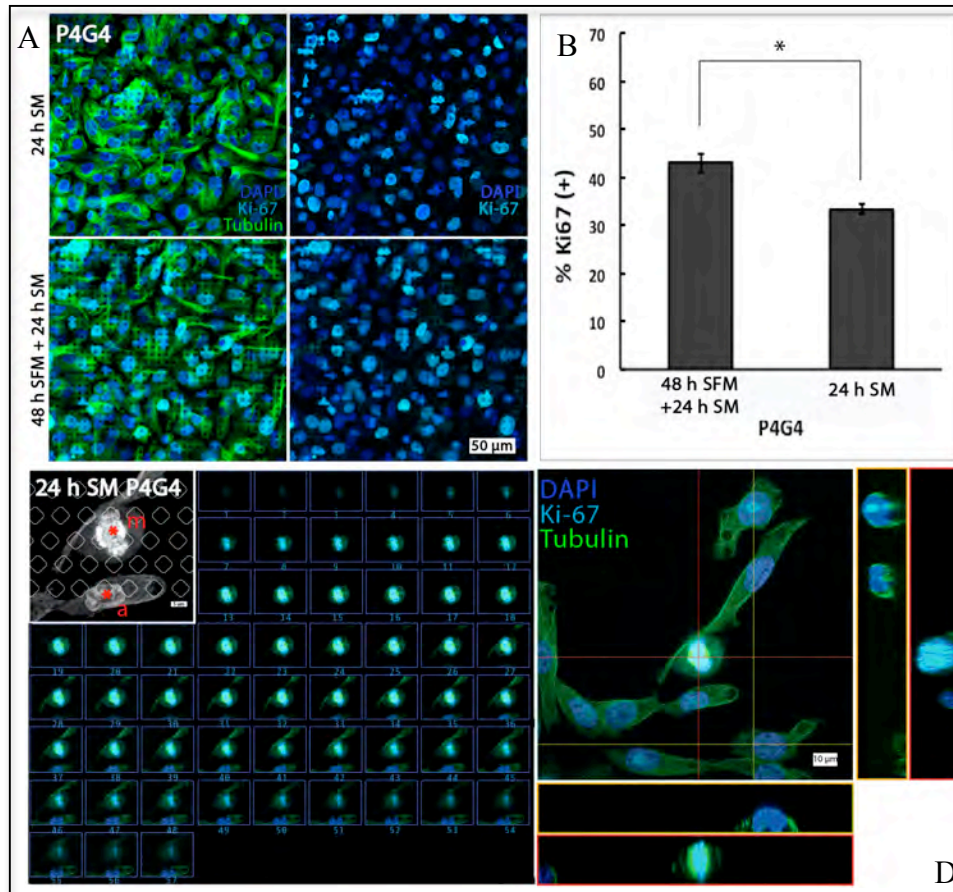


Figure 55: Immunocytochemistry of MDA-MB-231 cells with Ki67, tubulin- α and DAPI. (A) MDA-MB-231 cells on P4G4 micropatterned surfaces were treated with 10% FBS (24 h SM) and G0 synchronization procedure (48 h SFM + 24 h SM) and labeled for Ki-67 proliferation marker, tubulin and DNA for tracking mitosis. (B) Ki-67 positive cell percentages were calculated from CLSM images. (n=3, p<0.5). (C) CLSM images were taken for the MDA-MB-231 cell during mitosis from 24 h SM group. (mitosis (*m), adherent cell (*a)). (D) Cross sections of MDA-MB231 cells cultured on micropatterned substrate. Crosshair shows the y-z and x-z section planes. (Blue: DAPI, cyan: Ki67, green: tubulin- α , A: x20 objective, C-D: x63 objective)

3.7.3. Regulation of Cell Cycle in MDA-MB231 and MCF-7 Cells on Micropatterned Substrates

Cell cycle regulation of breast carcinoma cells (MDA-MB231 and MCF-7) were studied with qPCR for cell cycle regulation related genes Cyclins A2, B1, E2, p21 and p27. Proliferation was tested with Ki-67 proliferation marker. Cells were cultured on unpatterned and micropatterned PMMA substrates for 12, 24, 48, 72 h.

Ki-67 PCR results show no change at 12 h for MCF-7 and MDA-MB231 cells cultured on micropatterned substrate compared to unpatterned control (Figure 56). Since PMMA is hydrophobic and prevents instant cell attachment, these results were interpreted towards the senescent state of the cell during adhesion process. At 24 h Ki-67 was ca. 3-fold upregulated in MDA-MB231 cells and its expression decreased at 48 h and downregulated at 72 h. On the other hand, the maximum Ki-67 upregulation was observed at 48 h in MCF-7 cells and a similar downregulation like MDA-MB231 was observed at 72 h. This time window of decreased expression over 2 days correlates with the expected attachment and nuclear deformation of the cells. Since MDA-MB231 is a more aggressive carcinoma cell type, a faster response to physical cues are expected.

Cell cycle regulators Cyclin A, B and p21 expressions were studied. There was no significant change in Cyclin A expression by MCF-7 and MDA-MB231 cells cultured on micropatterned substrates (Figure 57). Cyclin B mRNA levels of MDA-MB231 cell were downregulated but stable until 72 h, but showed more significant downregulation at 72 h (Figure 58). Cyclin B levels were unchanged for MCF-7 cells. In MCF-7 cell cycle inhibitor p21 mRNA levels were upregulated over 72 h (Figure 59). In MDA-MB231 cells, p21 mRNA levels were upregulated for all time points. These downregulations in cell cycle control genes and upregulation of inhibitory gene p21 are related to the cell cycle arrest observed with flow cytometry (Figure 54).

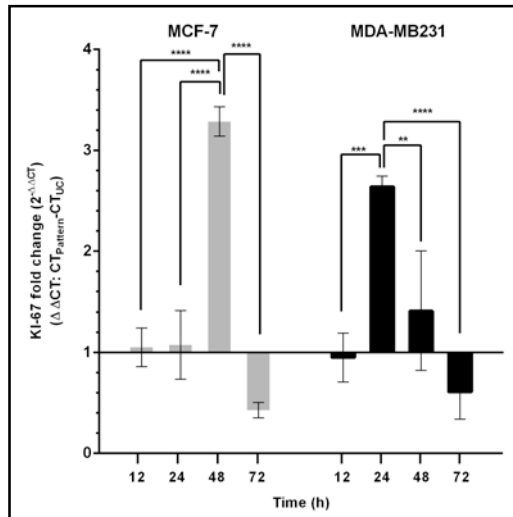


Figure 56: Ki-67 mRNA levels of MCF-7 and MDA-MB231 cells cultured on micropatterned substrates for up to 72 h. mRNA CT values were normalized to GAPDH (ΔCT) and to unpatterned control ($\Delta\Delta CT$). (One-Way ANOVA, $p < 0.001$, Tukey test for pairwise comparison, * $p < 0.05$, ** $p < 0.01$, *** $p < 0.005$, **** $p < 0.001$, $n = 4$)

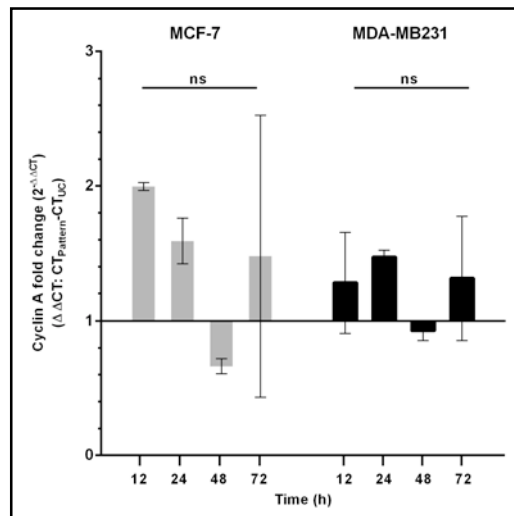


Figure 57: Cyclin A mRNA levels of MCF-7 and MDA-MB231 cells cultured on micropatterned substrates for up to 72 h. mRNA CT values were normalized to GAPDH (ΔCT) and to unpatterned control ($\Delta\Delta CT$). (One-Way ANOVA, $p < 0.001$, Tukey test for pairwise comparison, * $p < 0.05$, ** $p < 0.01$, *** $p < 0.005$, **** $p < 0.001$, $n = 4$)

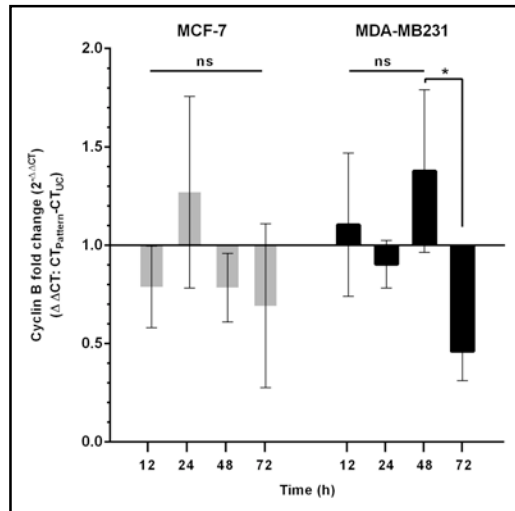


Figure 58: Cyclin B mRNA levels of MCF-7 and MDA-MB231 cells cultured on micropatterned substrates for up to 72 h. mRNA CT values were normalized to GAPDH (ΔCT) and to unpatterned control ($\Delta\Delta\text{CT}$). (One-Way ANOVA, $p < 0.001$, Tukey test for pairwise comparison, * $p < 0.05$, ** $p < 0.01$, *** $p < 0.005$, **** $p < 0.001$, $n=4$)

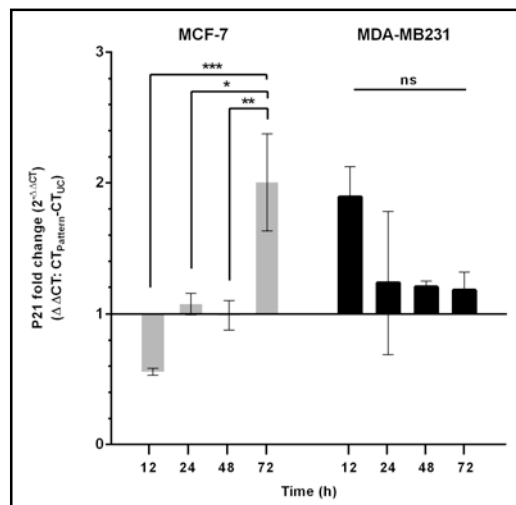


Figure 59: p21 mRNA levels of MCF-7 and MDA-MB231 cells cultured on micropatterned substrates for up to 72 h. mRNA CT values were normalized to GAPDH (ΔCT) and to unpatterned control ($\Delta\Delta\text{CT}$). (One-Way ANOVA, $p < 0.001$, Tukey test for pairwise comparison, * $p < 0.05$, ** $p < 0.01$, *** $p < 0.005$, **** $p < 0.001$, $n=4$)

3.8. Effect of Micropatterned Substrates on Epithelial-to-Mesenchymal Transition (EMT) of Breast Carcinoma Cells

3.8.1. Expression of EMT Markers

Epithelial-to-mesenchymal transition is a key event in cancer cell migration and metastasis (Samatov et al., 2013). In order to study the EMT inducing capacity of micropatterned substrates, MDA-MB231 and MCF-7 cells were cultured for 12, 24, 48 and 72 h. At each time point, expression of mesenchymal marker vimentin and epithelial marker E-cadherin expression was studied with PCR.

Cells cultured on TCPS were used as the control of baseline expression of vimentin and E-cadherin in MDA-MB231 and MCF-7 cells. Expression of each marker was normalized to HKG (GAPDH, Δ CT) and in order to compare the expression of both cell lines, MDA-MB231 expression was normalized to MCF-7 ($\Delta\Delta$ CT). MDA-MB231 cells showed 200 fold higher vimentin expression (Figure 60). Since this cell line is originated from a triple negative tumor (ER-/PR-/Her2/neu-) and has invasive capacity (Thompson et al. 1992) it is expected to have more mesenchymal characteristics and higher expression of vimentin. Similarly, epithelial marker E-cadherin expressions of MDA-MB231 cells were substantially lower (Figure 60), and this could easily be explained by the same mechanism presented above.

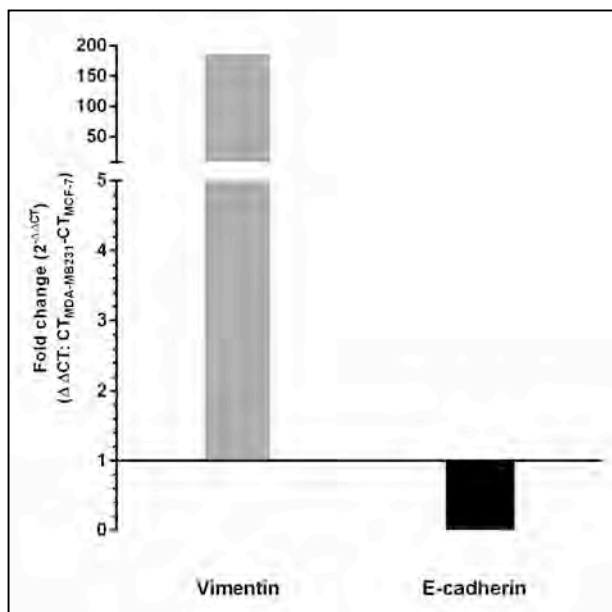


Figure 60: Basal vimentin and E-cadherin expression of MDA-MB231 cells compared to MCF-7 cells. (MDA-MB231 mRNA CT values were normalized to GAPDH (ΔCT) and to MCF-7 ($\Delta\Delta CT$))

Vimentin expression of MDA-MB231 and MCF-7 cells over 72 h on micropatterned substrates were different (Figure 61). MDA-MB231 cells showed a small amount of upregulation (<2 folds) for up to 48 h and at 72 h it was downregulated compared to the unpatterned control. The differences between these results were not significant (One-Way ANOVA, $p > 0.05$). On the other hand MCF-7 vimentin expression results were significant and showed a 2 fold increase until 48h (One-Way ANOVA, $p < 0.05$).

Mendez et al. performed studies with breast carcinoma cell lines (MDA-MB231, MCF-7 etc.) and role of vimentin EMT and proposed that cell shape changes (i.e. flattening) are induced by vimentin expression and facilitates the ability of the cell to withstand mechanical stimuli from microenvironment, which might be critical for metastatic cell survival (Mendez et al., 2010). Since vimentin expression is a survival mechanism against mechanical stimuli, increase in vimentin expression was expected because micropatterned substrates force the cells to deform.

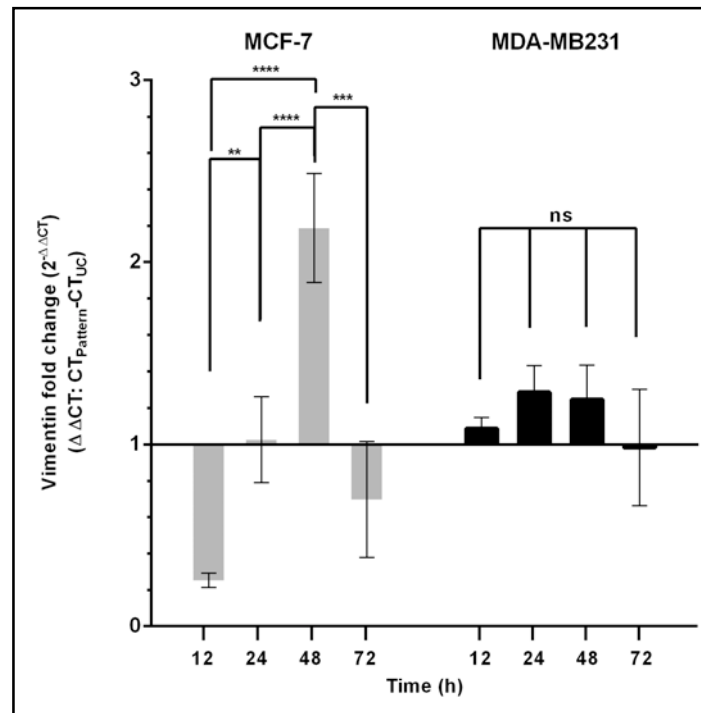


Figure 61: Vimentin mRNA levels of MCF-7 and MDA-MB231 cells cultured on micropatterned substrates for up to 72 h. mRNA CT values were normalized to GAPDH (Δ CT) and to unpatterned control ($\Delta\Delta$ CT). (One-Way ANOVA, $p < 0.001$, Tukey test for pairwise comparison, * $p < 0.05$, ** $p < 0.01$, *** $p < 0.005$, **** $p < 0.001$, $n = 4$)

E-cadherin expressions of MDA-MB231 and MCF-7 cells showed different trends (Figure 62). For MCF-7 cells E-cadherin was downregulated at all the time points. However, this change was not significant between the time points tested (One-Way ANOVA, $p > 0.05$). Since MCF-7 cell had a significantly higher baseline E-cadherin expression and more epithelial phenotype, the induced cell and nuclear shape deformations resulted in the decrease of the epithelial marker. MDA-MB231 cells on the other hand showed a 5 fold increase at 12 h but E-cadherin expression decreased over time and was downregulated at 72 h significantly (One-Way ANOVA, $p < 0.05$).

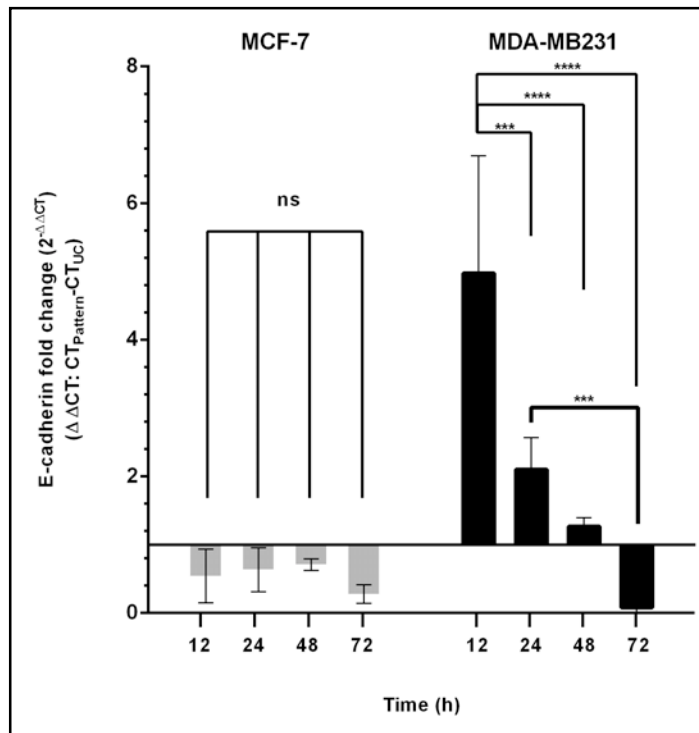


Figure 62: E-cadherin mRNA levels of MCF-7 and MDA-MB231 cells cultured on micropatterned substrates for up to 72 h. mRNA CT values were normalized to GAPDH (ΔCT) and to unpatterned control ($\Delta\Delta CT$). (One-Way ANOVA, $p < 0.001$, Tukey test for pairwise comparison, * $p < 0.05$, ** $p < 0.01$, *** $p < 0.005$, **** $p < 0.001$, $n=4$)

3.8.2. Immunohistochemistry of EMT Markers

The two most commonly used EMT markers, E-cadherin and vimentin, were used in the immunohistochemistry studies. MDA-MB231 cells were cultured on the control and P4G4 PMMA films for 1, 4 and 7 days. Antibodies for E-cadherin and vimentin were used in staining (Figure 63). Signal intensities for each antibody was measured using NIH ImageJ software from x20 CLSM images from separate channels (647 laser-vimentin, 532 laser-E-cadherin) (Figure 64). On the control surface on day 1 Vimentin/E-cadherin ratio was smaller than 1, and E-cadherin had slightly higher intensity compared to vimentin (Figure 63 left panel, Figure 64). On day 4, E-cadherin and vimentin intensities were similar and their ratio was ca. 1 and on day 7 both intensities were lower on control. On the control vimentin/ E-cadherin ratio was higher on days 4 and 7 compared to day 1 (Figure 64). On P4G4, surface E-cadherin intensities were lower than the control at all time points (Figure 63 right panel). E-cadherin intensity decreased on day 4 and day 7 and this decrease was reflected on the vimentin/E-cadherin ratio (Figure 64) as a significant increase compared to day 1.

E-cadherin expression could be down regulated through integrin binding and FAK activation. This pathway is connected to the Ras/Raf/MEK/ERK pathway, which represses E-cadherin through Slug (Jiang et al., 2013). Cell shape is an important parameter in EMT and is regulated via cues from the microenvironment (O'Connor et al., 2014). Nelson et al. concluded after their studies on micropatterned substrates with EMT of breast carcinoma cells that E-cadherin cleavage may not be the cause of EMT but it is necessary to allow cell-cell junction breakdown and consequent cell spreading (Nelson et al., 2008). Observed down regulation of E-cadherin in the present experiments may be the result of the drastic shape changes induced by the micropatterned substrates. The transition from cuboidal, cobblestone geometry of epithelial tissue to elongated, spindle like geometry of mesenchymal cells might be the cornerstone of EMT.

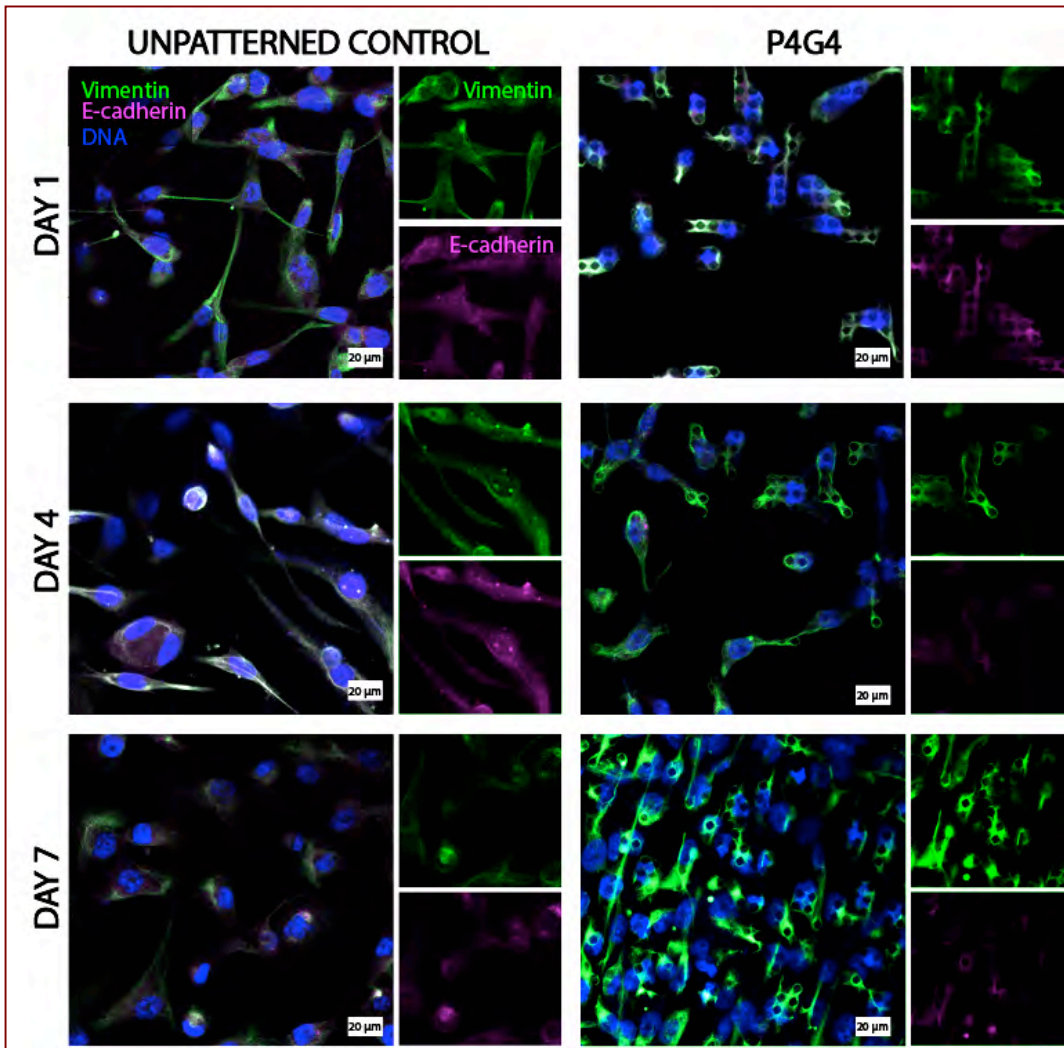


Figure 63: CLSM images of MDA-MB231 cells cultured on control and P4G4 surfaces up to 7 days. Cells were stained for vimentin (chicken anti-vimentin, donkey anti-chicken Alexa 647) and E-cadherin (mouse anti-E-cadherin, donkey anti-mouse Rhodamin Red), DAPI and imaged with a x20 objective.

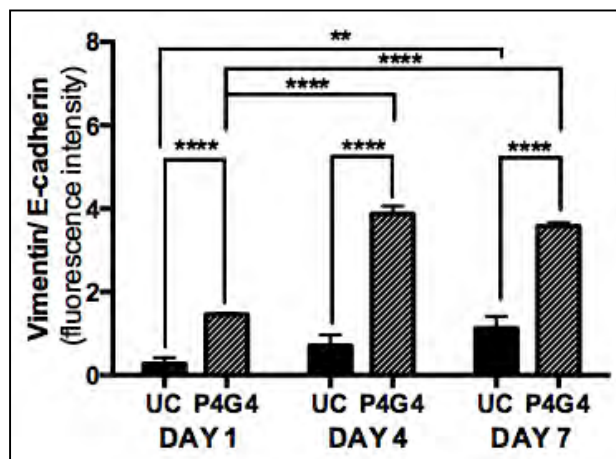


Figure 64: Vimentin/E-cadherin ratios of the MDA-MB231 cells cultured on control and P4G4 surfaces up to 7 days. Fluorescence intensities were calculated using the CLSM images and NIH ImageJ software from each corresponding channel (647 laser-vimentin, 532 laser-E-cadherin) (One-way ANOVA, $p < 0.001$, Tukey test for pairwise comparison, * $p < 0.05$, ** $p < 0.01$, *** $p < 0.005$, ****

3.9. RNA Sequencing of MDA-MB231 Cells on Micropatterned Substrates

MDA-MB231 cells were cultured on TCPS (48h SM, 48h SFM+12h SM) and on micropatterned and unpatterned PMMA (48h SM). Cells were harvested and pooled into 3 samples for each category. Total RNA was isolated and quality checked by Bioanalyzer. All samples had RIN (RNA Integrity Number) > 8 . PCA (Principal Component Analysis) of protein coding gene expression was plotted (Appendix E1). According to the 1st principal component, 48 h SM micropatterned and 48 h SFM+12 h SM TCPS groups fall into same quadrant and according to the 2nd principal component they fall into different quadrants. Only one of the three 48 h SM unpatterned samples was an outlier (Sample 2). Correlation of samples within each group was high (Appendix E2).

Reads of the 77 genes playing role in epithelial to mesenchymal transition pathway were plotted for all samples (Figure 65). 19 of those 77 genes were enriched in

samples cultured on the micropatterns. These are WNT5A, WNT5B, TMEM132A, MMP2, MMP9, VIM, CDH2, PTK2, PLEK2, JAG1, ITGA5, ITGAV, ITGB1, SERPINE1, STEAP1, KRT7, MSN, TFPI2 and PDGFRB.

WNT5A and WNT5B were enriched in the micropatterned samples (Figure 65). In one study on expression of Wnt ligands of breast carcinoma cell lines, it was found that breast carcinoma cell lines do not express non-canonical Wnt ligands WNT5A and WNT5B (Benhaj et al., 2006). Yüzügüllü et al. used hepatocellular carcinoma, and proposed that canonical Wnt ligands play a role in tumor initiation and non-canonical (WNT5A and WNT5B) pathway plays a role in tumor progression (Yüzügüllü et al., 2009).

MMP2 and MMP9 were enriched in micropatterned samples (Figure 65). EMT is often connected to increased matrix metalloproteinase (MMP) production (Lee et al., 2006). MMP2 and MMP9 were shown to have important roles in invasion and metastasis by degrading ECM substrates like collagen type IV (Björklund et al 2005).

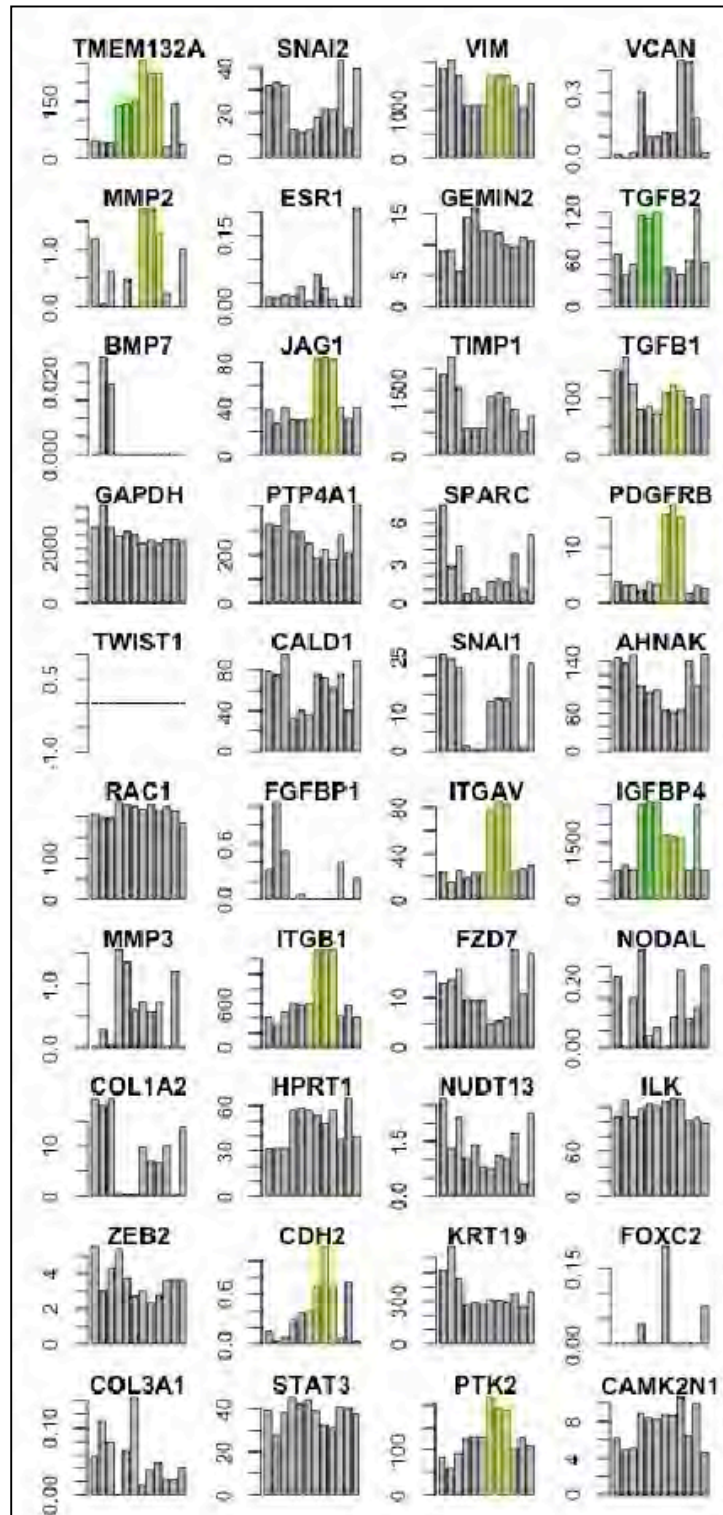


Figure 65: RNA sequencing results for EMT related genes of TCPS (48h SM, 48h SFM+12h SM) and micropatterned and unpatterned PMMA (48h SM) samples (*continued*).

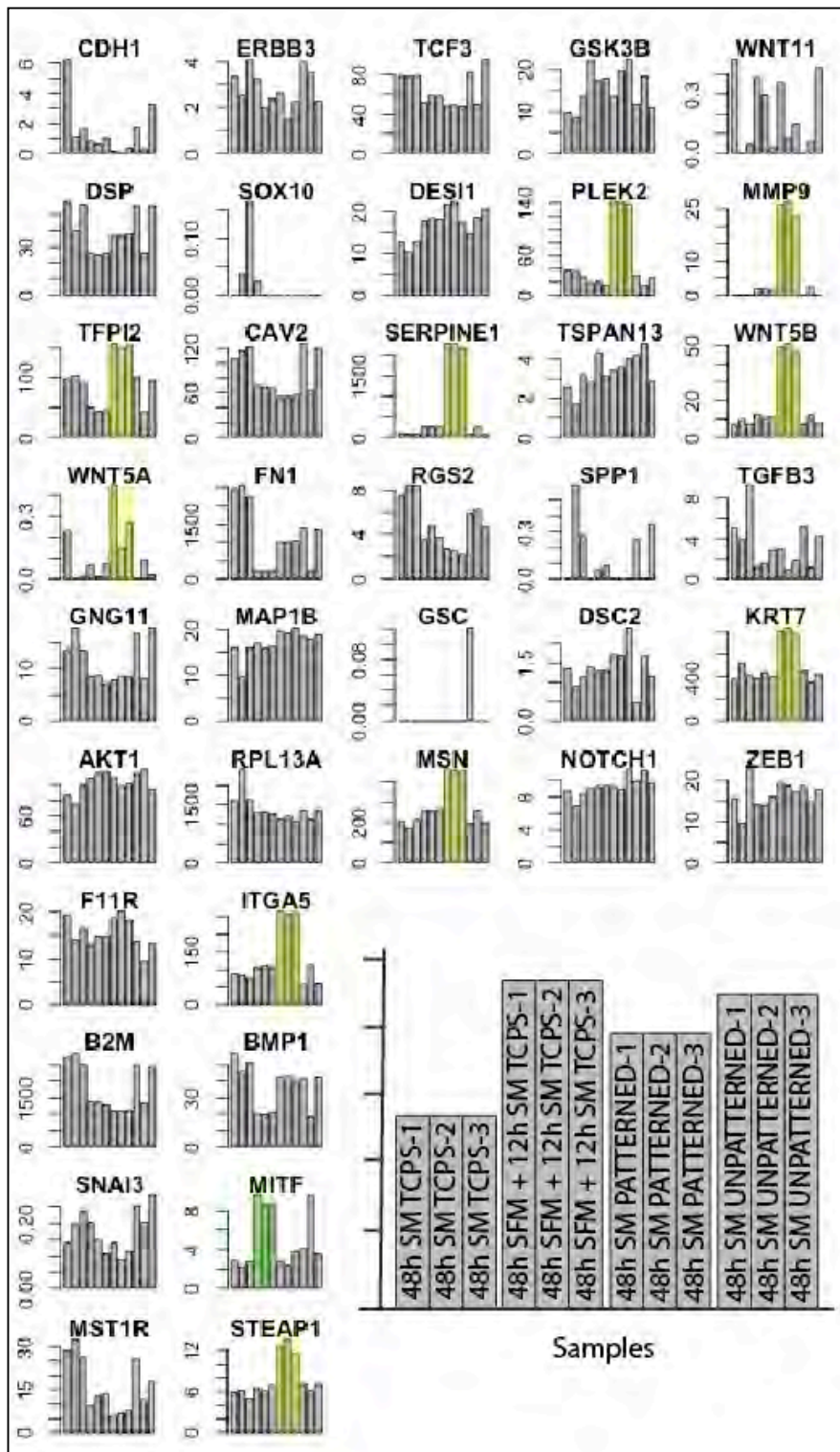


Figure 65 (continued): Three samples from each group were sequenced. (x axis: samples, y axis: read frequency)

Gene ontology (GO) term enrichment analysis were performed to compare of 4 sets of experiments. When 48h SM TCPS vs 4 8h SFM+12 h SM TCPS groups were compared for significant GO terms ($p < 0.001$) (Table 6), cell cycle arrest resulting from serum deprivation was reflected in top 15 GO terms, where 4 of these were related to cell division related terms.

Table 6: Gene ontology (GO) enrichment in 48 h SM TCPS vs 48 h SFM+12 h SM TCPS groups. Top 15 enrichment results were tabulated ($p < 0.001$). Serum starvation for cell cycle synchronization was performed for 48 h SFM+12 h SM TCPS group. 4 of 15 enriched GO categories belong to cell division related terms.

48h SM TCPS vs 48h SFM+12h SM TCPS						
	GO ID	GO Term	No of genes in annotated category	No of genes in sample	No of genes expected in sample	p value
1	GO:0007067	mitotic nuclear division	342	217	158.52	5.1e-07
2	GO:0090200	positive regulation of release of cytoch...	24	22	11.12	3.8e-06
3	GO:0000281	mitotic cytokinesis	28	24	12.98	1.9e-05
4	GO:0008285	negative regulation of cell proliferatio...	495	274	229.44	2.5e-05
5	GO:0007264	small GTPase mediated signal transductio...	738	393	342.08	6.2e-05
6	GO:0043687	post-translational protein modification	267	155	123.76	6.9e-05
7	GO:0008284	positive regulation of cell proliferatio...	596	322	276.26	7.0e-05
8	GO:0051301	cell division	528	304	244.74	7.9e-05
9	GO:0006614	SRP-dependent cotranslational protein ta...	71	49	32.91	9.1e-05
10	GO:0036498	IRE1-mediated unfolded protein response	54	39	25.03	0.00010
11	GO:0032269	negative regulation of cellular protein ...	758	412	351.35	0.00011
12	GO:0043393	regulation of protein binding	137	85	63.50	0.00015
13	GO:0009968	negative regulation of signal transducti...	802	431	371.74	0.00016
14	GO:0051345	positive regulation of hydrolase activit...	637	336	295.26	0.00051
15	GO:0006417	regulation of translation	235	134	108.93	0.00059

Other comparisons were made between 48 h SM TCPS – 48 h Micropatterned groups (Table 7) and 4 8h SM TCPS – 48 h SM Unpatterned groups (Table 8). There were 4 cell division-related terms in micropatterned and 7 cell division-related terms in the unpatterned group. This shows that not just micropatterns but also substrate stiffness and chemistry have an effect on cell cycle progression.

Table 7: Gene ontology (GO) enrichment in 48 h SM TCPS vs 48 h Micropatterned groups. Top 15 enrichment results were tabulated ($p < 0.001$). Serum starvation for cell cycle synchronization was performed for 48 h SFM+12 h SM TCPS group. 4 of 15 enriched GO categories belong to cell division related terms.

48h SM TCPS vs 48h SM Micropatterned						
	GO ID	GO Term	No of genes in annotated category	No of genes in sample	No of genes expected in sample	p value
1	GO:0016032	viral process	599	381	314.38	2.4e-05
2	GO:0042493	response to drug	328	208	172.15	3.3e-05
3	GO:0006614	SRP-dependent cotranslational protein ta...	71	54	37.26	3.6e-05
4	GO:0035666	TRIF-dependent toll-like receptor signal...	68	52	35.69	3.9e-05
5	GO:0043687	post-translational protein modification	267	172	140.13	4.4e-05
6	GO:0010039	response to iron ion	24	22	12.60	4.7e-05
7	GO:0034138	toll-like receptor 3 signaling pathway	81	60	42.51	5.3e-05
8	GO:0000086	G2/M transition of mitotic cell cycle	161	109	84.50	5.7e-05
9	GO:0018279	protein N-linked glycosylation via aspar...	103	73	54.06	0.00010
10	GO:0006379	mRNA cleavage	14	14	7.35	0.00012
11	GO:0007067	mitotic nuclear division	342	227	179.50	0.00015
12	GO:0043393	regulation of protein binding	137	93	71.90	0.00017
13	GO:0000070	mitotic sister chromatid segregation	105	73	55.11	0.00027
14	GO:0002755	MyD88-dependent toll-like receptor signa...	71	52	37.26	0.00027
15	GO:0000082	G1/S transition of mitotic cell cycle	215	144	112.84	0.00029

Table 8: Gene ontology (GO) enrichment in 48 h SM TCPS vs 48 h SM Unpatterned groups. Top 15 enrichment results were tabulated ($p < 0.001$). Serum starvation for cell cycle synchronization was performed for 48 h SFM+12 h SM TCPS group. 7 of 15 enriched GO categories belong to cell division related terms.

48h SM TCPS vs 48h SM Unpatterned						
	GO ID	GO Term	No of genes in annotated category	No of genes in sample	No of genes expected in sample	p value
1	GO:0019083	viral transcription	131	39	15.08	1.2e-08
2	GO:0006614	SRP-dependent cotranslational protein ta...	71	25	8.17	1.4e-07
3	GO:0000184	nuclear-transcribed mRNA catabolic proce...	80	26	9.21	4.9e-07
4	GO:0006270	DNA replication initiation	32	15	3.68	6.4e-07
5	GO:0051301	cell division	528	109	60.79	8.7e-07
6	GO:0006271	DNA strand elongation involved in DNA re...	29	13	3.34	6.8e-06
7	GO:0006414	translational elongation	142	35	16.35	8.5e-06
8	GO:0000086	G2/M transition of mitotic cell cycle	161	38	18.54	1.1e-05
9	GO:0007076	mitotic chromosome condensation	11	7	1.27	5.7e-05
10	GO:0006415	translational termination	126	30	14.51	7.3e-05
11	GO:0007067	mitotic nuclear division	342	82	39.37	0.00010
12	GO:0032201	telomere maintenance via semi-conservati...	19	9	2.19	0.00011
13	GO:0006413	translational initiation	197	41	22.68	0.00011
14	GO:0034502	protein localization to chromosome	28	11	3.22	0.00015
15	GO:0000082	G1/S transition of mitotic cell cycle	215	43	24.75	0.00019

Table 9: Gene ontology (GO) enrichment in 48 h SM Unpatterned vs 48 h SM Micropatterned groups. Top 15 enrichment results were tabulated ($p < 0.001$). Serum starvation for cell cycle synchronization was performed for 48 h SFM+12 h SM TCPS group. 3 of 15 enriched GO categories belong to cell polarity, mechanotransduction and migration related terms.

48h SM Unpatterned vs 48h SM Micropatterned						
	GO ID	GO Term	No of genes in annotated category	No of genes in sample	No of genes expected in sample	<i>p</i> value
1	GO:0001666	response to hypoxia	216	120	85.67	1.4e-06
2	GO:0030574	collagen catabolic process	63	42	24.99	1.3e-05
3	GO:0090162	establishment of epithelial cell polarit...	12	12	4.76	1.5e-05
4	GO:0018146	keratan sulfate biosynthetic process	23	19	9.12	3.1e-05
5	GO:0051259	protein oligomerization	333	168	132.08	3.4e-05
6	GO:0046627	negative regulation of insulin receptor ...	25	20	9.92	4.6e-05
7	GO:0032331	negative regulation of chondrocyte diffe...	17	15	6.74	5.0e-05
8	GO:2001235	positive regulation of apoptotic signali...	159	87	63.06	7.9e-05
9	GO:0071260	cellular response to mechanical stimulus	59	38	23.40	0.00010
10	GO:0000122	negative regulation of transcription fro...	557	263	220.92	0.00013
11	GO:0045732	positive regulation of protein catabolic...	209	109	82.90	0.00015
12	GO:0045740	positive regulation of DNA replication	54	35	21.42	0.00016
13	GO:0044093	positive regulation of molecular functio...	1374	644	544.97	0.00017
14	GO:0060337	type I interferon signaling pathway	60	38	23.80	0.00017
15	GO:0030335	positive regulation of cell migration	283	142	112.25	0.00018

CHAPTER 4

CONCLUSION

Surface features in the form of micropatterns are valuable tools to be used to study interactions between cells and materials. Nanotechnology makes engineering of highly controlled surfaces possible. In this study an array of 9 micropatterned substrates made of degradable and non-degradable synthetic polymers were used to study nuclear deformation, forces generated by cells, focal adhesion signaling, proliferation and EMT of cancerous and non-cancerous cell types.

Deformation of cell nucleus is a property of cell type and micropatterned substrates. Using a single cell type, the effect of pillar size and interpillar spacing were studied. Interpillar spacing was found to be the most important parameter that affects nuclear deformation. After finding the surface that deforms the cell nucleus the most, different cell types were studied. Cancer cells showed the most significant nuclear deformations while with non-cancerous cells deformation of the nuclei was limited. Different cell types and also cells within a single population showed a spectrum of deformation behavior. Rectangularity and circle variance were shape related properties that distinguished the cells best.

Cells exert forces to the substrate to attach and to migrate. Micropatterned substrates made visualization of these forces possible. Pillars bend under the force that cells exert. Images of bent pillars are obtained with electron microscopy and forces that cells exerted on micropillars are calculated from the extent on bending and pillar properties. The magnitude of these forces varied with cell type, pillar dimensions and

stiffness. Using same size pillars but increasing interpillar spacings (from 4 μm to 16 μm) allowed to the influence of pillar density on forces that cells generate. Besides, using soft and stiff substrates showed that cells generate forces depending on the substrate's mechanical properties. Combining micropattern design and substrate materials one can test the mechanotransduction pathway from the perspective of cellular traction forces. In this study short interpillar distances and soft materials led to smaller pillar displacements and forces generated.

Advanced molecular biology tools were used in this study to show the effect of micropatterned substrates on several signaling pathways. Focal adhesions that take a central role in the initiation and transfer of mechanical stimuli are an agglomeration of many interacting proteins. PCR array was used to quantify the changes in focal adhesion-related genes. Micropatterned substrates affected expression of these genes and some genes were more upregulated than the others, showing that interaction with substrates is important in activation of specific pathways.

Micropatterned substrates have an influence on cell fate. It is shown in this study that cell cycle and epithelial or mesenchymal phenotype of breast carcinoma cells were affected whether they were cultured on a micropatterned or smooth substrate.

Micropatterned substrates had an influence on fate of stem cells. It was shown in this study that cell cycle and phenotype (epithelial or mesenchymal) of breast carcinoma cells were affected depending on whether they were cultured on a micropatterned or smooth substrate.

All these findings together support the initial hypothesis: micropatterned substrates activate intracellular mechanotransduction pathways, resulting in a series of coordinated events: focal adhesion related proteins are activated, force is conducted to the nucleus causing the nucleus to deform, and mechanotransduction, cell cycle and cell fate related genes change are expressed differently.

This study introduced the affects micropatterned substrates through mechanotransduction pathways on cellular processes. Further studies especially focused on pathways are required. Detailed studies of the genes that stood out in

PCR arrays and in total RNA sequencing are good candidates to be the key regulators in invasion and metastasis in cancer because these processes are directly related to the sensing of the substrate.

In conclusion, micropatterned substrates influence many different cellular processes, to different levels. Nuclear deformation is a major result caused by the substrate geometry, and is an indicator of differences between cell types (cancer vs non-cancer) and the properties determined enable (circularity, etc) quantification.

REFERENCES

- Adelfalk, C., Scherthan, H., Hirsch-Kauffmann, M., & Schweiger, M. (2005). Nuclear deformation characterizes Werner syndrome cells. *Cell biology international*, 29(12), 1032-1037.
- Agrelo, R., Setien, F., Espada, J., Artiga, M. J., Rodriguez, M., Pérez-Rosado, A., ... & Esteller, M. (2005). Inactivation of the lamin A/C gene by CpG island promoter hypermethylation in hematologic malignancies, and its association with poor survival in nodal diffuse large B-cell lymphoma. *Journal of clinical oncology*, 23(17), 3940-3947.
- Athanasiou, K. A., Niederauer, G. G., & Agrawal, C. M. (1996). Sterilization, toxicity, biocompatibility and clinical applications of polylactic acid/polyglycolic acid copolymers. *Biomaterials*, 17(2), 93-102.
- Badique, F., Stamov, D. R., Davidson, P. M., Veuillet, M., Reiter, G., Freund, J. N., ... & Anselme, K. (2013). Directing nuclear deformation on micropillared surfaces by substrate geometry and cytoskeleton organization. *Biomaterials*, 34(12), 2991-3001.
- Bao, G., & Suresh, S. (2003). Cell and molecular mechanics of biological materials. *Nature materials*, 2(11), 715-725.
- Bastioli, C. (Ed.). (2005). *Handbook of biodegradable polymers*. iSmithers Rapra Publishing.
- Begelman, G., Pechuk, M., Rivlin, E., & Sabo, E. (2006, January). System for computer-aided multiresolution microscopic pathology diagnostics. In *Computer Vision Systems, 2006 ICVS'06. IEEE International Conference on* (pp. 16-16). IEEE.

Běhálek, L., Maršálková, M., Lenfeld, P., Habr, J., Bobek, J., & Seidl, M. (2014). Study of crystallization of polylactic acid composites and nanocomposites with natural fibres by DSC method. *NANOCON 2013*, 16-18.

Benhaj, K., Akcali, K. C., & Ozturk, M. (2006). Redundant expression of canonical Wnt ligands in human breast cancer cell lines. *Oncology reports*, 15(3), 701-707.

Ber, S., Köse, G. T., & Hasırcı, V. (2005). Bone tissue engineering on patterned collagen films: an in vitro study. *Biomaterials*, 26(14), 1977-1986.

Betancourt, T., & Brannon-Peppas, L. (2006). Micro-and nanofabrication methods in nanotechnological medical and pharmaceutical devices. *International journal of nanomedicine*, 1(4), 483.

Biela, S. A., Su, Y., Spatz, J. P., & Kemkemer, R. (2009). Different sensitivity of human endothelial cells, smooth muscle cells and fibroblasts to topography in the nano–micro range. *Acta Biomaterialia*, 5(7), 2460-2466.

Blodgett, O. W. (1966). Design of welded structures. *Cleveland: James F. Lincoln Arc Welding Foundation*, 1966, 1.

Broers, J. L., Machiels, B. M., Kuijpers, H. J., Smedts, F., van den Kieboom, R., Raymond, Y., & Ramaekers, F. C. (1997). A-and B-type lamins are differentially expressed in normal human tissues. *Histochemistry and cell biology*, 107(6), 505-517.

Broers, J. L., Peeters, E. A., Kuijpers, H. J., Endert, J., Bouten, C. V., Oomens, C. W., ... & Ramaekers, F. C. (2004). Decreased mechanical stiffness in LMNA–/– cells is caused by defective nucleo-cytoskeletal integrity: implications for the development of laminopathies. *Human molecular genetics*, 13(21), 2567-2580.

Brozovic, A., Duran, G. E., Wang, Y. C., Francisco, E. B., & Sikic, B. I. (2015). The miR-200 family differentially regulates sensitivity to paclitaxel and carboplatin in human ovarian carcinoma OVCAR-3 and MES-OV cells. *Molecular oncology*, 9(8), 1678-1693.

Carman, C. V., & Springer, T. A. (2003). Integrin avidity regulation: are changes in affinity and conformation underemphasized?. *Current opinion in cell biology*, 15(5), 547-556.

Cassie, A. B. D., & Baxter, S. (1944). Wettability of porous surfaces. *Transactions of the Faraday Society*, 40, 546-551.

Chang, J., Arbeláez, P., Switz, N., Reber, C., Tapley, A., Davis, J. L., ... & Malik, J. (2012). *Automated tuberculosis diagnosis using fluorescence images from a mobile microscope* (pp. 345-352). Springer Berlin Heidelberg.

Charest, J. L., García, A. J., & King, W. P. (2007). Myoblast alignment and differentiation on cell culture substrates with microscale topography and model chemistries. *Biomaterials*, 28(13), 2202-2210.

Chen, C. C., Chueh, J. Y., Huang, H. M., & Lee, S. Y. (2003). Preparation and characterization of biodegradable PLA polymeric blends. *Biomaterials*, 24(7), 1167-1173.

Chen, C. S. (2008). Mechanotransduction—a field pulling together?. *Journal of cell science*, 121(20), 3285-3292.

Chen, C. S., Mrksich, M., Huang, S., Whitesides, G. M., & Ingber, D. E. (1997). Geometric control of cell life and death. *Science*, 276(5317), 1425-1428.

Chivukula, M., Saad, R. S., Elishaev, E., White, S., Mauser, N., & Dabbs, D. J. (2007). Introduction of the Thin Prep Imaging System™(TIS): experience in a high volume academic practice. *Cytojournal*, 4(1), 6.

Dalby, M. J., Gadegaard, N., Tare, R., Andar, A., Riehle, M. O., Herzyk, P., ... & Oreffo, R. O. (2007). The control of human mesenchymal cell differentiation using nanoscale symmetry and disorder. *Nature materials*, 6(12), 997-1003.

Daniels, A. U., Chang, M. K., Andriano, K. P., & Heller, J. (1990). Mechanical properties of biodegradable polymers and composites proposed for internal fixation of bone. *Journal of Applied Biomaterials*, 1(1), 57-78.

Darling, E. M., Zauscher, S., Block, J. A., & Guilak, F. (2007). A thin-layer model for viscoelastic, stress-relaxation testing of cells using atomic force microscopy: do cell properties reflect metastatic potential?. *Biophysical journal*, 92(5), 1784-1791.

Davidson, P. M., Fromigué, O., Marie, P. J., Hasirci, V., Reiter, G., & Anselme, K. (2010). Topographically induced self-deformation of the nuclei of cells: dependence on cell type and proposed mechanisms. *Journal of Materials Science: Materials in Medicine*, 21(3), 939-946.

Davidson, P. M., Ozcelik, H., Hasirci, V., Reiter, G. & Anselme, K. Microstructured surfaces cause severe but non-detrimental deformation of the cell nucleus. *Adv. Mater.* **21**, 3586–3590 (2009).

Du, X., Yang, J., Yang, D., Tian, W., & Zhu, Z. (2014). The genetic basis for inactivation of Wnt pathway in human osteosarcoma. *BMC cancer*, 14(1), 1.

Edith, D., & Six, J. L. (2006). Surface characteristics of PLA and PLGA films. *Applied Surface Science*, 253(5), 2758-2764.

Eke, G., Goñi-de-Cerio, F., Suarez-Merino, B., Hasirci, N., & Hasirci, V. (2015). Biocompatibility of Dead Sea Water and retinyl palmitate carrying poly (3-hydroxybutyrate-co-3-hydroxyvalerate) micro/nanoparticles designed for transdermal skin therapy. *Journal of Bioactive and Compatible Polymers: Biomedical Applications*, 0883911515585183.

Etienne-Manneville, S., & Hall, A. (2001). Integrin-mediated activation of Cdc42 controls cell polarity in migrating astrocytes through PKC ζ . *Cell*, 106(4), 489-498.

Fink, J., Carpi, N., Betz, T., Bétard, A., Chebah, M., Azioune, A., ... & Piel, M. (2011). External forces control mitotic spindle positioning. *Nature cell biology*, 13(7), 771-778.

- Fletcher, D. A., & Mullins, R. D. (2010). Cell mechanics and the cytoskeleton. *Nature*, *463*(7280), 485-492.
- Folkman, J., & Moscona, A. (1978). Role of cell shape in growth control.
- Franco, D., Klingauf, M., Bednarzik, M., Cecchini, M., Kurtcuoglu, V., Gobrecht, J., ... & Ferrari, A. (2011). Control of initial endothelial spreading by topographic activation of focal adhesion kinase. *Soft Matter*, *7*(16), 7313-7324.
- Friedl, P., Wolf, K., & Lammerding, J. (2011). Nuclear mechanics during cell migration. *Current opinion in cell biology*, *23*(1), 55-64.
- Galbraith, C. G., Yamada, K. M., & Sheetz, M. P. (2002). The relationship between force and focal complex development. *The Journal of cell biology*, *159*(4), 695-705.
- Gartland, A., Buckley, K. A., Dillon, J. P., Curran, J. M., Hunt, J. A., & Gallagher, J. A. (2005). Isolation and culture of human osteoblasts. *Human Cell Culture Protocols*, 29-54.
- Gartner, L. P., & Hiatt, J. L. (2012). *Color atlas and text of histology*. Lippincott Williams & Wilkins.
- Gentile, P., Chiono, V., Carmagnola, I., & Hatton, P. V. (2014). An overview of poly (lactic-co-glycolic) acid (PLGA)-based biomaterials for bone tissue engineering. *International journal of molecular sciences*, *15*(3), 3640-3659.
- Goldman, R. D., Shumaker, D. K., Erdos, M. R., Eriksson, M., Goldman, A. E., Gordon, L. B., ... & Collins, F. S. (2004). Accumulation of mutant lamin A causes progressive changes in nuclear architecture in Hutchinson–Gilford progeria syndrome. *Proceedings of the National Academy of Sciences of the United States of America*, *101*(24), 8963-8968.
- Gomes, E. R., Jani, S., & Gundersen, G. G. (2005). Nuclear movement regulated by Cdc42, MRCK, myosin, and actin flow establishes MTOC polarization in migrating cells. *Cell*, *121*(3), 451-463.

Gossett DR, *et al.* Hydrodynamic stretching of single cells for large population mechanical phenotyping. *Proceedings of the National Academy of Sciences* **109**, 7630-7635 (2012).

Gruenbaum Y, Margalit A, Goldman RD, Shumaker DK, Wilson KL. The nuclear lamina comes of age. *Nature reviews Molecular cell biology* **6**, 21-31 (2005).

Gunatillake, P. A., & Adhikari, R. (2003). Biodegradable synthetic polymers for tissue engineering. *Eur Cell Mater*, 5(1), 1-16.

Han, S. J., Bielawski, K. S., Ting, L. H., Rodriguez, M. L., & Sniadecki, N. J. (2012). Decoupling substrate stiffness, spread area, and micropost density: a close spatial relationship between traction forces and focal adhesions. *Biophysical journal*, 103(4), 640-648.

Hasirci, V., & Kenar, H. (2006). Novel surface patterning approaches for tissue engineering and their effect on cell behavior.

Heydemann, A., & McNally, E. M. (2007). Consequences of disrupting the dystrophin-sarcoglycan complex in cardiac and skeletal myopathy. *Trends in cardiovascular medicine*, 17(2), 55-59.

Hong, T. F., Ju, W. J., Wu, M. C., Tai, C. H., Tsai, C. H., & Fu, L. M. (2010). Rapid prototyping of PMMA microfluidic chips utilizing a CO₂ laser. *Microfluidics and nanofluidics*, 9(6), 1125-1133.

Hutchison, C. J. (2002). Lamins: building blocks or regulators of gene expression?. *Nature Reviews Molecular Cell Biology*, 3(11), 848-858.

Hutchison, C. J., & Worman, H. J. (2004). A-type lamins: guardians of the soma?. *Nature Cell Biology*, 6(11), 1062-1067.

Jiang, W. G., Sanders, A. J., Katoh, M., Ungefroren, H., Gieseler, F., Prince, M., ... & Sliva, D. (2015, December). Tissue invasion and metastasis: molecular, biological

and clinical perspectives. In *Seminars in cancer biology*(Vol. 35, pp. S244-S275). Academic Press.

Jolliffe, I. T. *Principal Component Analysis 1–9* (Springer, New York, 2002).

Kamaly, N., Yameen, B., Wu, J., & Farokhzad, O. C. (2016). Degradable Controlled-Release Polymers and Polymeric Nanoparticles: Mechanisms of Controlling Drug Release. *Chemical reviews*, *116*(4), 2602-2663.

Karuri, N. W., Liliensiek, S., Teixeira, A. I., Abrams, G., Campbell, S., Nealey, P. F., & Murphy, C. J. (2004). Biological length scale topography enhances cell-substratum adhesion of human corneal epithelial cells. *Journal of cell science*, *117*(15), 3153-3164.

Karuri, N. W., Nealey, P. F., Murphy, C. J., & Albrecht, R. M. (2008). Structural organization of the cytoskeleton in SV40 human corneal epithelial cells cultured on nano-and microscale grooves. *Scanning*, *30*(5), 405-413.

Kitchener HC, *et al.* MAVARIC—a comparison of automation-assisted and manual cervical screening: a randomised controlled trial. *Clinical Governance: An International Journal* **16**, (2011).

Le Beyec, J., Xu, R., Lee, S. Y., Nelson, C. M., Rizki, A., Alcaraz, J., & Bissell, M. J. (2007). Cell shape regulates global histone acetylation in human mammary epithelial cells. *Experimental cell research*, *313*(14), 3066-3075.

Lee, J. S., Hale, C. M., Panorchan, P., Khatau, S. B., George, J. P., Tseng, Y., ... & Wirtz, D. (2007). Nuclear lamin A/C deficiency induces defects in cell mechanics, polarization, and migration. *Biophysical journal*, *93*(7), 2542-2552.

Li, J. M., Liu, C., Liu, J. S., Xu, Z., & Wang, L. D. (2009). Multi-layer PMMA microfluidic chips with channel networks for liquid sample operation. *Journal of Materials Processing Technology*, *209*(15), 5487-5493.

Li, N., Tourovskaia, A., & Folch, A. (2003). Biology on a chip: microfabrication for studying the behavior of cultured cells. *Critical Reviews™ in Biomedical Engineering*, 31(5&6).

Lim, H., & Hoag, S. W. (2013). Plasticizer Effects on Physical–Mechanical Properties of Solvent Cast Soluplus® Films. *Aaps Pharmscitech*, 14(3), 903-910.

Liu, H., Wang, S., & Qi, N. (2012). Controllable structure, properties, and degradation of the electrospun PLGA/PLA-blended nanofibrous scaffolds. *Journal of Applied Polymer Science*, 125(S2).

Lourenço, B. D. N. (2011). Cells behavior on superhydrophobic surfaces with different topographies.

Lu, L., Garcia, C. A., & Mikos, A. G. (1999). In vitro degradation of thin poly (DL-lactic-co-glycolic acid) films. *Journal of biomedical materials research*, 46(2), 236-244.

Lu, X., & Leng, Y. (2009). Comparison of the osteoblast and myoblast behavior on hydroxyapatite microgrooves. *Journal of Biomedical Materials Research Part B: Applied Biomaterials*, 90(1), 438-445.

Ma, Z., Gao, C., Yuan, J., Ji, J., Gong, Y., & Shen, J. (2002). Surface modification of poly-L-lactide by photografting of hydrophilic polymers towards improving its hydrophilicity. *Journal of applied polymer science*, 85(10), 2163-2171.

Makadia, H. K., & Siegel, S. J. (2011). Poly lactic-co-glycolic acid (PLGA) as biodegradable controlled drug delivery carrier. *Polymers*, 3(3), 1377-1397.

McManus, L. L., Bonnier, F., Burke, G. A., Meenan, B. J., Boyd, A. R., & Byrne, H. J. (2012). Assessment of an osteoblast-like cell line as a model for human primary osteoblasts using Raman spectroscopy. *Analyst*, 137(7), 1559-1569.

- Mendez, M. G., Kojima, S. I., & Goldman, R. D. (2010). Vimentin induces changes in cell shape, motility, and adhesion during the epithelial to mesenchymal transition. *The FASEB Journal*, 24(6), 1838-1851.
- Meyer, F. (1994). Topographic distance and watershed lines. *Signal processing*, 38(1), 113-125.
- Mitra, S. K., Hanson, D. A., & Schlaepfer, D. D. (2005). Focal adhesion kinase: in command and control of cell motility. *Nature Reviews Molecular Cell Biology*, 6(1), 56-68.
- Na, S., Collin, O., Chowdhury, F., Tay, B., Ouyang, M., Wang, Y., & Wang, N. (2008). Rapid signal transduction in living cells is a unique feature of mechanotransduction. *Proceedings of the National Academy of Sciences*, 105(18), 6626-6631.
- Nam, E. H., Lee, Y., Park, Y. K., Lee, J. W., & Kim, S. (2012). ZEB2 upregulates integrin $\alpha 5$ expression through cooperation with Sp1 to induce invasion during epithelial–mesenchymal transition of human cancer cells. *Carcinogenesis*, bgs005.
- Navarro, M., Michiardi, A., Castano, O., & Planell, J. A. (2008). Biomaterials in orthopaedics. *Journal of the Royal Society Interface*, 5(27), 1137-1158.
- Nelson, W. J. (2009). Remodeling epithelial cell organization: transitions between front–rear and apical–basal polarity. *Cold Spring Harbor perspectives in biology*, 1(1), a000513.
- Nemir, S., & West, J. L. (2010). Synthetic materials in the study of cell response to substrate rigidity. *Annals of biomedical engineering*, 38(1), 2-20.
- Nickerson, J. A., Blencowe, B. J., & Penman, S. (1996). The architectural organization of nuclear metabolism. *International review of cytology*, 162, 67-123.)
- Niini, T., & Knuutila, S. (2014). Cytogenetic and molecular genetic alterations in bone tumors. *Bone Cancer: Primary Bone Cancers and Bone Metastases*, 319.

Noboyuki, O. (1979). A Threshold Selection Method from gray Level histogram. *IEEE Transmission on System, MAN Cybernetics*, 9(1).

Okada M. *Chemical syntheses of biodegradable polymers*, Prog. Polym. Sci 2002; 27: 87-133.

Ozcelik, H. (2012). Interaction between micro and nano patterned polymeric surfaces and different cell types (Doctoral dissertation, Middle East Technical University).

Özçelik, H., Padeste, C., & Hasirci, V. (2014). Systematically organized nanopillar arrays reveal differences in adhesion and alignment properties of BMSC and Saos-2 cells. *Colloids and Surfaces B: Biointerfaces*, 119, 71-81.

Pachenari M, *et al.* Mechanical properties of cancer cytoskeleton depend on actin filaments to microtubules content: Investigating different grades of colon cancer cell lines. *Journal of biomechanics* 47, 373-379 (2014).

Pan, Z., Yan, C., Peng, R., Zhao, Y., He, Y., & Ding, J. (2012). Control of cell nucleus shapes via micropillar patterns. *Biomaterials*, 33(6), 1730-1735.

Parsons, S. J., & Parsons, J. T. (2004). Src family kinases, key regulators of signal transduction. *Oncogene*, 23(48), 7906-7909.

PaszeK, M. J., Zahir, N., Johnson, K. R., Lakins, J. N., Rozenberg, G. I., Gefen, A., ... & Weaver, V. M. (2005). Tensional homeostasis and the malignant phenotype. *Cancer cell*, 8(3), 241-254.

Pollard, T. D. (2003). The cytoskeleton, cellular motility and the reductionist agenda. *Nature*, 422(6933), 741-745.

Prokocimer, M., Davidovich, M., Nissim-Rafinia, M., Wiesel-Motiuk, N., Bar, D. Z., Barkan, R., ... & Gruenbaum, Y. (2009). Nuclear lamins: key regulators of nuclear structure and activities. *Journal of cellular and molecular medicine*, 13(6), 1059-1085.

Rajniecek, A., Britland, S., & McCaig, C. (1997). Contact guidance of CNS neurites on grooved quartz: influence of groove dimensions, neuronal age and cell type. *Journal of Cell Science*, 110(23), 2905-2913.

Rickard, D. J., Kassem, M., Hefferan, T. E., Sarkar, G., Spelsberg, T. C., & Riggs, B. L. (1996). Isolation and characterization of osteoblast precursor cells from human bone marrow. *Journal of Bone and Mineral Research*, 11(3), 312-324.

Rizvi, I., Gurkan, U. A., Tasoglu, S., Alagic, N., Celli, J. P., Mensah, L. B., ... & Hasan, T. (2013). Flow induces epithelial-mesenchymal transition, cellular heterogeneity and biomarker modulation in 3D ovarian cancer nodules. *Proceedings of the National Academy of Sciences*, 110(22), E1974-E1983.

Rosin, P. L. (2003). Measuring shape: ellipticity, rectangularity, and triangularity. *Machine Vision and Applications*, 14(3), 172-184.

Roskoski Jr, R. (2012). ERK1/2 MAP kinases: structure, function, and regulation. *Pharmacological research*, 66(2), 105-143.

Salamone, J. C. (Ed.). (1998). *Concise polymeric materials encyclopedia* (Vol. 1). CRC press.

Samatov, T. R., Tonevitsky, A. G., & Schumacher, U. (2013). Epithelial-mesenchymal transition: focus on metastatic cascade, alternative splicing, non-coding RNAs and modulating compounds. *Molecular cancer*, 12(1), 1.

Schlaepfer, D. D., Hauck, C. R., & Sieg, D. J. (1999). Signaling through focal adhesion kinase. *Progress in biophysics and molecular biology*, 71(3), 435-478.

Schnitt SJ, *et al.* Interobserver reproducibility in the diagnosis of ductal proliferative breast lesions using standardized criteria. *The American journal of surgical pathology* **16**, 1133-1143 (1992).

Schoen, I., Hu, W., Klotzsch, E., & Vogel, V. (2010). Probing cellular traction forces by micropillar arrays: contribution of substrate warping to pillar deflection. *Nano letters*, *10*(5), 1823-1830.

Schwartz, M. A., Schaller, M. D., & Ginsberg, M. H. (1995). Integrins: emerging paradigms of signal transduction. *Annual review of cell and developmental biology*, *11*(1), 549-599.

Sniadecki, N. J., & Chen, C. S. (2007). Microfabricated silicone elastomeric post arrays for measuring traction forces of adherent cells. *Methods in cell biology*, *83*, 313-328.

Soriano, P., Montgomery, C., Geske, R., & Bradley, A. (1991). Targeted disruption of the c-src proto-oncogene leads to osteopetrosis in mice. *Cell*, *64*(4), 693-702.

Starr, D. A., & Fridolfsson, H. N. (2010). Interactions between nuclei and the cytoskeleton are mediated by SUN-KASH nuclear-envelope bridges. *Annual review of cell and developmental biology*, *26*, 421-444.

Stein, G. S., Lian, J. B., Van Wijnen, A. J., Stein, J. L., Javed, A., Montecino, M., ... & Young, D. (2007). Organization of transcriptional regulatory machinery in nuclear microenvironments: implications for biological control and cancer. *Advances in enzyme regulation*, *47*, 242.

Swaminathan, V., Mythreye, K., O'Brien, E. T., Berchuck, A., Blobe, G. C., & Superfine, R. (2011). Mechanical stiffness grades metastatic potential in patient tumor cells and in cancer cell lines. *Cancer research*, *71*(15), 5075-5080.

Tapley, E. C., & Starr, D. A. (2013). Connecting the nucleus to the cytoskeleton by SUN-KASH bridges across the nuclear envelope. *Current opinion in cell biology*, *25*(1), 57-62.

Théry, M. (2010). Micropatterning as a tool to decipher cell morphogenesis and functions. *Journal of cell science*, *123*(24), 4201-4213.

Théry, M., Racine, V., Pépin, A., Piel, M., Chen, Y., Sibarita, J. B., & Bornens, M. (2005). The extracellular matrix guides the orientation of the cell division axis. *Nature cell biology*, 7(10), 947-953.

Thompson, E. W., Paik, S., Brünner, N., Sommers, C. L., Zugmaier, G., Clarke, R., ... & Martin, G. R. (1992). Association of increased basement membrane invasiveness with absence of estrogen receptor and expression of vimentin in human breast cancer cell lines. *Journal of cellular physiology*, 150(3), 534-544.

Timoshenko, S. P. (1921). On the correction factor for shear of the differential equation for transverse vibrations of prismatic bar. *Philosophical Magazine*, 6(41), 295.

Vergani, L., Grattarola, M., & Nicolini, C. (2004). Modifications of chromatin structure and gene expression following induced alterations of cellular shape. *The international journal of biochemistry & cell biology*, 36(8), 1447-1461.

Versaevel, M., Grevesse, T., & Gabriele, S. (2012). Spatial coordination between cell and nuclear shape within micropatterned endothelial cells. *Nature communications*, 3, 671.

Vicente-Manzanares, M., Ma, X., Adelstein, R. S., & Horwitz, A. R. (2009). Non-muscle myosin II takes centre stage in cell adhesion and migration. *Nature reviews Molecular cell biology*, 10(11), 778-790

Vroman I, Tighzert L. *Biodegradable polymers*, Materials 2009; 2: 307-334.

Wang, N., Tytell, J. D., & Ingber, D. E. (2009). Mechanotransduction at a distance: mechanically coupling the extracellular matrix with the nucleus. *Nature reviews Molecular cell biology*, 10(1), 75-82.)

Wenzel, R. N. (1936). Resistance of solid surfaces to wetting by water. *Industrial & Engineering Chemistry*, 28(8), 988-994.

Wilbur DC, *et al.* The Becton Dickinson FocalPoint GS Imaging System clinical trials demonstrate significantly improved sensitivity for the detection of important cervical lesions. *American journal of clinical pathology* **132**, 767-775 (2009).

Wirtz, D., Konstantopoulos, K., & Searson, P. C. (2011). The physics of cancer: the role of physical interactions and mechanical forces in metastasis. *Nature Reviews Cancer*, 11(7), 512-522.

Wong, T. S., & Ho, C. M. (2009). Dependence of macroscopic wetting on nanoscopic surface textures. *Langmuir*, 25(22), 12851-12854.

Wozniak, M. A., Modzelewska, K., Kwong, L., & Keely, P. J. (2004). Focal adhesion regulation of cell behavior. *Biochimica et Biophysica Acta (BBA)-Molecular Cell Research*, 1692(2), 103-119.

Wu, Z., Wu, L., Weng, D., Xu, D., Geng, J., & Zhao, F. (2009). Reduced expression of lamin A/C correlates with poor histological differentiation and prognosis in primary gastric carcinoma. *Journal of Experimental & Clinical Cancer Research*, 28(1), 1-12.

Yang L, *et al.* Pathminer: A web-based tool for computer-assisted diagnostics in pathology. *Information Technology in Biomedicine, IEEE Transactions on* **13**, 291-299 (2009).

Yang, M., Kpalma, K., & Ronsin, J. (2008). A survey of shape feature extraction techniques. *Pattern recognition*, 43-90.

Yuzugullu, H., Benhaj, K., Ozturk, N., Senturk, S., Celik, E., Toyly, A., ... & Atabey, N. (2009). Canonical Wnt signaling is antagonized by noncanonical Wnt5a in hepatocellular carcinoma cells. *Molecular cancer*, 8(1), 1.

Zhai, W., Ko, Y., Zhu, W., Wong, A., & Park, C. B. (2009). A study of the crystallization, melting, and foaming behaviors of polylactic acid in compressed CO₂. *International journal of molecular sciences*, 10(12), 5381-5397.

Zhang, D., & Lu, G. (2004). Review of shape representation and description techniques. *Pattern recognition*, 37(1), 1-19.

Zhang, L. P., Li, W. J., Zhu, Y. F., Huang, S. Y., Fang, S. Y., Shen, L., & Gao, Y. L. (2015). CDKN3 knockdown reduces cell proliferation, invasion and promotes apoptosis in human ovarian cancer. *International journal of clinical and experimental pathology*, 8(5), 4535.

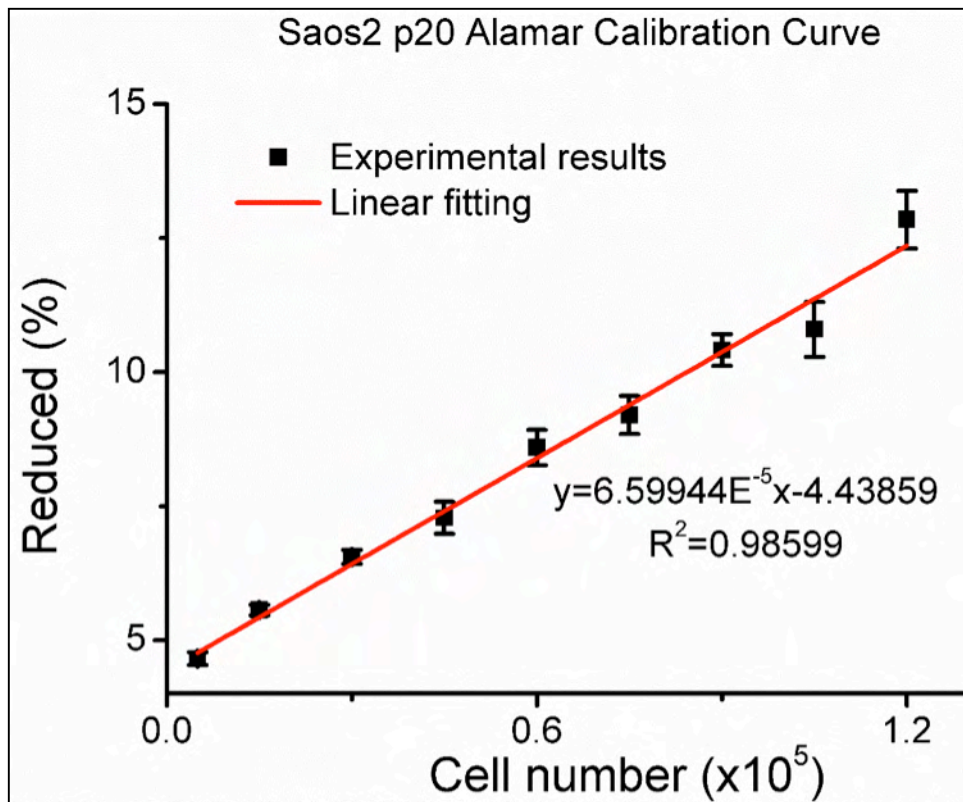
Zheng, Q., & Lü, C. (2014). Size effects of surface roughness to superhydrophobicity. *Procedia IUTAM*, 10, 462-475.

Zheng, Q., Lv, C., Hao, P., & Sheridan, J. (2010). Small is beautiful, and dry. *Science China Physics, Mechanics and Astronomy*, 53(12), 2245-2259.

Zorlutuna, P., Hasirci, N., & Hasirci, V. (2008). Nanopatterned collagen tubes for vascular tissue engineering. *Journal of tissue engineering and regenerative medicine*, 2(6), 373-377.

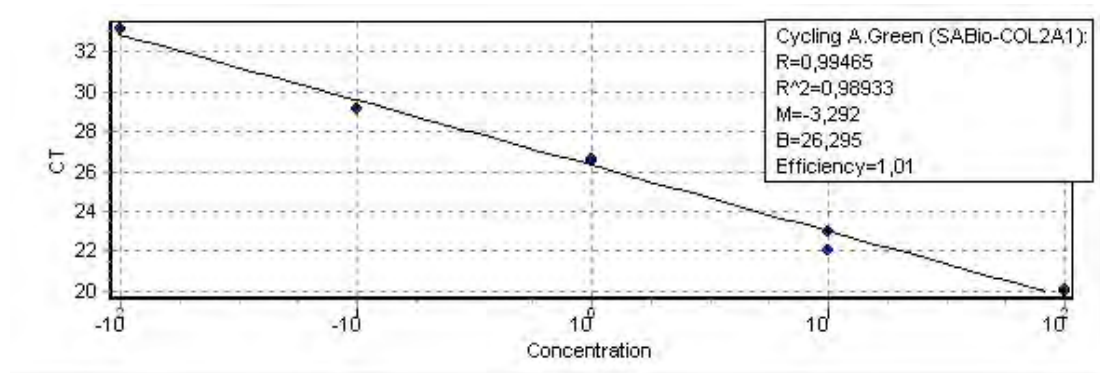
APPENDICES

APPENDIX A

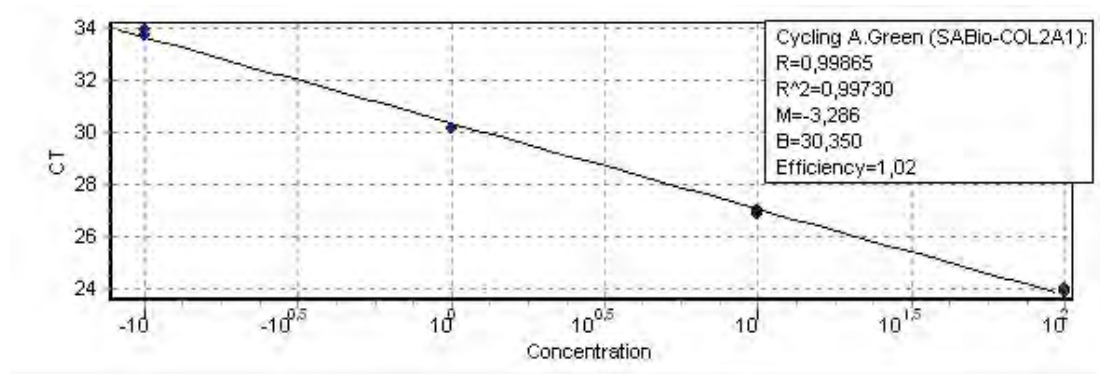


Appendix A: Calibration curve of Saos-2 cells for Alamar Blue proliferation assay.

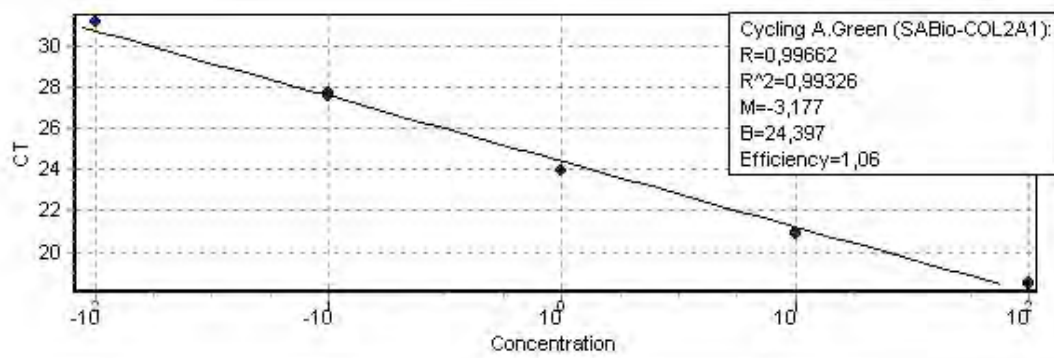
APPENDIX B



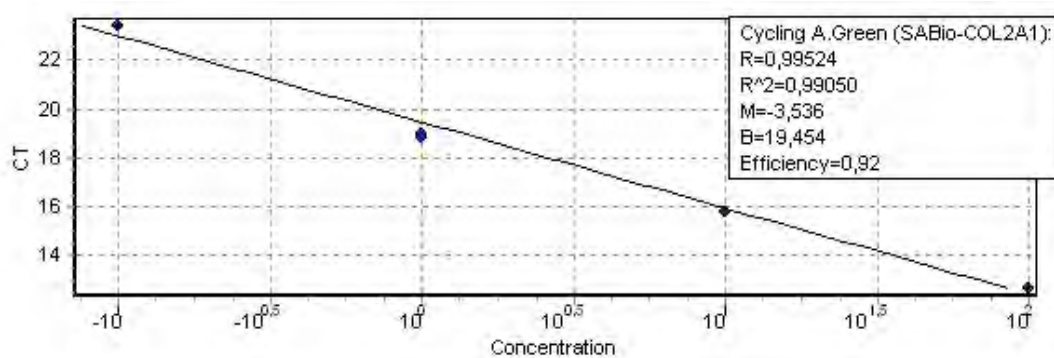
Appendix B1: Calibration curve of Cyclin A primer.



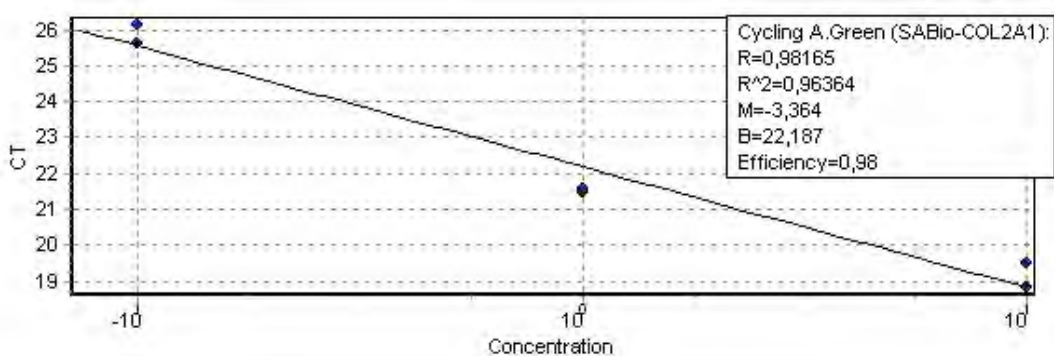
Appendix B2: Calibration curve of Cyclin B primer.



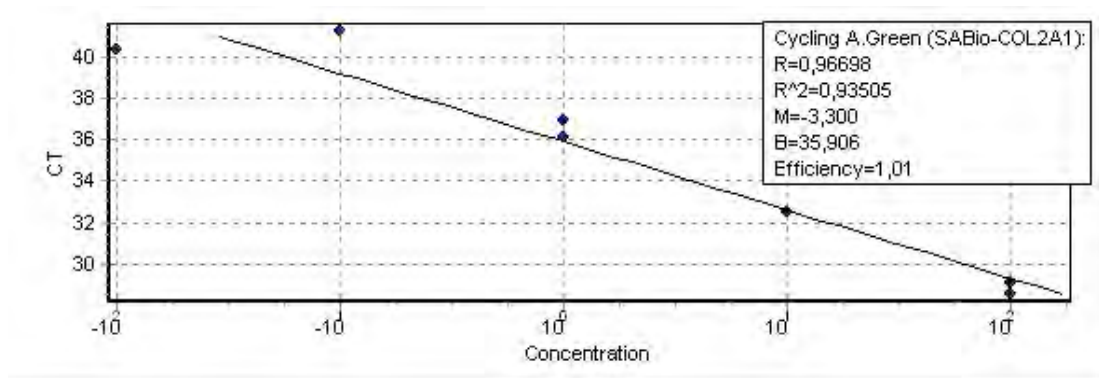
Appendix B3: Calibration curve of E-cadherin primer.



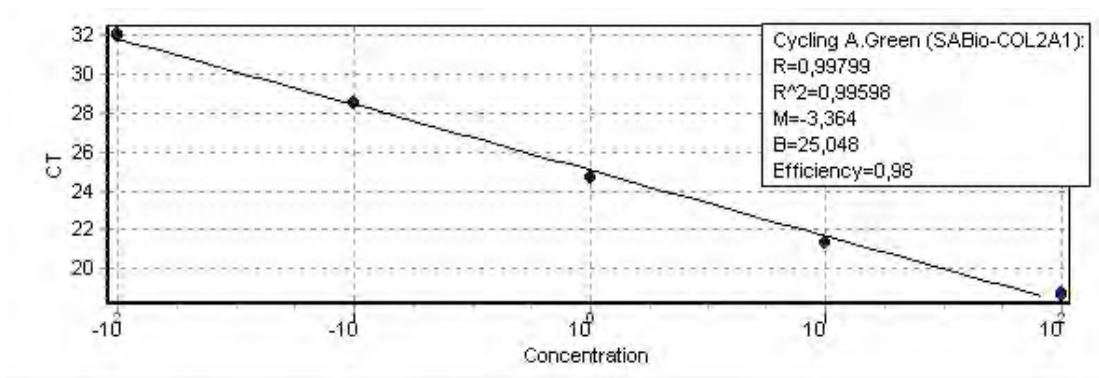
Appendix B4: Calibration curve of GAPDH primer.



Appendix B5: Calibration curve of Ki-67 primer.



Appendix B6: Calibration curve of p21 primer.



Appendix B7: Calibration curve of Vimentin primer.

APPENDIX C

Gene list of the human focal adhesion PCR array.

Position	Unigene	GeneBank	Symbol	Description	Gene Name
A01	Hs.235750	NM_001102	ACTN1	Actinin, alpha 1	BDPLT15
A02	Hs.498178	NM_001103	ACTN2	Actinin, alpha 2	CMD1AA, CMH23
A03	Hs.270291	NM_004924	ACTN4	Actinin, alpha 4	ACTININ-4, FSGS, FSGS1
A04	Hs.525622	NM_005163	AKT1	V-akt murine thymoma viral oncogene homolog 1	AKT, CWS6, PKB, PKB-ALPHA, PRKBA, RAC, RAC-ALPHA
A05	Hs.631535	NM_001626	AKT2	V-akt murine thymoma viral oncogene homolog 2	HIHGHH, PKBB, PKBBETA, PRKBB, RAC-BETA
A06	Hs.498292	NM_005465	AKT3	V-akt murine thymoma viral oncogene homolog 3 (protein kinase B, gamma)	MPPH, MPPH2, PKB-GAMMA, PKBG, PRKBG, RAC-PK-gamma, RAC-gamma, STK-2
A07	Hs.592313	NM_001173	ARHGAP5	Rho GTPase activating protein 5	GFI2, RhoGAP5, p190-B, p190BRhoGAP
A08	Hs.479747	NM_014567	BCAR1	Breast cancer anti-estrogen resistance 1	CAS, CAS1, CASS1, CRKAS, P130Cas
A09	Hs.350899	NM_001748	CAPN2	Calpain 2, (m/II) large subunit	CANP2, CANPL2, CANPml, mCANP
A10	Hs.74034	NM_001753	CAV1	Caveolin 1, caveolae protein, 22kDa	BSCL3, CGL3, LCCNS, MSTP085, PPH3, VIP21

A11	Hs.212332	NM_001233	CAV2	Caveolin 2	CAV
A12	Hs.98303	NM_001234	CAV3	Caveolin 3	LGMD1C, LQT9, VIP-21, VIP21
B01	Hs.467637	NM_001791	CDC42	Cell division cycle 42 (GTP binding protein, 25kDa)	CDC42Hs, G25K
B02	Hs.461896	NM_016823	CRK	V-crk sarcoma virus CT10 oncogene homolog (avian)	CRKII, p38
B03	Hs.5613	NM_005207	CRKL	V-crk sarcoma virus CT10 oncogene homolog (avian)-like	-
B04	Hs.712929	NM_001904	CTNNB1	Catenin (cadherin-associated protein), beta 1, 88kDa	CTNNB, MRD19, armadillo
B05	Hs.529451	NM_005219	DIAPH1	Diaphanous homolog 1 (Drosophila)	DFNA1, DIA1, DRF1, LFHL1, hDIA1
B06	Hs.159195	NM_001380	DOCK1	Dedicator of cytokinesis 1	DOCK180, ced5
B07	Hs.669931	NM_015548	DST	Dystonin	BP240, BPA, BPAG1, CATX-15, CATX15, D6S1101, DMH, DT, EBSB2, HSAN6, MACF2
B08	Hs.195464	NM_001456	FLNA	Filamin A, alpha	ABP-280, ABPX, CSBS, CVD1, FLN, FLN-A, FLN1, FMD, MNS, NHBP, OPD, OPD1, OPD2, XLVD, XMVD
B09	Hs.476448	NM_001457	FLNB	Filamin B, beta	ABP-278, ABP-280, AOI, FH1, FLN-B, FLN1L, LRS1, SCT, TABP, TAP
B10	Hs.390567	NM_002037	FYN	FYN oncogene related to SRC, FGR, YES	SLK, SYN, p59-FYN
B11	Hs.444356	NM_002086	GRB2	Growth factor receptor-bound protein 2	ASH, EGFRBP-GRB2, Grb3-3, MST084, MSTP084, NCKAP2
B12	Hs.445733	NM_002093	GSK3B	Glycogen synthase kinase 3 beta	-

C01	Hs.37003	NM_005343	HRAS	V-Ha-ras Harvey rat sarcoma viral oncogene homolog	C-BAS, HAS, C-H-RAS, C-HA-RAS1, CTLO, H-RASIDX, HAMSIV, HRAS1, RASH1, p21ras
C02	Hs.706355	NM_004517	ILK	Integrin-linked kinase	HEL-S-28, ILK-1, ILK-2, P59, p59ILK
C03	Hs.644352	NM_181501	ITGA1	Integrin, alpha 1	CD49a, VLA1
C04	Hs.436416	NM_001004439	ITGA11	Integrin, alpha 11	HsT18964
C05	Hs.482077	NM_002203	ITGA2	Integrin, alpha 2 (CD49B, alpha 2 subunit of VLA-2 receptor)	BR, CD49B, GPIa, HPA-5, VLA-2, VLAA2
C06	Hs.411312	NM_000419	ITGA2B	Integrin, alpha 2b (platelet glycoprotein IIb of IIb/IIIa complex, antigen CD41)	BDPLT16, BDPLT2, CD41, CD41B, GP2B, GPIIb, GT, GTA, HPA3, PPP1R93
C07	Hs.265829	NM_002204	ITGA3	Integrin, alpha 3 (antigen CD49C, alpha 3 subunit of VLA-3 receptor)	CD49C, GAP-B3, GAPB3, ILNEB, MSK18, VCA-2, VL3A, VLA3a
C08	Hs.440955	NM_000885	ITGA4	Integrin, alpha 4 (antigen CD49D, alpha 4 subunit of VLA-4 receptor)	CD49D, IA4
C09	Hs.505654	NM_002205	ITGA5	Integrin, alpha 5 (fibronectin receptor, alpha polypeptide)	CD49e, FNRA, VLA-5, VLA5A
C10	Hs.133397	NM_000210	ITGA6	Integrin, alpha 6	CD49f, ITGA6B, VLA-6
C11	Hs.524484	NM_002206	ITGA7	Integrin, alpha 7	-
C12	Hs.592472	NM_003638	ITGA8	Integrin, alpha 8	-
D01	Hs.113157	NM_002207	ITGA9	Integrin, alpha 9	ALPHA-RLC, ITGA4L, RLC
D02	Hs.174103	NM_002209	ITGAL	Integrin, alpha L (antigen CD11A (p180), lymphocyte function-associated antigen 1; alpha polypeptide)	CD11A, LFA-1, LFA1A
D03	Hs.172631	NM_000632	ITGAM	Integrin, alpha M (complement component 3	CD11B, CR3A, MAC-1, MAC1A, MO1A,

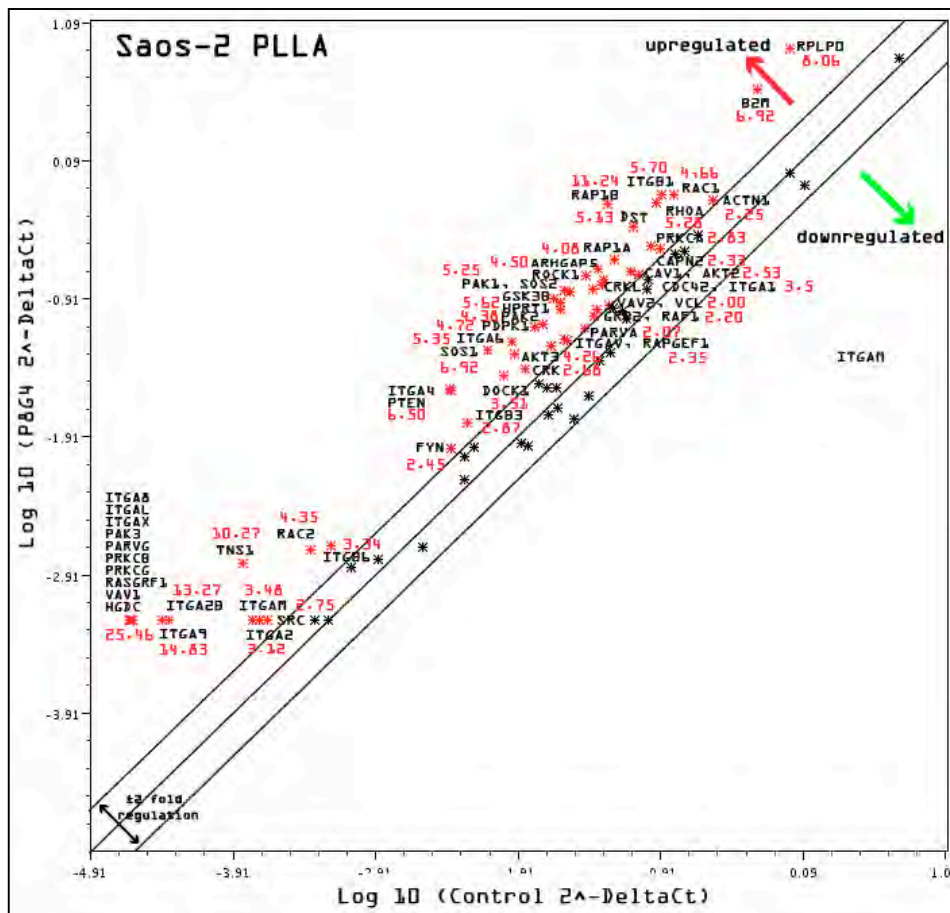
				receptor 3 subunit)	SLEB6
D04	Hs.436873	NM_002210	ITGAV	Integrin, alpha V (vitronectin receptor, alpha polypeptide, antigen CD51)	CD51, MSK8, VNRA, VTNR
D05	Hs.248472	NM_000887	ITGAX	Integrin, alpha X (complement component 3 receptor 4 subunit)	CD11C, SLEB6
D06	Hs.643813	NM_002211	ITGB1	Integrin, beta 1 (fibronectin receptor, beta polypeptide, antigen CD29 includes MDF2, MSK12)	CD29, FNRB, GPIIA, MDF2, MSK12, VLA-BETA, VLAB
D07	Hs.375957	NM_000211	ITGB2	Integrin, beta 2 (complement component 3 receptor 3 and 4 subunit)	CD18, LAD, LCAMB, LFA-1, MAC-1, MF17, MFI7
D08	Hs.218040	NM_000212	ITGB3	Integrin, beta 3 (platelet glycoprotein IIIa, antigen CD61)	BDPLT16, BDPLT2, CD61, GP3A, GPIIIa, GT
D09	Hs.632226	NM_000213	ITGB4	Integrin, beta 4	CD104
D10	Hs.13155	NM_002213	ITGB5	Integrin, beta 5	-
D11	Hs.470399	NM_000888	ITGB6	Integrin, beta 6	AI1H
D12	Hs.435714	NM_002576	PAK1	P21 protein (Cdc42/Rac)-activated kinase 1	PAKalpha
E01	Hs.518530	NM_002577	PAK2	P21 protein (Cdc42/Rac)-activated kinase 2	PAK65, PAKgamma
E02	Hs.656789	NM_002578	PAK3	P21 protein (Cdc42/Rac)-activated kinase 3	MRX30, MRX47, OPHN3, PAK-3, PAK3beta, bPAK, beta-PAK
E03	Hs.20447	NM_005884	PAK4	P21 protein (Cdc42/Rac)-activated kinase 4	-
E04	Hs.432914	NM_018222	PARVA	Parvin, alpha	CH-ILKBP, MXRA2
E05	Hs.475074	NM_013327	PARVB	Parvin, beta	CGI-56
E06	Hs.658995	NM_022141	PARVG	Parvin, gamma	-
E07	Hs.459691	NM_002613	PDPK1	3-phosphoinositide dependent protein kinase-1	PDK1, PDPK2, PDPK2P, PRO0461

E08	Hs.282177	NM_012398	PIP5K1C	Phosphatidylinositol-4-phosphate 5-kinase, type I, gamma	LCCS3, PIP5K-GAMMA, PIP5K1-gamma, PIP5Kgamma
E09	Hs.434248	NM_000445	PLEC	Plectin	EBS1, EBSMD, EBSND, EBSO, EBSOG, EBSPA, HD1, LGMD2Q, PCN, PLEC1, PLEC1b, PLTN
E10	Hs.531704	NM_002737	PRKCA	Protein kinase C, alpha	AAG6, PKC-alpha, PKCA, PRKACA
E11	Hs.460355	NM_002738	PRKCB	Protein kinase C, beta	PKC-beta, PKCB, PRKCB1, PRKCB2
E12	Hs.631564	NM_002739	PRKCG	Protein kinase C, gamma	PKC-gamma, PKCC, PKCG, SCA14
F01	Hs.729457	NM_000314	PTEN	Phosphatase and tensin homolog	10q23del, BZS, CWS1, DEC, GLM2, MHAM, MMAC1, PTEN1, TEP1
F02	Hs.395482	NM_005607	PTK2	PTK2 protein tyrosine kinase 2	FADK, FAK, FAK1, FRNK, PPP1R71, p125FAK, pp125FAK
F03	Hs.446336	NM_002859	PXN	Paxillin	-
F04	Hs.413812	NM_006908	RAC1	Ras-related C3 botulinum toxin substrate 1 (rho family, small GTP binding protein Rac1)	MIG5, Rac-1, TC-25, p21-Rac1
F05	Hs.517601	NM_002872	RAC2	Ras-related C3 botulinum toxin substrate 2 (rho family, small GTP binding protein Rac2)	EN-7, Gx, HSPC022, p21-Rac2
F06	Hs.159130	NM_002880	RAF1	V-raf-1 murine leukemia viral oncogene homolog 1	CMD1NN, CRAF, NS5, Raf-1, c-Raf
F07	Hs.586618	NM_002884	RAP1A	RAP1A, member of RAS oncogene family	C21KG, G-22K, KREV-1, KREV1, RAP1, SMGP21
F08	Hs.369920	NM_015646	RAP1B	RAP1B, member of RAS oncogene family	K-REV, RAL1B
F09	Hs.127897	NM_005312	RAPGEF1	Rap guanine nucleotide exchange factor (GEF) 1	C3G, GRF2
F10	Hs.459035	NM_153815	RASGRF1	Ras protein-specific guanine nucleotide-releasing	CDC25, CDC25L, GNRP, GRF1, GRF55,

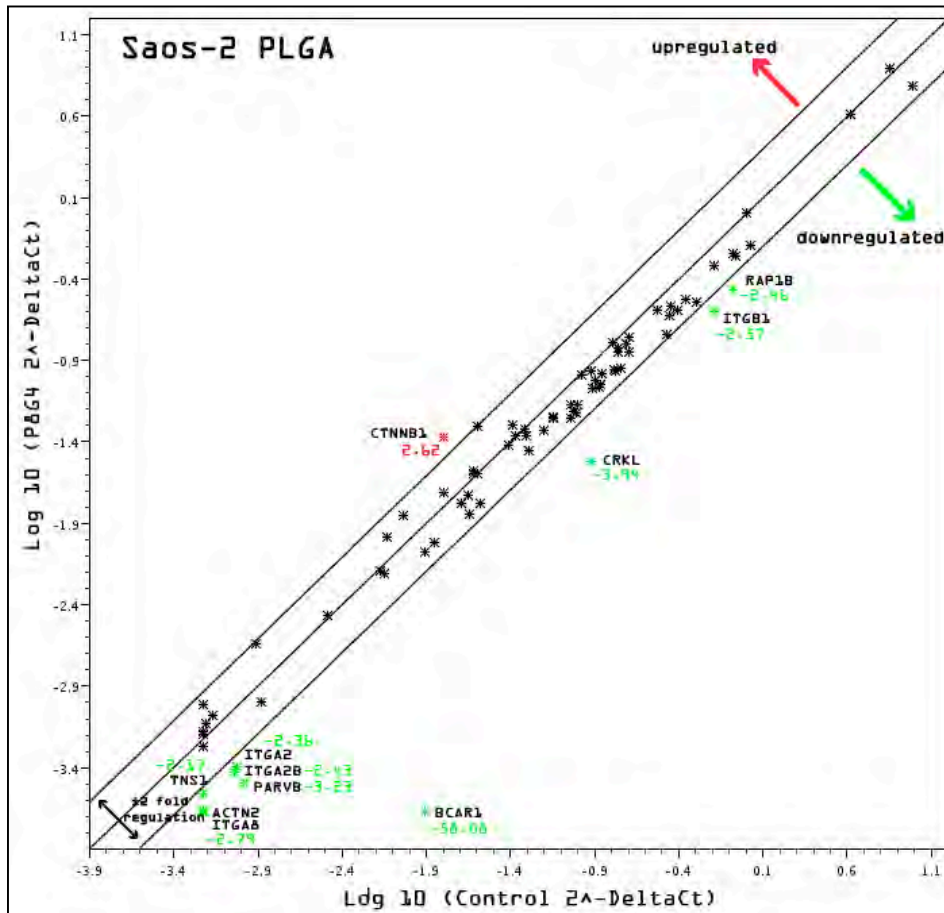
				factor 1	H-GRF55, PP13187, ras-GRF1
F11	Hs.247077	NM_001664	RHOA	Ras homolog gene family, member A	ARH12, ARHA, RHO12, RHOH12
F12	Hs.306307	NM_005406	ROCK1	Rho-associated, coiled-coil containing protein kinase 1	P160ROCK, ROCK-I
G01	Hs.681743	NM_004850	ROCK2	Rho-associated, coiled-coil containing protein kinase 2	ROCK-II
G02	Hs.433795	NM_003029	SHC1	SHC (Src homology 2 domain containing) transforming protein 1	SHC, SHCA
G03	Hs.709893	NM_005633	SOS1	Son of sevenless homolog 1 (Drosophila)	GF1, GGF1, GINGF, HGF, NS4
G04	Hs.291533	NM_006939	SOS2	Son of sevenless homolog 2 (Drosophila)	-
G05	Hs.195659	NM_005417	SRC	V-src sarcoma (Schmidt-Ruppin A-2) viral oncogene homolog (avian)	ASV, SRC1, c-SRC, p60-Src
G06	Hs.471014	NM_006289	TLN1	Talin 1	ILWEQ, TLN
G07	Hs.471381	NM_022648	TNS1	Tensin 1	MST091, MST122, MST127, MSTP091, MSTP122, MSTP127, MXRA6, PPP1R155, TNS
G08	Hs.515469	NM_003370	VASP	Vasodilator-stimulated phosphoprotein	-
G09	Hs.116237	NM_005428	VAV1	Vav 1 guanine nucleotide exchange factor	VAV
G10	Hs.369921	NM_003371	VAV2	Vav 2 guanine nucleotide exchange factor	VAV-2
G11	Hs.643896	NM_003373	VCL	Vinculin	CMD1W, CMH15, HEL114, MV, MVCL
G12	Hs.490415	NM_003461	ZYX	Zyxin	ESP-2, HED-2
H01	Hs.520640	NM_001101	ACTB	Actin, beta	BRWS1, PS1TP5BP1
H02	Hs.534255	NM_004048	B2M	Beta-2-microglobulin	-
H03	Hs.592355	NM_002046	GAPDH	Glyceraldehyde-3-phosphate dehydrogenase	G3PD, GAPD, HEL-S-162eP

H04	Hs.412707	NM_000194	HPRT1	Hypoxanthine phosphoribosyltransferase 1	HGPRT, HPRT
H05	Hs.546285	NM_001002	RPLP0	Ribosomal protein, large, P0	L10E, LP0, P0, PRLP0, RPP0
H06	N/A	SA_00105	HGDC	Human Genomic DNA Contamination	HIGX1A
H07	N/A	SA_00104	RTC	Reverse Transcription Control	RTC
H08	N/A	SA_00104	RTC	Reverse Transcription Control	RTC
H09	N/A	SA_00104	RTC	Reverse Transcription Control	RTC
H10	N/A	SA_00103	PPC	Positive PCR Control	PPC
H11	N/A	SA_00103	PPC	Positive PCR Control	PPC
H12	N/A	SA_00103	PPC	Positive PCR Control	PPC

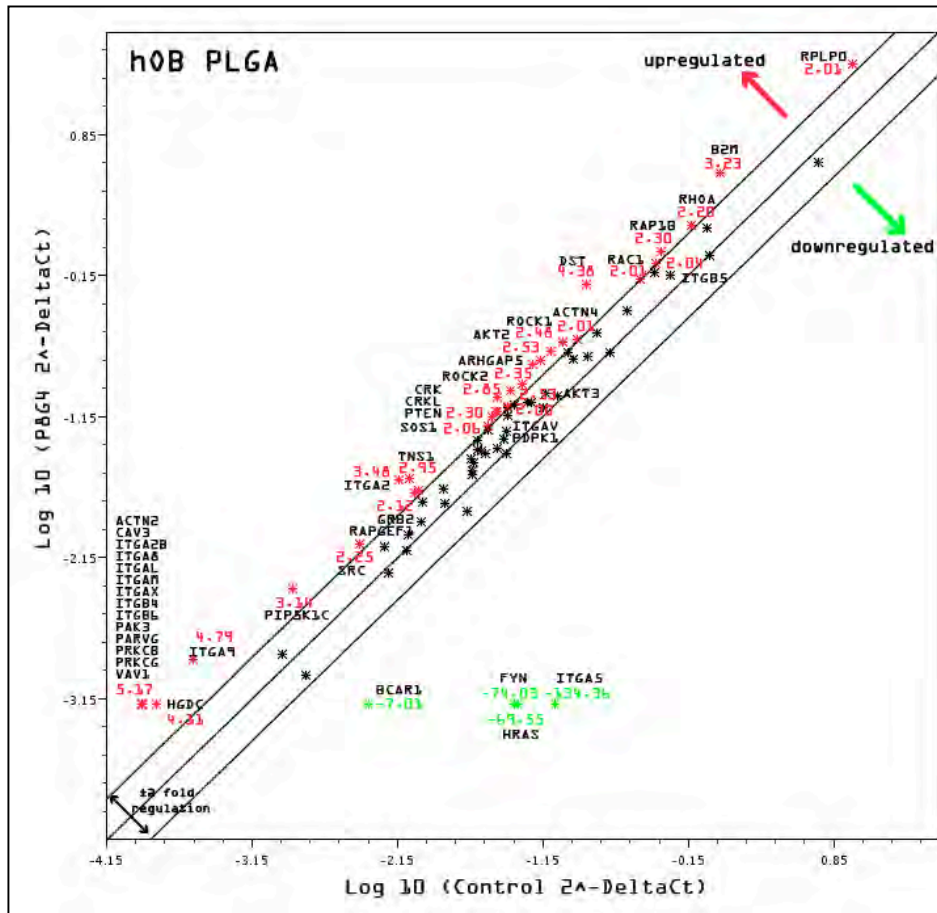
APPENDIX D



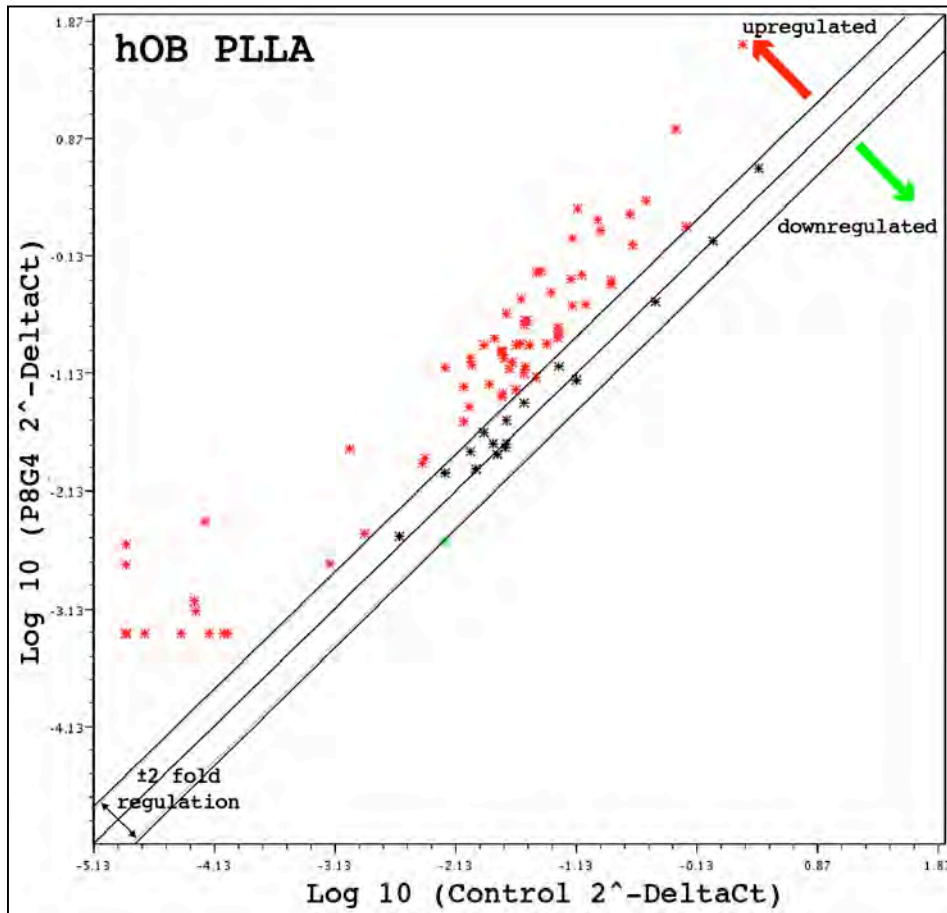
Appendix D1: Fold regulation scatter plot for Saos-2 cells cultured on PLLA (normalized to GAPDH, ± 2 fold change was accepted as no regulation, >2 fold regulation in $y > x$ region up regulation, >2 fold regulation in $x > y$ region down regulation).



Appendix D2: Fold regulation scatter plot for Saos-2 cells cultured on PLGA (normalized to GAPDH, ± 2 fold change was accepted as no regulation, >2 fold regulation in $y > x$ region up regulation, >2 fold regulation in $x > y$ region down regulation).

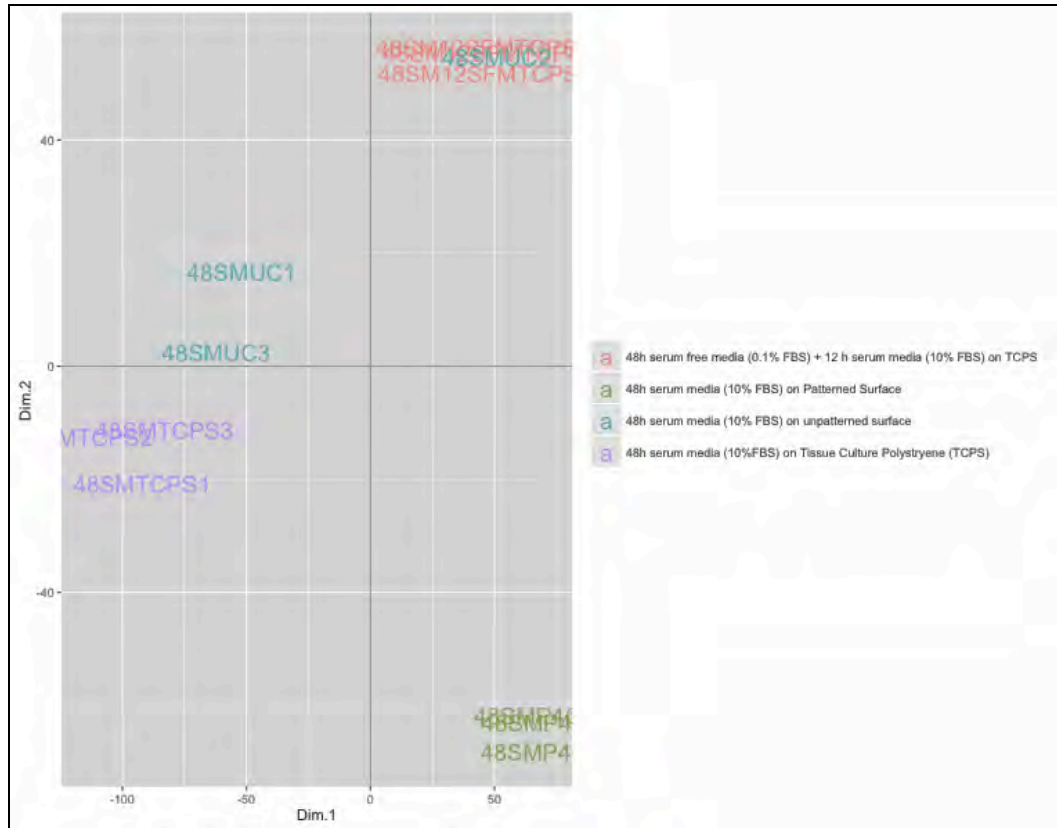


Appendix D3: Fold regulation scatter plot for hOB cells cultured on PLGA (normalized to GAPDH, ± 2 fold change was accepted as no regulation, >2 fold regulation in $y > x$ region upregulation, >2 fold regulation in $x > y$ region downregulation).

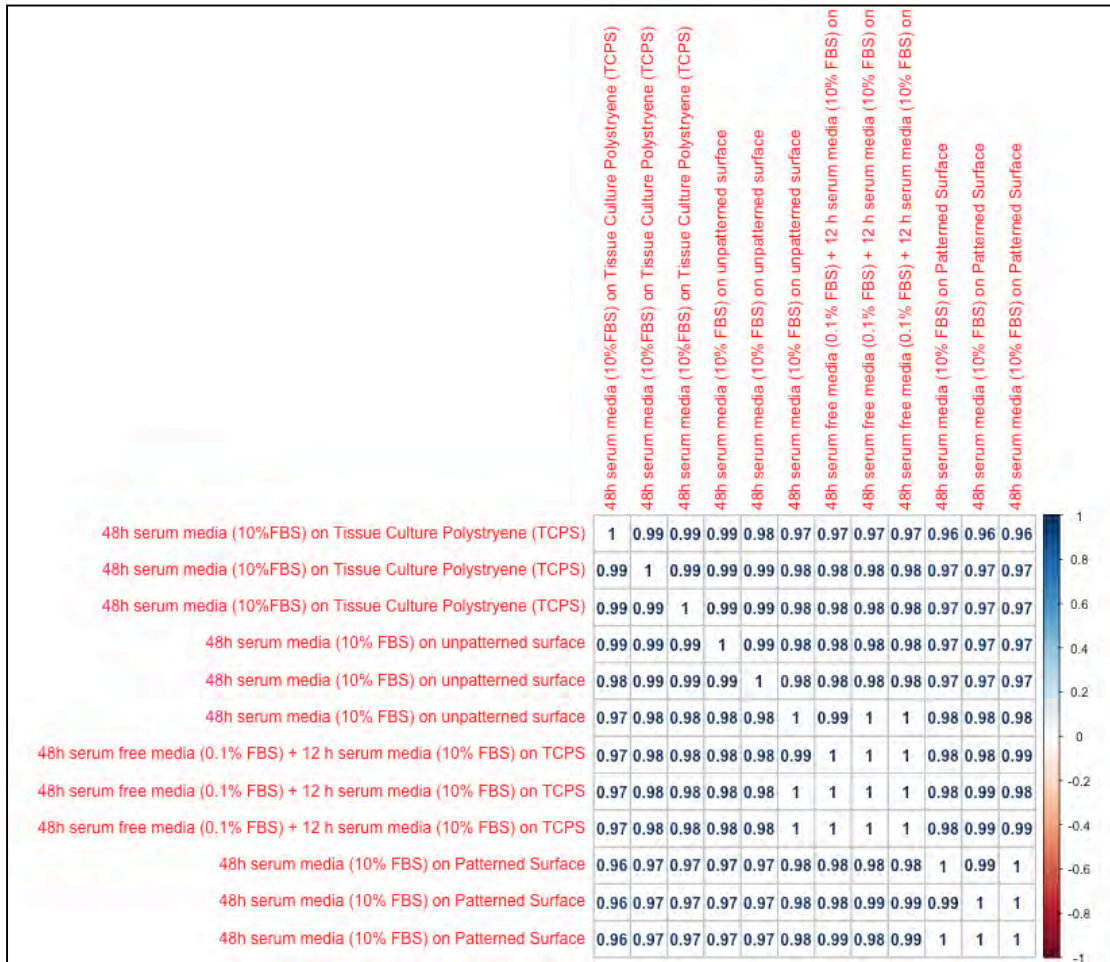


Appendix D4: Fold regulation scatter plot for hOB cells cultured on PLLA (normalized to GAPDH, ± 2 fold change was accepted as no regulation, >2 fold regulation in $y > x$ region upregulation, >2 fold regulation in $x > y$ region downregulation).

APPENDIX E



Appendix E1: PCA (Principal Component Analysis) of protein coding gene expression of four experimental groups: 48h SFM+24h SM on TCPS, 48h SM on TCPS, 48h SM on micropatterned, 48h SM on unpatterned (n=3).



Appendix E2: Correlation matrix of samples used fro RNA sequencing.

CURRICULUM VITAE

PERSONAL INFORMATION

Surname, Name: Ermiş Şen, Menekşe
Nationality: Turkish (T.C.)
Date and Place of Birth: 19 June 1985, Ankara
Marital Status: Married
Phone: +905326682923
Email: e.menek@gmail.com, ermism@metu.edu.tr

EDUCATION

Degree	Institution	Year of Graduation
MD	Hacettepe University School of Medicine	2009
High School	METU College	2002

WORK EXPERIENCE

Year	Place	Enrollment
2009-2012	Kırıkkale Yüksek İhtisas Hastanesi	MD
2012-2013	Özel Çankaya Doruk Hastanesi	MD
2015	Canary Center for Early Cancer Detection Stanford University, School of Medicine	Visiting Scholar
2013-	BIOMATEN CoE in Biomaterial and Tissue Engineering	Research Specialist

FOREIGN LANGUAGES

Advanced English

PUBLICATIONS

1. Antmen, E., Ermis, M., Demirci, U., Hasirci, V. (*In preparation*).
2. Ermis, M., Akkaynak, D., Chen, P., Demirci, U., Hasirci, V. (*Submitted*). Micropillar induced nuclear deformation (MIND): An approach linking nuclear deformation in cell populations and cancer. *Scientific reports*.
3. Ucar, S., Ermis, M., & Hasirci, N. (2016). Modified chitosan scaffolds: Proliferative, cytotoxic, apoptotic, and necrotic effects on Saos-2 cells and

antimicrobial effect on Escherichia coli. *Journal of Bioactive and Compatible Polymers: Biomedical Applications*, 0883911515627471.

4. Ermis, M., Baran, E. T., Dursun, T., Antmen, E., & Hasirci, V. A. S. I. F. (2014). Contribution of Physical Forces on the Design of Biomimetic Tissue Substitutes. *Bio-inspired Materials for Biomedical Engineering*, 59-76.

HOBBIES

Scuba diving, Free diving, Mountaineering, Caving, Travelling, Reading, Graphical Design